Thickness- and Symmetry-Induced Electronic Transport Properties of Semimetallic Transition Metal Dichalcogenides

by

Shazhou Zhong

A thesis
presented to the University of Waterloo
in fulfillment of the
thesis requirement for the degree of
Doctor of Philosophy
in
Physics (Quantum Information)

Waterloo, Ontario, Canada, 2023

Examining Committee Membership

The following served on the Examining Committee for this thesis. The decision of the Examining Committee is by majority vote.

External Examiner: Ke Wang
Assistant Professor, School of Physics and Astronomy,
University of Minnesota

Supervisor(s):   Adam Wei Tsen
Assistant Professor, Dept. of Chemistry, University of Waterloo

Internal Member: Anton Burkov
Professor, Dept. of Physics and Astronomy, University of Waterloo

Internal Member: Robert Hill
Associate Professor, Dept. of Physics and Astronomy,
University of Waterloo

Internal-External Member: Guo-Xing Miao
Associate Professor, Dept. of Electrical and Computer Engineering,
University of Waterloo

Author's Declaration

This thesis consists of material all of which I authored or co-authored: see Statement of Contributions included in the thesis. This is a true copy of the thesis, including any required final revisions, as accepted by my examiners.

I understand that my thesis may be made electronically available to the public.

Statement of Contributions

Shazhou Zhong was the sole author for Chapters 1, 2, and 5 which were written under the supervision of Adam W. Tsen. This thesis consists in part of 2 manuscripts written for publication. Exceptions to sole authorship of material are as follows:

Research presented in Chapters 3

The experiment is supervised by Adam W. Tsen and Rui He. Shazhou Zhong, Hyun Ho Kim, Daniel McHaffie and Ivana Rilak fabricated the samples. Shazhou Zhong and Hyun Ho Kim performed the transport measurements. Gaihua Ye and Logan Winford performed the Raman spectroscopy measurement. Shazhou Zhong performed the data analysis. Fangchu Chen, Xuan Luo and Yuping Sun grew the $MoTe_2$ crystals.

This chapter is based on previously published work: R. He, S. Zhong, H. H. Kim, G. Ye, Z. Ye, L. Winford, D.McHaffie, I. Rilak, F. Chen, X. Luo, Y. Sun, and A. W. Tsen, Dimensionality-driven orthorhombic $MoTe_2$ at room temperature, *Phys. Rev. B* **97**, 041410 (2018). Copyright (2018) by the American Physical Society. doi: 10.1103/PhysRevB.01410

Research presented in Chapters 4

The experiment is supervised by Adam W. Tsen. Shazhou Zhong and Archana Tiwari fabricated the samples. Shazhou Zhong, Archana Tiwari and George Nichols performed the transport measurement. Shazhou Zhong, Archana Tiwari and Adam W. Tsen analyzed the data. Fangchu Chen, Xuan Luo and Yuping Sun grew the $MoTe_2$ crystals.

This chapter is based on previously published work: S. Zhong, A. Tiwari, G. Nichols, F. Chen, X. Luo, Y. Sun, and A. W. Tsen, *Phys. Rev. B* **97**, 241409(R) (2018). Copyright (2018) by the American Physical Society. doi: 10.1103/PhysRevB.97.241409

Abstract

This thesis presents experimental study of how thickness and symmetry would impact the electron transport properties of $MoTe_2$ and WTe_2, two members of the transition metal dichalcogenide family.

In the first experiment, as presented in Chapter 3, we used Raman spectroscopy and electron transport measurement to study the phase transition in semimetallic $MoTe_2$. It is known that bulk $MoTe_2$ goes through a first-order phase transition around $\sim$250 K. The high temperature phase is monoclinic. At low temperatures, it crystallizes in the inversion symmetry breaking orthorhombic phase. Our Raman spectroscopy measurement suggests that for flakes below certain thickness, $\sim$12 nm, only the inversion symmetry breaking phase exist, even up to and beyond room temperature. The corresponding electron transport measurement also shows no evidence of phase transition around $\sim$250 K.

Since there is a distinction between the bulk and thin $MoTe_2$ in terms of how it crystallizes, the band structure of thin $MoTe_2$ is expected to be different as well. This could be evident in the electron transport measurement. In Chapter 4, we performed thickness dependent magnetotransport measurements on $MoTe_2$. Our findings show both the electron and hole carrier density decreased in thin $MoTe_2$. Also, the magnetoresistance, which is large in bulk $MoTe_2$, is suppressed systematically with reduced thickness.

The third experiment follows from a recent non-linear anomalous Hall effect work on few-layer WTe_2. This effect produces second harmonic voltage and zero frequency (DC) voltage in the transverse direction when an oscillating electric field is applied in the longitudinal direction. In Chapter 5, we reproduced this effect in WTe_2, and extended the frequency to the radio frequency range.

Acknowledgements

I would first like to thank my supervisor Dr. Adam Wei Tsen who welcomed me to his group. As the first generation of students, I am privileged with the opportunity of learning directly from him. Needless to say, this thesis would not be possible without his guidance.

Teamwork is an important aspect of doing scientific research. I am grateful for the supportive environment in our group. Thus, I would like to thank my group members who have helped me along the way. Dr. Hyun Ho Kim and Dr. Archana Tiwari taught me how to do nanofabrication. Dr. Daozhi Shen and Dr. Fangchu Chen gave me guidance and advice on how to design experiments. I thank Dr. Tarun Patel, Dr. Bowen Yang, Tina Dekker, Fangzhou Yin, Daniel McHaffie and Xiaotao Ma for many helpful discussions during the countless hours we spent in the lab together.

I also received help, often more than I asked for, from members outside of our group. Dr. George Nichols showed me the tricks of the trade in operating cryostats. Dr. Francois Sfigakis would often pause his work to lend me a helping hand. Dr. Peng Li selflessly shared his expertise in the research field that we are both in. Peter Sprenger taught me the principles and operations of radio frequency electronics, which is essential to my experiments. Stephen Harrigan provided critical feedback on my experimental design. I would also like to thank Dr. David Cory and Dr. Jonathan Baugh for generously providing much of the equipment used for this thesis. Nanofabrications were done in the University of Waterloo's Quantum-Nano Fabrication and Characterization Facility which Vito Logiudice and his team always kept in pristine condition.

I am blessed with a great advisory committee that I benefited directly from. Both materials, $MoTe_2$ and WTe_2, presented in thesis are type-II Weyl semimetal candidates. I am very fortunate to have Dr. Anton Burkov on my committee as he is an expert in the field of Weyl semimetals. He provided helpful insights based on my data. Dr. Robert Hill, who is an expert in transport measurement, discussed the details of my experimental setup. During the high frequency experiments, Dr. Guo-Xing Miao spotted some flaws in my experimental design. After redesigning the setup, my experiment went a lot smoother. Hence, I would like to express my sincere gratitude to all my committee members.

I would also like to thank my former supervisor, Paul Haljan, who introduced me to the field of scientific research.

Lastly, I would like to thank my family. In particular, my mom and dad, to which this thesis is dedicated to. They have always been supportive of me, especially during my graduate studies period. I am also very fortunate to have loving and caring grandparents who always encouraged me to pursue higher levels of education. Finally, I would like to thank my aunts and uncles for being the role models of my life.

Dedication

To my parents, for their unconditional love and support.

Table of Contents

List of Tables

List of Figures

Chapter 1

Introduction

It has been long debated if materials can exist in 2-dimensions (2D). Theoretically, it has been predicted that crystals in very thin layers are unstable as the crystal lattice would be disrupted by the thermal energy at any finite temperatures [18]. The early form of 2D material can be seen in field effect transistor. While the material itself is not 2D, but the electrons in it are forced into a near ideal 2-dimensional electron gas (2DEG). This gave birth to the discovered the quantum Hall effect in 1980 [19]. The actual realization of true atomically thin material is the successful exfoliation of single layers of graphene in 2004 [20]. The crystal structure of graphene is made up of carbon atoms arranged in a single layer as shown in Fig. 1.1(a). As electrons can only move in a 2D plane in graphene, one of the first experiments done using graphene is the demonstration of QHE [2]. An optical image of their device is shown in Fig. 1.1(a). The QHE displayed in graphene persisted up to room temperature [3], which is 10 times higher than other systems [21]. Graphene also shows extraordinary electric conductivity[22] and extremely strong intrinsic strength [23]. Since then, the field of 2D materials has grown rapidly. It includes a variety of materials from conductors to insulator, covering many phases of matters such as superconductors, magnets and topological insulators.

Intuitively, since a bulk van der Waals material is made up of identical layers, thus, the physical phenomena of the bulk would just be a combination of all the layers. However, that is not the case. Firstly, the lack of out-of-plane interactions may cause changes
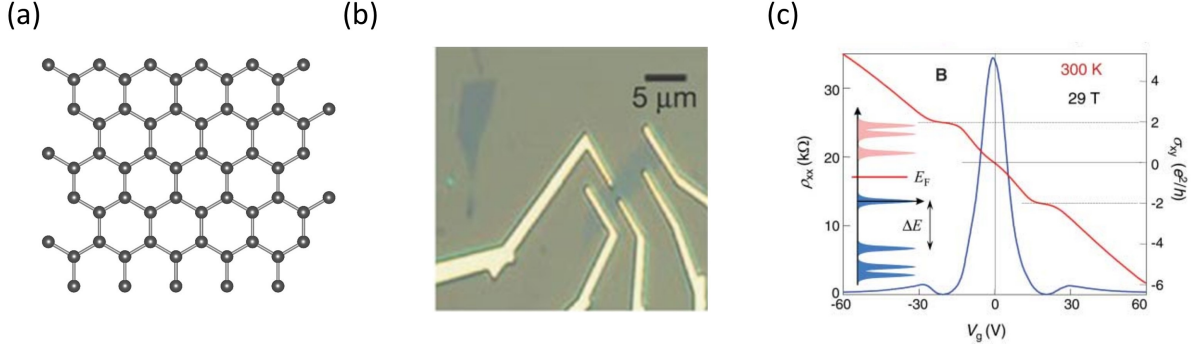
Figure 1.1: (a) Top view of graphene lattice structure. (b) Optical image of one of the first graphene devices. Figure adapted from [2] with permission from Springer Nature. (c) Experimental data of QHE observed in graphene at room temperature. The plot shows σ_{xy} (red) and ρ_{xx} (blue) as a function of gate voltages (V_g) in a magnetic field of 29 T. Inset: Schematic of the energy levels where the density of states are quantized into Landau levels. Figure adapted from [3] with permission from American Association for the Advancement of Science.

to how physical properties manifest. In the field of superconductivity, for instance, the Ginzburg-Landau theory [24] and the Eliashberg theory [25] both predict the superconducting transition temperature (T_c) should decrease as the thickness is reduced. This trend is verified experimentally, such the case in NbSe$_2$ [26]. However, few materials show the opposite can also be true. As shown in Fig. 1.2(a), T$_d$-MoTe$_2$, 2H-TaS$_2$ and FeSe on SrTiO$_3$ substrate have shown increased T$_c$ in reduced thickness. Notably, T$_d$-MoTe$_2$ sees more than an order of magnitude higher T$_c$ in its monolayer form when compared to the bulk [4]. Similarly, magnetic materials also show layer dependent magnetism. Although magnetic materials have been known for a long time, but its existence in monolayer was debated as the thermal fluctuations at any finite temperatures may destroy its magnetism [27]. The first 2D ferromagnets, CrI$_3$ [28] and Cr$_2$Ge$_2$Te$_6$ [29] were discovered experimentally in 2017. In few layers CrI$_3$, both monolayer and trilayer CrI$_3$ are ferromagnets while bilayer CrI$_3$ is an antiferromagnet [28]. The manifested magnetism is believed to be the result of the competition between the antiferromagnetic order due to interlayer coupling and the ferromagnetic order in each individual layer [28]. Aside from interlayer interac-

2
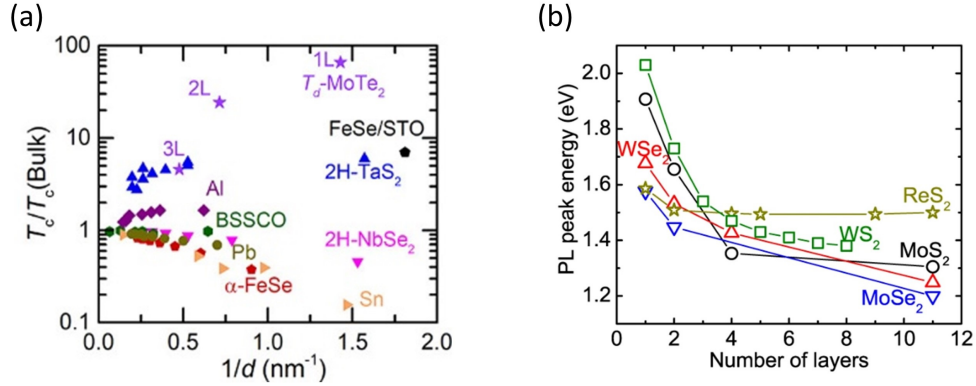
Figure 1.2: (a) Thickness dependence of superconducting temperatures in selected materials. Figure adapted from [4], copyright (2021) American Chemical Society. (b) Enhanced photoluminescence observed for semiconductors in monlayer form. Figure adapted from [5], reused under Creative Commons license CC BY 4.0.

tions, reduced thickness also shows impact on its band structure. Many of the transition metal dichalcogenides are indirect bandgap semiconductors. However, in the monolayer limit, it becomes a direct bandgap semiconductor due to quantum confinement [30, 31]. The bandgap also increases with reduced thickness [32]. Accompanied with the change in band structure, the photoluminescence also tends to increase when reaching the monolayer limit [5]. Fig. 1.2(b) shows some of layer depend photoluminescence in common TMDC semiconductors.

Having an isolated 2D material, one can also use it as building blocks of novel 3D materials. Proximity effect, for instance, only happens at the boundary of two materials. Such effect is weak for bulk materials as the majority bulk part is not affected. When the material is thin enough, however, the properties presented can be influenced significantly by the neighboring materials. For instance, graphene is a non-magnetic material. When placed on yttrium iron garnet, a ferromagnetic material, ferromagnetism is induced on the neighboring graphene [33]. Another type of novel material is to form moiré structures. From daily experience, when two periodic structures overlap each other, a moiré pattern can be formed. Similar, when two layers of material with comparable lattice constant are stacked together, a moiré structure can also be formed. Typically, the moiré lattice constant

(a)

(b)
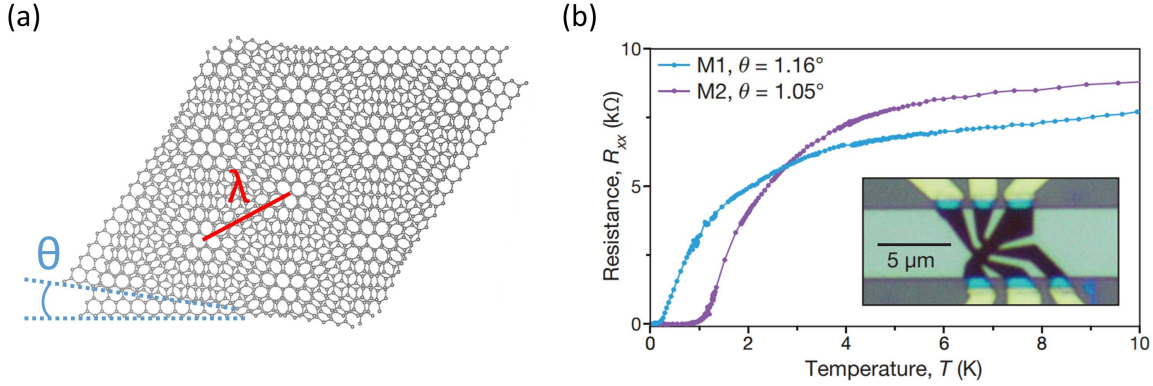
Figure 1.3: (a) The morié structure with periodicity, λ, formed by two layers of graphene stacked at an angle, θ. (b) Superconductivity shown in twisted bilayer graphene. Inset: Optical image of the twisted bilayer device. Figure adapted from [6] with permission from Springer Nature.

is larger than the material's crystal lattice constant. This gives raise to a new periodic potential which results in a smaller Brillouin zone. One early example is the placement of graphene on BN [34]. Moiré structure can also be created by using same material by varying the angle between the two layers. A schematic of two layers of graphene stacked together is shown in Fig. 1.3(a). With a twist angle, θ, the superlattice with periodicity, λ, can be seen clearly. "Magic angle" twisted bilayer graphene is when two layers of graphene are stacked together with a $\sim 1.1°$ twist angle. New phenomenon such as superconductivity (shown in Fig. 1.3(b)) and correlated insulator states were observed in the system, both are not known in pristine graphene [6].

1.1 Synthesis of 2D materials

Many techniques have been developed to synthesis 2D materials, which can be categorized by either the bottom-up approach or the top-down method. In the former, the 2D materials are formed by assembling the atoms into the desired structure [35]. Usually, it requires very specific conditions for the 2D material to form properly or expensive equipment to

achieve well controlled environment [36]. However, compared to the top-down method, it does not require the material to be layered. Also, it is capable of producing 2D materials in mass amount. One well known example of bottom-up approach is few layers Cr-doped $(Bi,Sb)_2Te_3$ grown by molecular beam expitaxy, which demonstrated the first realization of Quantum anomalous Hall effect [37]. Other techniques include physical vapor deposition and chemical vapor deposition.

The process of scotch tape exfoliation belongs to the top-down method where thin layers are isolated from the bulk crystal. Earlier attempts of trying to peel off a single layer from the bulk can be traced back to the 1960s [38, 39]. However, it did not gain much attention until the discovery of graphene. Since then, this technique has been applied to isolate single layers of many other materials [40]. This method works because the layers of a van der Waals material are weakly bonded. It is experimentally estimated that $\sim$300 nN of normal force is needed to cleave off the top layer of graphene from the graphite crystal [41]. It turns out the adhesion force between the Scotch tape and the topmost layer is sufficient to overcome this interlayer force. It is surprising that this method does not require any expensive equipment. Hence, it has been widely adopted to obtain monolayers. It does have its downsides as well. For instance, the yield is usually limited and the typical size of monolayers are on the order of 10x10 μm^2. Also, van der Waals force between the neighboring layers in other materials may be stronger than of graphite such that using Scotch tape alone would not result in reasonably-sized monolayer, if any at all. Many additional techniques, however, have been developed to improve both the size and yield. For instance, machine-based exfoliation method seems to be better than human operation [42]. Modifying the surface of the substrate used for the exfoliation process also shows improved results. By heating and performing oxygen plasma cleaning on the Si/SiO_2 substrate, the size of the exfoliated monolayer graphene can be >300x300 μm^2 [43]. Coating the substrate with gold also shows promising result with centimeter-sized MoS_2 monolayer demonstrated[44]. Other popular top-down methods include liquid exfoliation and chemical exfoliation techniques. Although they have better yields as compared to mechanical exfoliation, the size are typically small and have lower quality [35]. The Scotch tape method has proven to produce 2D materials with high quality, which is a priority in studying the fundamental properties of it. Therefore, this is the method used in this thesis.

5

The procedure in exfoliating and making of the test devices are presented in Chapter 2.

1.2 Transition metal dichalogenide
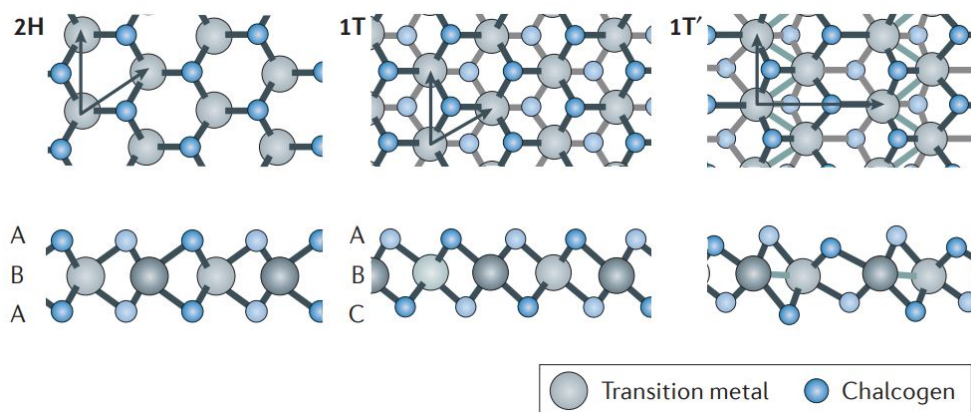
Figure 1.4: Schematics of the common crystal structures of single layers of TMDC materials. Figure adapted from [7] with permission from Springer Nature.

TMDC is a family of materials that share the chemical formula of MX_2, where M is a transition metal (group IV, V, VI, VII, IX or X) and X is a chalcogenide (S,Se or Te). Commonly, TMDC crystallizes in either the 2H (trigonal prismatic) phase or the 1T (octahedral) phase with the structure of the phases shown in 1.4. In the 2H phase, each layer consists of three atomic planes with an ABA stacking. The chalcogen atoms in the top and bottom plane occupy the same position in the direction perpendicular to the layer. Each unit cell consists two layers that are rotated by 60°. In the 1T phase, the three atomic planes in each layer stacks has an ABC stacking order. Often, the metal-metal bond is strong such that the metal chain becomes distorted [45, 46]. This distorted 1T phase is known as the 1T' phase. Due to the many combinations of atoms, TMDCs host a wide range of physical properties. A lot of the TMDC materials are layered, which makes the Scotch tape exfoliation process applicable. Hence, TMDCs have been studied extensively in the 2D limit. The known layered TMDCs with their possible crystal structures are summarized in Fig. 1.5.
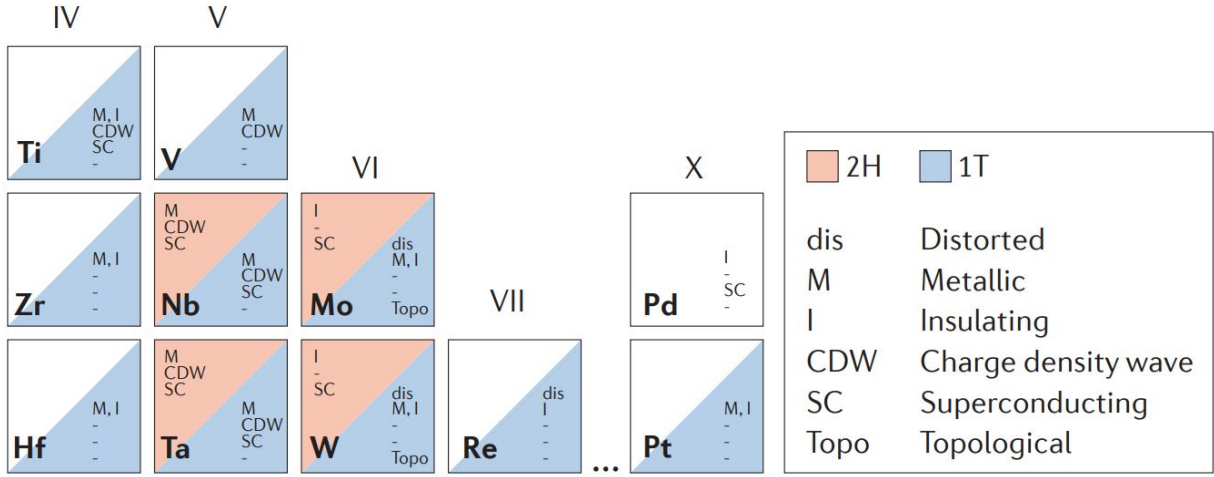
Figure 1.5: Summary of known layered TMDC materials with their existing structures. Figure adapted from [7] with permission from Springer Nature.

In this thesis, we focus on the electronic transport study of $MoTe_2$ and WTe_2. In its bulk form, $MoTe_2$ is able to crystallize in a few different structures. Its stable form at room temperature is the 2H phase, which is semiconducting with a bandgap of $\sim$1.1 eV [47, 48]. It is able to remain metastable at room temperature in the centrosymmetric 1T' phase and is semimetallic. At low temperature, it remains semimetallic and transitions to the T_d phase (space group $Pmn2_1$) where the unit cell is orthorhombic and breaks inversion symmetry. Although TMDCs tend to have a range of crystal structures, WTe_2 is an exception. Bulk WTe_2 is only stable in the T_d phase for room temperature and below. The T_d phase of both crystals have been theoretically predicted to be type-II Weyl semimetal candidates [49, 50]. Later, Fermi arcs were also observed in $MoTe_2$ [51, 52] and WTe_2 [53, 54]. Furthermore, anisotropic negative magnetoresistance in thin WTe_2 also supports this claim [55]. However, there are still debates and more evidence is needed to draw definite conclusions [56]. The study in reduced thickness of both materials has also been active. In monolayer WTe_2, the interior becomes insulating while the edges remains conductive. Hence, it has been considered as the first 2D topological insulator [57]. Studies have suggested similar behavior in T_d-$MoTe_2$ where a bandgap opens in the thin limit [58]. However, this is debated as others have observed semimetallic T_d-$MoTe_2$ even down to

7

monolayer [4]. This topic is explored in this thesis and presented in Chapter 3. In terms of its transport properties, both materials exhibit extremely large magnetoresistance at low temperatures [59, 60]. This is attributed to the compensation of electron and hole carriers. In Chapter 4, we present the magnetotransport experiments of thin $MoTe_2$. More recently, a new form of Hall effect, non-linear anomalous Hall effect (NLAHE), has been realized in few layers WTe_2 [15, 16] and T_d-$MoTe_2$ [61]. Chapter 5 presents the study of the NLAHE in thin WTe_2 at higher driving frequencies.

Chapter 2

Experimental Techniques

For the experiments presented in this thesis, we are aiming to measure the electronic transport properties of thin materials. This chapter presents the general procedure in preparing the samples and the measurement environment. The thin flakes are first obtained by mechanical exfoliation from bulk crystal. Since the dimensions of the exfoliated flakes are typically less than 20 μm, we cannot make electrical contacts directly using metallic wires. Instead, we use photolithography techniques to make the appropriately sized electrodes. We then transfer the target flake to the pre-patterned electrodes. Finally, the sample is loaded in cryostats for electron transport measurements in low temperature and high magnetic field environment.

2.1   Sample fabrication

All materials used in this thesis are layered materials, which means the neighboring atomic layers are bonded by van der Waals force. As demonstrated by Novoselov et al., the layers can be separated using scotch tape [20]. First, place a bulk crystal onto the scotch tape. After successive exfoliation between the tape, the bulk crystal separates into thinner flakes. The flakes are then stamped onto a Si substrate with 285 nm of SiO_2 layer. When thin flakes are placed on the Si/SiO_2 substrate, it changes the interference color as compared to

the native color of the substrate. The resulting color depends on the flake thickness [62]. Therefore, flakes of desired thickness range can be picked out by the color contrast[63]. The precise thickness of a chosen flake can be measured by atomic force measurement (AFM). The error depends on the tip used and the scanning rate. Typically, the measurement error is about 2 nm. To prevent thin films from degradation, the exfoliation process is done inside a nitrogen-filled glovebox with oxygen level < 5 ppm [64]. The samples are covered with more inert flakes, such as hexagonal boron nitride (hBN), before being taken outside of the glovebox.

2.1.1 Stamping method

When the targeted flake of desired thickness is isolated, the next step is to place it onto the pre-patterned electrodes. One way to do so is using a polydimethylsiloxane (PDMS) polymer stamp [65]. For this method, the bulk crystal is first exfoliated between Scotch tape and a piece of PDMS. Some fakes will be transferred onto the PDMS surface. Next step is to look under a microscope to identify suitable flake. The setup is shown in 2.1(a). The PDMS is attached to a glass slide, which is held by a manipulator to provide movements in all three directions. Since PDMS is transparent, using the transmission mode of the microscope can give a rough estimate of the flake thickness. After a flake has been chosen, it can be aligned to the desired location using the microscope. Press down hard on the PDMS so the targeted flake is stamped onto the pre-patterned electrodes. Sometimes, the flake would not stick to the electrodes. In such a case, raising the temperature up to 90°C during the stamping process can increase the chance of transferring.

2.1.2 Dry pickup technique

When thin flakes are on PDMS, it is very hard to estimate the flake thickness. Also, for very thin flakes, it can be very transparent and hard to find. The better way to identify flake thickness is when it sits on Si/SiO_2 substrate. Hence, another transfer technique we use is the dry pick-up technique [66, 67]. A solution of 6 % polycarbonate (PC) in chloroform by weight is prepared. Then, spread out the PC solution onto a piece of glass
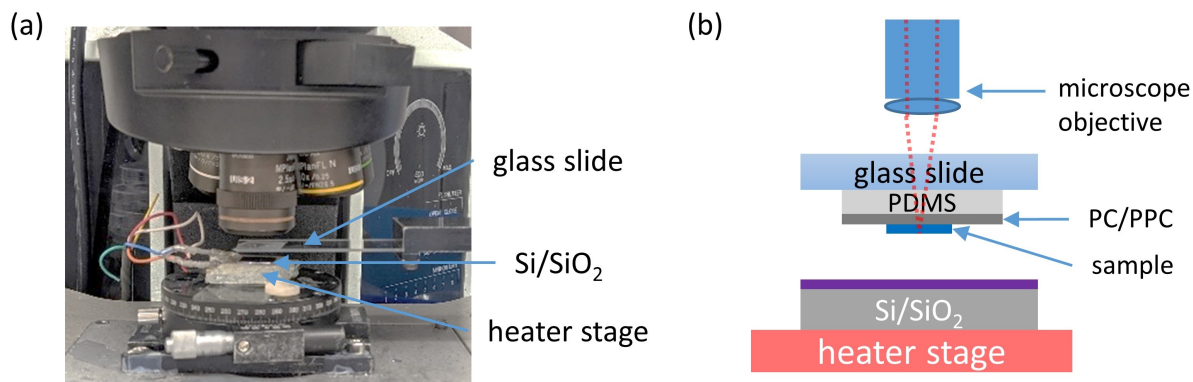
Figure 2.1: (a) Picture of the transfer stage setup. (b) Schematic of the dry pickup transfer method setup.

slide and heat it on a hot plate at 60°C for 15 min. The resulting thin film of PC is cut into smaller pieces, $\sim$ 1×1 cm. Then, place the PC film over a piece of smaller PDMS that sits on a glass slide. Finally, the structure is secured by taping it down on the glass slide. This handle is then mounted on a mechanical manipulator. The pick-up and transfer procedure is similar to the PDMS stamping process. A schematic of the setup is shown in Fig. 2.1(b). Using the microscope, the PC film can be aligned over a chosen sample flake for pick-up process. The glass slide lowers until the PC film is in contact with the flake. Set the temperature of the base to 90 °C so that the PC softens and conforms to the Si/SiO_2 chip. After the PC has conformed well with the flake, turn off the heater and allow it to cool down to below 50°C so that the PC hardens. Slowly lift up the handle to pickup the targeted flake. Finally, align the sample flake to the pre-patterned electrodes and stamp it down. This time, set the heater to 150°C so that the PC film melts down and detaches from the PDMS. The layered stakes are successfully transferred onto the pre-patterned electrodes with a layer of PC film on top. Immerse the whole chip in chloroform for $\sim$2 min to dissolve the PC film.

2.2 Pre-patterned electrodes

For robust materials, metal electrodes can be deposited directly on top using the nano-fabrication techniques. However, air sensitive materials that we work with are not suitable for such process. Hence, we will first make the electrodes and then transfer the samples onto them. Workflow of a typical process is shown in the top panel of Fig. 2.2. First, we start by cleaning the wafer using acetone and isopropyl alcohol. Both chemicals are used to wash away organic residues. The wafer is further cleaned using oxygen plasma. If using Si/SiO$_2$ substrate, hexamethyldisilazane (HMDS) treatment is done to ensure better adhesion of the photoresist. Then, spincoat photoresist onto the clean wafer. This process aims to coat a uniform layer of photoresist that is ∼1400 nm. Depending on the type of photoresist used, soft bake it on the hot plate at the recommended temperatures. The wafer is then loaded into a maskless photo lithography tool for exposing the designed pattern. The exposure is done by a laser in the ultra-violate (UV) wavelength. The exposed parts of the photoresist come off when immersed in the developer solution, leaving the rest of the area protected by the photoresist. Metal, such as gold or platinum, are deposited onto the wafer using electron beam vapor deposition. The typical electrode thickness we use ranges from 30-100 nm. Finally, use photoresist remover to clear all the photoresist on the wafer. The typical resolution for the final electrodes is ∼1 μm.

Oftentimes, the thin flakes samples are comparable in thickness as compared to the electrodes. It is reasonable to suspect the samples will be under strain when sitting on the electrodes. There is a drawback for making the electrodes arbitrarily thin. Gold, for instance, will have much higher resistance when the thickness drops below 30 nm [68]. In order to solve this issue, we buried part of the electrode under the substrate, exposing only part of the electrodes. This is done by first etching the substrate for about 30 nm before depositing the metal films. The whole process is similar to the standard process, with an extra etching step added. The process is shown in the bottom panel in Fig. 2.2. An atomic force microscopy (AFM) image of a sample electrode that is made in such a way is shown in Fig. 2.3(a). From the line profile shown in Fig. 2.3(b), the electrodes extend ∼10 nm above the SiO$_2$ surface with a roughness ∼2.4 nm measured over an area of 1 um^2.

The standard lithography process will create a very sharp edge around the electrodes.
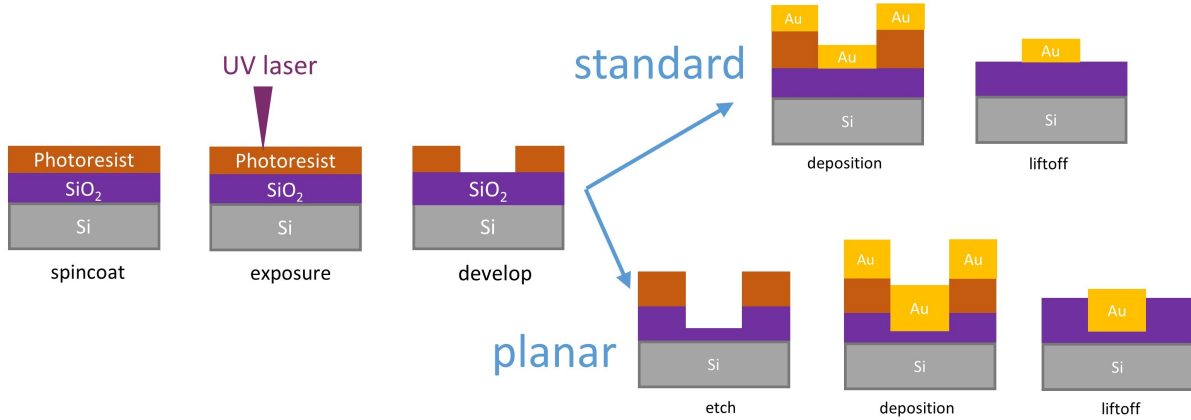
Figure 2.2: Work flow of a typical nano-lithography process for making pre-patterned electrodes. The planar electrodes are made by burying part of the metal into the SiO_2. Schematics not to scale.

It affects samples that are near the monolayer limit. In order to avoid this issue, electrodes can be made using bilayer photoresist process. The process uses an extract layer of polydimethylglutarimide (PMGI) based polymer before spincoating the regular photoresist. The exposure process applies to the bilayer using the same laser. The development process is a bit different and will result in a re-entrant sidewall profile as shown in Fig. 2.4(a). The final electrodes will have a slope rather than cliff-like edge. AFM image of a sample electrode created using this process is shown in Fig. 2.4(b) with the height profile in Fig. 2.4(c). Unfortunately, the resolution will be compromised with the minimal feature size increased to $\sim$2 μm.

By placing test samples on pre-patterned electrodes, only the bottom surface is in contact with the probes. It presents a concern that the current flow is not uniform throughout the layers. The better setup is to have side contacts as in bulk crystal measurements. However, since both $MoTe_2$ and WTe_2 are air sensitive, it is very hard to deposit metal contact directly on top without exposure to the ambient environment. Recent report on $MoTe_2$ did include a measurement of the resistivity in the c-axis direction, which is $\sim$4 times larger than the in-plane resistivity [61]. Also, considering the dimension of our samples, almost all of the flakes used are <50 nm thick. That is about two orders of magnitude
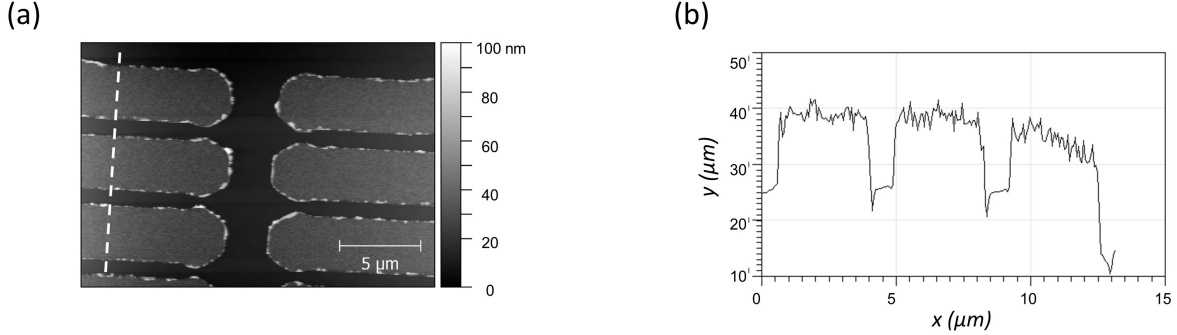
Figure 2.3: (a) AFM height image of pre-patterned electrodes with part of it buried in SiO_2. (b) Line profile taken along the dashed white line in (a).

smaller compared to the width and length, which ~ 5 μm. Considering only classic Ohm's law, electrons should move a lot easier in the c-axis direction as compared to the in-plane direction. Hence, the current should be fairly uniform throughout all layers.

2.3 Cryogenic experimental environment

Two different cryostats are used to obtain the data in this thesis. The general principals of how these cryostats operate are explained well by Pobell [69].

2.3.1 Closed-cycle helium cryostat

Experiments without the need of magnetic fields were done using the C2 cryostation by Montanta Instruments Corporation. The helium gas is enclosed in the main unit, separated from the sample chamber. The sample space is pumped down to below 2 Torr first. Then, the compressor starts up, and lowers the temperature of the cold finger that's thermally connected to the sample. The designed temperature range is from 4.9 K to 350 K. We have achieved higher temperatures by manually controlling the heater power. When the sample thermometer reached 410 K, which this cryostat is not designed for, an overheat protection alarm will be triggered and the system is forced to shut down.

14
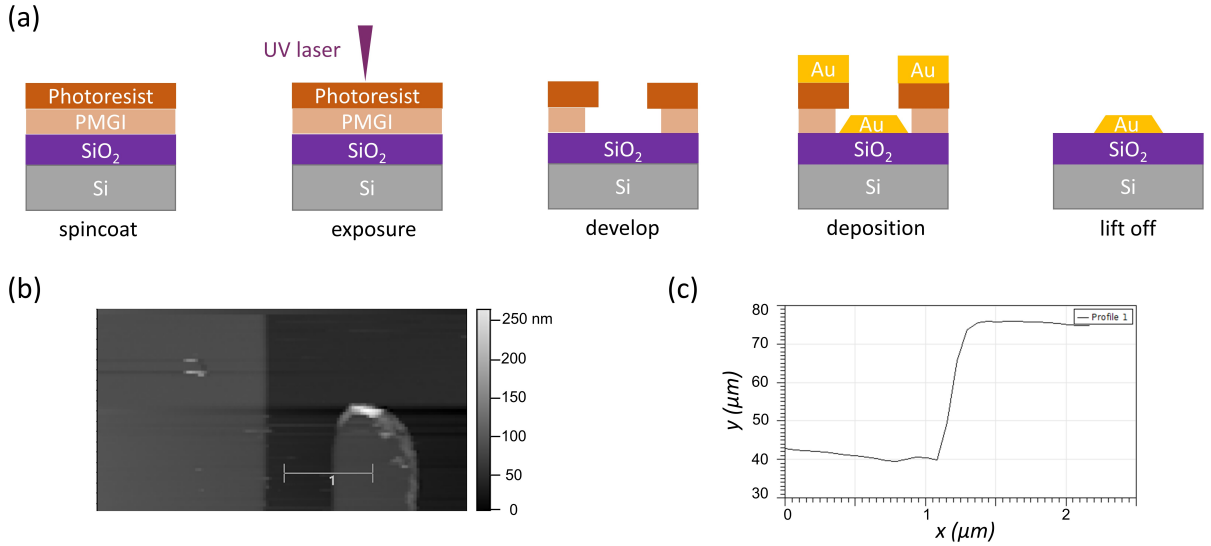
Figure 2.4: (a) Schematics of bilayer photoresist photolithography process. Diagrams are not to scale. (b) AFM height image of pre-patterned electrodes made using bilayer photoresist process. (c) Line profile taken along the white line in (b).

2.3.2 ^{3}He cryogenic system

For experiments that require lower temperatures, it is better to use a system with liquid helium. In this thesis, a cryostat made by Janis Research Company is used with the schematic shown in Fig. 2.5. A 12 T superconducting magnet is immersed in the helium bath that provides the magnetic field. In its equilibrium state, the sample space is about 4 K. A heater is located close to the sample space so the temperature can be regulated between 4 K and room temperature. Using an insert that is equipped with ^{3}He, it can achieve lower temperatures. ^{3}He has a lower boiling point of 3.2 K, and can be further reduced when pumped on. ^{3}He is enclosed in a hermetically sealed space to prevent any loss. Starting from the top is the charcoal chamber that holds charcoal inside the ^{3}He space. At low temperatures, ^{3}He molecules are adsorbed on the surface of the charcoal. When heated it up using a heater, ^{3}He will be released in gaseous form. Below the charcoal chamber is the 1 K pot that surrounds the outside of the ^{3}He space. The 1K pot can be filled with ^{4}He and can be pumped so its temperature is <2 K. When gaseous ^{3}He

15
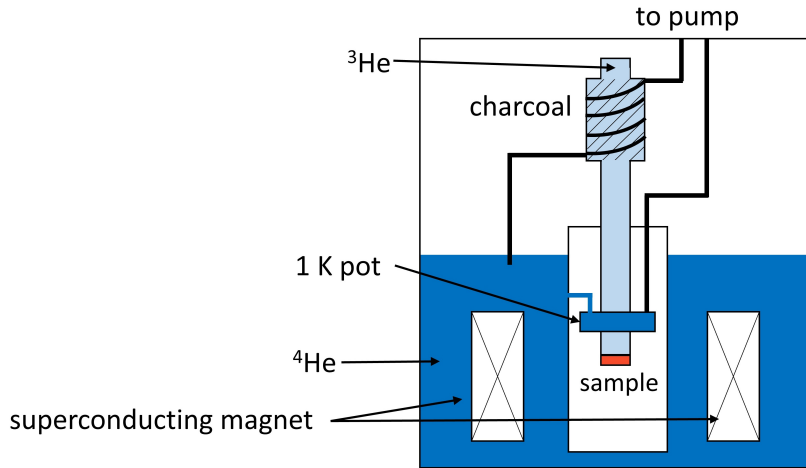
Figure 2.5: Schematic of the ^{3}He cryostat used in this thesis.

encounters the cold surface near the 1 K pot, it condenses into liquid form and drips to the bottom. The sample is attached on the outside of the ^{3}He space. The sample space is enclosed in vacuum, isolated from the surrounding ^{4}He bath. When all ^{3}He is condensed, the process can be reversed by cooling down the charcoal with the ^{4}He gas coils around the outside. Once the charcoal cools, it is able to adsorb the ^{3}He again. This makes the charcoal a pump, reducing the boiling point of the liquid ^{3}He. The base temperature of our setup is about 0.3 K. It will stay at this temperature and can be held until liquid ^{3}He dries out. Typically, sweeping the magnetic field from full positive to full negative takes about 3 hours. There is sufficient liquid ^{3}He in the system so the base temperature can be maintained during this time. For temperatures between 0.3 K and 4 K, a heater is used to increase the temperature of liquid ^{3}He. This will increase the evaporation rate of the liquid ^{3}He, reducing the measurement time. Based on our experiments, 1.7 K is the highest that we can maintain for a reasonable amount of time. Once the liquid ^{3}He dries out, the sample temperature will increase to 4 K. This process can be repeated to start another round of measurement.

Chapter 3

Dimensionality-driven orthorhombic MoTe$_2$ at room temperature

3.1 Introduction

MoTe$_2$, like most other TMDCs, displays a layered structure. Each layer is made up of three atomic planes as shown in the side views of Fig. 3.1(a). At room temperature, MoTe$_2$ naturally crystallizes in the 2H phase (α-MoTe$_2$) and belongs to the space group P6$_3$/mmc. The Mo atom is in the center of a trigonal prism of tellurium atoms [70]. In this phase, MoTe$_2$ is an indirect bandgap semiconductor with an indirect gap bandgap of 0.88 eV [71]. When thinned down to monolayer, it becomes a direct-gap semiconductor with an optical bandgap of 1.1 eV [47, 48].

By heating up to above 1175 K, MoTe$_2$ undergoes a phase transition. The abrupt jump in the temperature-dependent resistivity plot shown in Fig. 3.1(b) indicates semiconductor to semimetal transition [8]. This high-temperature phase has a monoclinic crystal structure and belongs to space group P2$_1$/m. This phase is known as β-MoTe$_2$ (or 1T'-MoTe$_2$) and the top and side view are shown in Fig. 3.1(b) [72, 73]. The Mo atoms are squeezed closer together and form pairs. The pairing is believed to be a result of metal-metal bonding [45, 46, 70]. This also forces Te atoms to be in different plane [70]. By quenching it

17
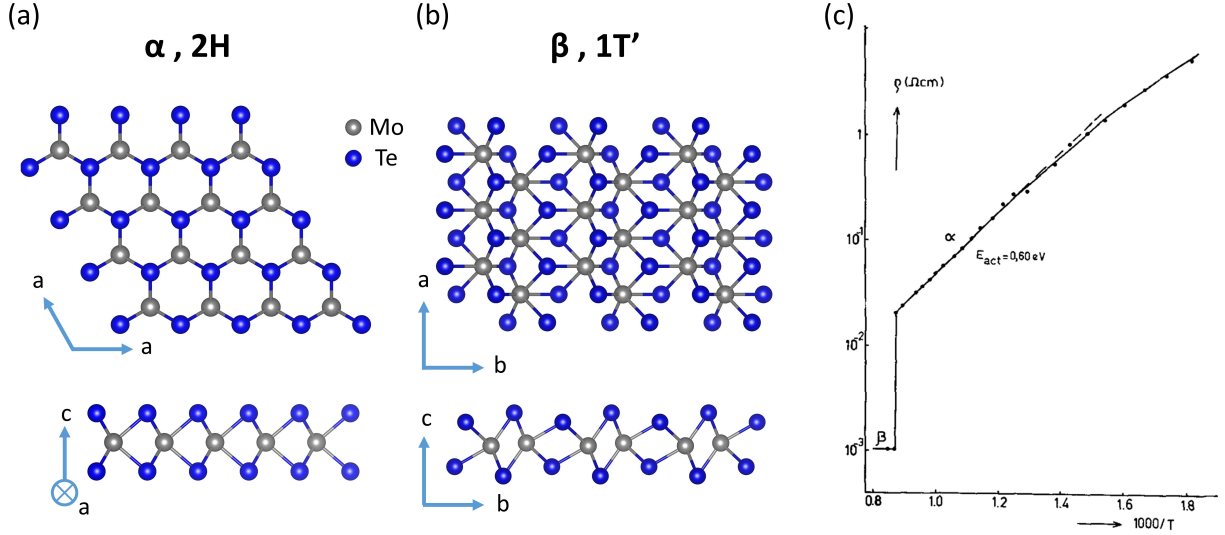
Figure 3.1: Crystal structure of (a) α-MoTe$_2$ and (b) β-MoTe$_2$. The a-axis direction is defined parallel to the Mo-Mo zigzag chain. (c) Resistivity versus reciprocal temperature for α- and β-MoTe$_2$. The abrupt jump at 1175 K indicates a semiconductor to metal transition. Figure adapted from [8] with permission from Elsevier.

down from high temperatures, β-MoTe$_2$ maintains it structure and is metastable at room temperature [74]. It is interesting to note that MoTe$_2$ can transition between the two phases via laser irradiation [75] and electrostatic gating [76].

Semimetallic MoTe$_2$ shows anisotropy in electrical transport measurement as shown in Fig. 3.2(a). Resistivity along the a-axis is smaller due to the Mo-Mo chain formed in that direction [9]. Another major observation in the plot is the hysteresis around 250 K, which hints a first-order phase transition. This was later investigated by Clarke et al. using x-ray diffraction. The structure of the low-temperature MoTe$_2$ was determined to be an orthorhombic structure where the monoclinic angle in β-MoTe$_2$ was shifted from $\sim$93° to 90° [74]. This new phase is called γ-MoTe$_2$ (or T$_d$-MoTe$_2$). The change in stacking angle is subtle, but it puts the crystal in the non-centrosymmetric space group $Pmn2_1$. At low temperatures, γ-MoTe$_2$ exhibits a number of interesting properties. This includes extremely large magnetoresistance [13, 58, 60], which is primarily attributed to the balance

18
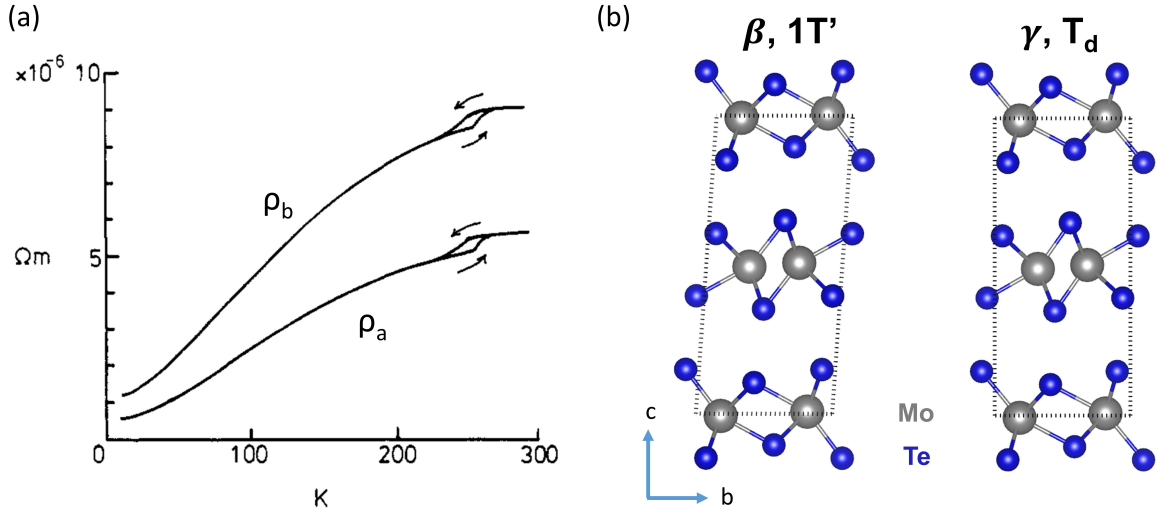
Figure 3.2: Temperature dependence resistivity of semimetallic $MoTe_2$. Figure adapted from [9], with ρ_a and ρ_b swapped to be consistent with axis direction defined in this thesis. ©IOP Publishing. Reproduced with permission. All rights reserved.

of electron and hole carriers. The magnetoresistance can be changed by applying pressure or strain [77, 78]. Superconductivity was observed in $MoTe_2$ with a transition temperature of ~0.1 K [79]. The transition temperature can be tuned by pressure [78] and thickness [4]. Many reports have found possible unconventional origins to its superconductivity mechanism [4, 14, 79–83].γ-$MoTe_2$ has been proposed to be a type-II Weyl semimetal [49, 50]. Experimentally, Fermi arcs and Weyl nodes were also observed [50–52, 84–86]. However, γ-$MoTe_2$ remains to be a Weyl candidate as there are still debates and more evidence is needed to draw definite conclusions [56].

Although bulk $MoTe_2$, in either β or γ phase, is regarded as a semimetal, there are disputes regarding its electronic transport properties in the monolayer limit. Some reports showed that few layered-$MoTe_2$ behaves like a semiconductor with a bandgap ranging from 28 to 60 meV [58, 87]. This is observation is reasonable as WTe_2, with crystal structure and electronic properties similar to $MoTe_2$, opens up a bandgap in the monolayer limit [57, 88]. However, a more direct measurement of the band structure, angle-resolved photoemission spectroscopy, was performed on monolayer $MoTe_2$ grown by molecular beam epitaxy. The

19

result does not show any bandgap [89]. Furthermore, semimetallic properties that persisted down to monolayer were also reported [4]. Another report by Song et al. showed few-layered MoTe$_2$ displays semiconducting electrical transport properties. However, their infrared spectroscopy measurements suggest there is no bandgap even for MoTe$_2$ as thin as bilayer. They believe thin MoTe$_2$ became ambipolar while its band structure remains gapless [90]. Due to the inconsistent reports, it is still under debate whether semimetallic MoTe$_2$ opens up a bandgap when the thickness is reduced [91].

In this work we explored the effects of reducing thickness in semimetallic MoTe$_2$. Since the β-γ phase transition involves an out-of-plane distortion, it may be possible to tune this transition by changing dimensionality. Thus, we first measured the temperature-dependent resistivity for flakes of various thicknesses. Our data shows semimetallic MoTe$_2$ does not transition to semiconductor for thickness down to 7 nm, the thinnest sample we tested. We also noticed the anomaly at $\sim$250 K gradually vanishes as thickness is reduced. Then, we used Raman spectroscopy to identify the crystal structure. With both Raman and transport measurements, we conclude that γ-MoTe$_2$ is observed in moderately thin samples below $\sim$12 nm at temperatures up to 400 K. The mechanism may originate from the inherent three-dimensional (3D) band structure of MoTe$_2$—reducing thickness confines hole carriers along the c-axis, which stabilizes the orthorhombic phase in accordance with theoretical predictions [10].

3.2   Electronic transport measurement

The upper right inset of Fig. 3.3 shows an optical image of a representative device with the MoTe$_2$ flake outlined by a dashed line. In the main panel of Fig. 3.3(b), we show temperature-dependent resistivity, normalized to the resistivity at 280 K, $\rho(T)/\rho(280 \text{ K})$, for 1.2 K/min cooling and warming of three thin MoTe$_2$ samples (thickness 7, 50, and 180 nm) prepared in this way as well as that of a bulk crystal (thickness 100 μm). The traces for the thin flakes are offset vertically for clarity, and the offset values are marked by dashed lines on the right.

First, in contrast with an earlier study on unprotected MoTe$_2$ flakes, which reports

(a)

(b)
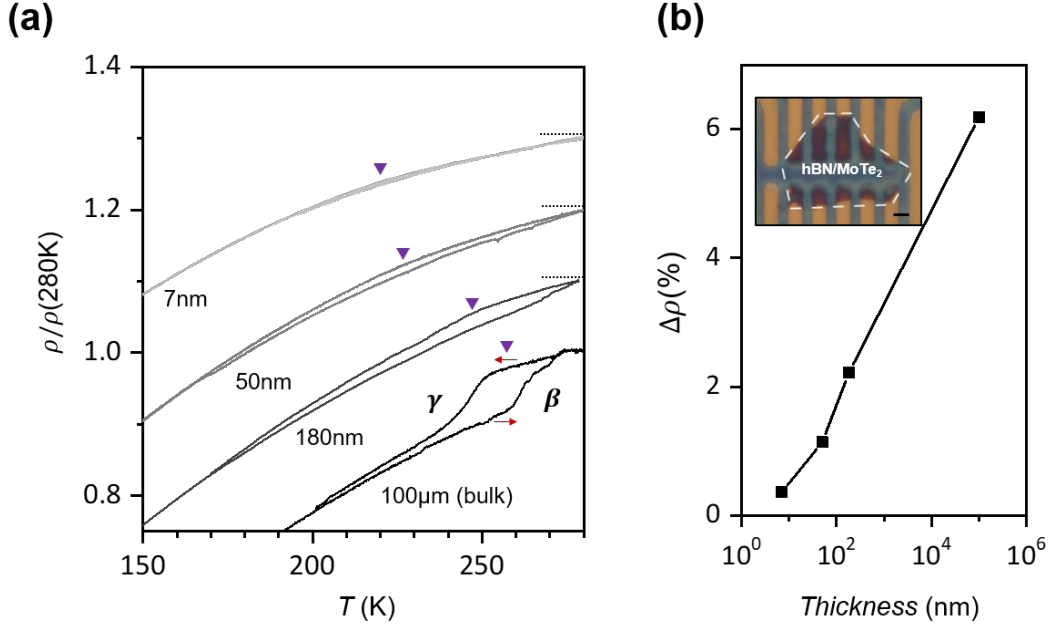
Figure 3.3: (a) Normalized temperature-dependent resistivity of MoTe$_2$ bulk crystal and thin flakes. Upper traces are offset for clarity. Kink and hysteresis between cooling and warming at 250 K corresponds to a first-order β-γ phase transition. Hysteresis becomes less visible in thinner flakes. (b) Percentage resistivity difference between cooling and warming in the middle of the hysteresis region (marked by purple arrows) as a function of flake thickness. Inset: Optical image of thin flake device capped with hBN to protect from sample oxidation. MoTe$_2$ is outlined with a dashed line. Scale bar is 10 μm.

a metal-to-insulator transition in samples below $\sim$10-nm thickness [58], all samples here show metallic behavior down to 150 K, i.e., $\frac{d\rho}{dT} > 0$. We also investigated the effects of backgating of the 7-nm-thick device as shown in Fig. 3.4(a). We observe little change as the gate voltage changes between ±30 V. This is not unexpected as the carrier concentration of bulk MoTe$_2$ at high temperature is $\sim$10^{21} cm^{-3} [13, 60], and so a 10-nm-thick sample will possess a sheet concentration of $\sim$10^{14} cm^{-2}. The charge doping induced by the backgate is $n_g = C_g V_g/e$, where C_g is the gate capacitance per unit area. Using the 300 nm SiO$_2$ as the dielectric material, $C_g \sim$115 μF/m^2. Therefore, the carrier concentration induced by

the backgate is on the order of $\sim 10^{12}$ cm^{-2}, far less than the intrinsic carrier concentration in MoTe$_2$. Fig. 3.4(b) shows the temperature sweep at different backgate voltages. A
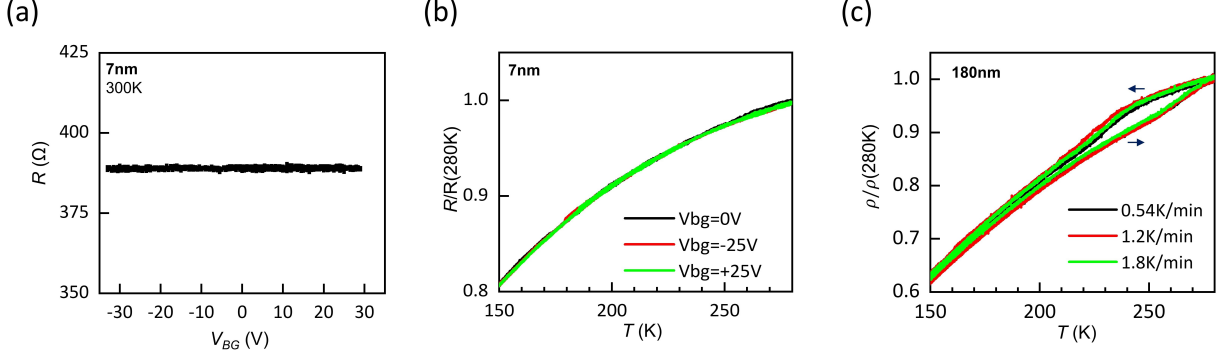
Figure 3.4: (a) Backgate-dependent resistance for 7-nm-thick device measured at room temperature. (b) Temperature-dependent resistance of the same device for three different gate voltages.(c) Sweep rate dependence of the resistivity versus temperature sweep.

previous study on unprotected thin WTe$_2$ showed insulating behavior for thickness below 5 layers [92]. However, this is likely caused by surface oxidation [93, 94]. Later, many studies used BN as protection layer showed WTe$_2$ stays metallic for 3 layers and thicker [16, 57, 95]. Likewise, surface degradation may be the reason for the insulating behavior observed in thin MoTe$_2$. Secondly, while the resistivity of the bulk crystal shows a kink and a hysteresis between cooling and warming around $\sim$250K, as indicative of the β-γ phase transition [9], the hysteresis becomes less apparent with decreasing thickness and is barely visible for the 7-nm flake. To quantify this trend, in the upper left inset of Fig. 3.3, we plot the percentage resistivity difference between cooling and warming, ρ, measured in the middle of the hysteresis region (marked by purple arrows in the main panel) as a function of sample thickness in log scale. We observe that ρ is substantially reduced from the bulk value even for a relatively large thickness of 180 nm, which is unexpected in that it contains over 250 layers (the single-layer thickness is $\sim$0.7 nm) and reflects that the β-γ phase transition in MoTe$_2$ is essentially 3D in character. The hysteresis loop is also not sensitive to changing temperature sweep rates. We have measured temperature sweep rate dependence for the 180-nm-thick sample and the results are shown in Fig. 3.4(c). We do

not observe much difference in the hysteresis as the sweep rate is changed by a factor of three—1.8 K/min is the fastest ramp rate allowed by our cryostat.

Results from the resistivity measurements presented above suggest one of two scenarios: For thin samples, either (1) the β-γ phase transition proceeds gradually with changing temperature, or (2) only a single phase exists throughout the entire temperature range. In order to discriminate between the two, we have performed temperature-dependent Raman spectroscopy, which has been demonstrated to clearly distinguish between the β and γ phases of bulk $MoTe_2$ [1, 96, 97].

3.3   Raman spectroscopy measurement

Although the crystal structure between the two semimetallic $MoTe_2$ phases is subtle, it puts them in two different symmetry groups. In particular, β-$MoTe_2$ has inversion symmetry, whereas, γ-$MoTe_2$ is non-centrosymmetric. The makes it convenient for Raman spectroscopy measurement as Raman modes are sensitive to symmetry breaking. Studies on the Raman spectroscopy for the two phases found additional modes appear in the low-temperature phase [1, 97].

For Raman spectroscopy measurements, a light source, usually supplied by a laser, incidents on a material. The incident photon of energy $E_0 = h\nu_0$ may be absorbed by the system, simultaneously emitting a photon with energy $E_f = h\nu_f$. If the emitted photon has smaller energy, the reflected light's wavelength would have a smaller wavelength. This is known as Stokes Raman scattering. Alternatively, emitted photons that have more energy than the incident photons are called anti-Stokes Raman scattering. In the case of Rayleigh scattering, there is no energy difference between the incident and emitted light. The three cases are summarized in the energy diagram in Fig. 3.5(a). Not all vibrational modes will show up in the spectroscopy. There can be degenerate modes, and thus, would give rise to Raman scatter of the same frequency. Also, some modes are inactive due to symmetry reasons where the incident light is not able to induce a transition between the ground state and the virtual energy level [98]. For a vibrational mode to be Raman active, the motion of the vibration needs to change the molecule's polarizability. Before we dive into

23

(a)

Rayleigh scattering   Stokes scattering   Anti-Stokes scattering

virtual energy states

vibrational energy states

(b)

symmetric stretch
Raman active

asymmetric stretch
Raman inactive

Bending
Raman inactive
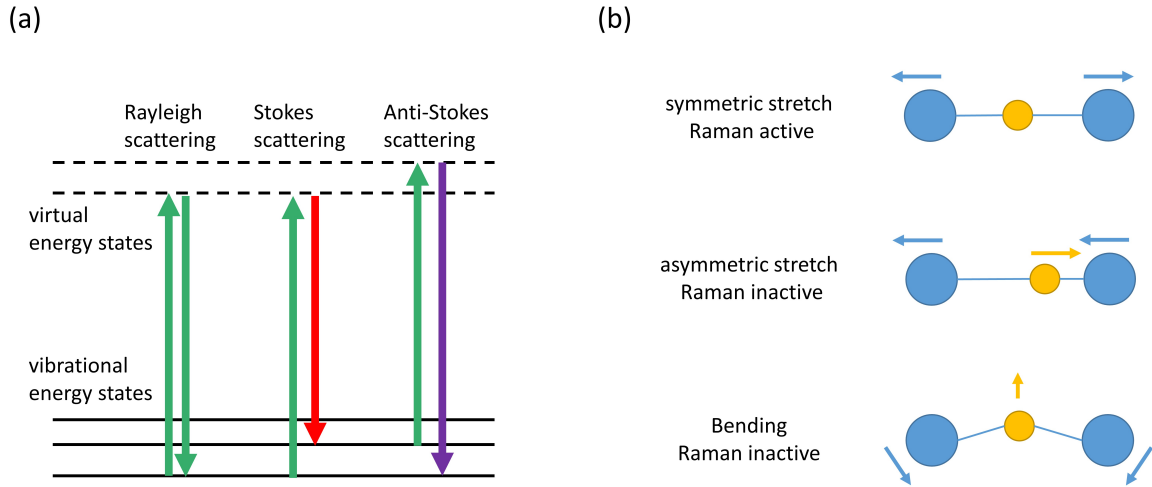
Figure 3.5: (a) Energy diagram showing the states involved in Raman spectroscopy. (b) Vibrational modes of carbon dioxide and their respective Raman activity.

$MoTe_2$, we examine a simpler molecule: carbon dioxide (CO_2). As a general rule, the total number of vibrational modes for linear molecules with N atoms is $3N - 5$ ($3N - 6$ for other molecules). For CO_2, it has one symmetrical stretch, one asymmetrical stretch and two bending vibrations. The vibrational modes of carbon dioxide and their corresponding Raman activity are shown in Fig. 3.5(b) [99]. In the symmetric stretching motion, both C-O bonds increased in length. The overall polarizability has changed and, thus, this mode is Raman active. In contrast, the asymmetry stretch vibration mode, one C-O bond is stretched and the other is compressed. The result net polarizability stays constant, which means this vibration mode is inactive. The third mode, a bending motion, does not involve the bond length change. Therefore, it is Raman inactive.

Next, we examine the Raman modes that are present in bulk β-$MoTe_2$ and γ-$MoTe_2$. Zhang et al. have calculated the possible Raman modes for β-$MoTe_2$ and γ-$MoTe_2$ [1]. Table 3.1 shows part of the calculated results where the Raman modes were observed. The Raman modes also depend on the polarization condition, which is given on the right side. The letter inside (outside) the parenthesis denotes the incident and reflection light's polarization (propagation) direction. Since more Raman modes are activated for $MoTe_2$

β-MoTe$_2$									a(bb)a	a(bc)a	a(cc)a	b(aa)b	b(ac)b	b(cc)b	c(aa)c	c(ab)c	c(bb)c
A$_g$	78 a	89 b	114 c	119 d	133 e	134 f	157 g	166 h	✓	✓	✓	✓		✓	✓		✓
B$_g$	93 i	98 j	112 k	115 l	200 m	204 n							✓			✓	
γ-MoTe$_2$																	
A$_1$	14 A	78 B	115 C	129 D	133 E	165 F					✓	✓		✓	✓		✓
A$_2$	98 G	112 H	115 I	192 J	200 K											✓	
B$_1$	93 L	115 M	119 N										✓				
B$_2$	89 O	119 P	121 Q	134 R	136 S	159 T				✓							

Table 3.1: Calculated Raman modes for β-MoTe$_2$ and γ-MoTe$_2$ in units of cm^{-1}. The letter for peak labeling is shown below the number. The right side is the polarization requirements for seeing the modes. The letter inside (outside) the parenthesis denotes the incident and reflection light's polarization (propagation) direction. The a-axis is defined parallel to the Mo-Mo zig-zag chain. Data in this table are taken from [1].

when it is in the γ phase, it can be used to distinguish between the two phases of MoTe$_2$.

Fig. 3.6(a) shows the setup used for Raman spectroscopy in this experiment. The laser light source first reflects off the first ultra-low frequency (ULF) filter, directing it onto the sample. Experimentally, the Rayleigh scattering signal is about three orders of magnitude stronger than Raman scatter [98]. In order to measure low-frequency Raman shifts, strong filters are used to damp out the Rayleigh scattering, allowing the Raman signal to be detected. We did not use polarizers as using non-polarized light is sufficient to distinguish between the two phases. The samples for Raman spectroscopy were prepared inside the nitrogen-filled glove to prevent oxidation. Since we are working with thin films that are $\ll 1$ μm thick, we can only shine laser light in the c-axis direction. By setting the light's propagation direction parallel to the crystal's c-axis, according to Table 3.1, only the A$_g$ and B$_g$ modes in β-MoTe$_2$ and A$_1$ and A$_2$ modes in γ-MoTe$_2$ are accessible. For a non-polarized light source, the Raman modes of the two phases are summarized in Table

β −MoTe$_2$	X	78	98	112	114	133,134		157,163	200
peak label		a	j	k	c	e,f		g,h	m
γ −MoTe$_2$	14	78	98	112	115	129	133	165	200
peak label	A	B	G	H	C,I	D	E	F	K

Table 3.2: Comparison of the calculated Raman modes for β-MoTe$_2$ and γ-MoTe$_2$ where the laser is unpolarized and propagates in the c-axis direction. Data in this table are from [1].

3.2. By comparing the Raman peaks of the two phases, most of the peaks overlap. The major difference is in the 14 cm^{-1}, 130 cm^{-1} and 165 cm^{-1} region. Although it is expected that β-MoTe$_2$ would have a double peak around 165 cm^{-1}, the h peak is very strong and overshadows the neighboring g peak.

We first performed Raman measurement on a 50 nm thick MoTe$_2$ at room temperature and low temperature. The results are shown in Fig. 3.6(b) and is comparable to the bulk MoTe$_2$ spectrum [1, 97]. γ-MoTe$_2$ shows a prominent peak around 13 cm^{-1} and a double peak around 130 cm^{-1}. In contrast, β-MoTe$_2$ does not have any peak below 20 cm^{-1} and only a single peak at 130 cm^{-1}. The low energy peak, labeled A, is associated with interlayer shear mode and is sensitive to stacking sequence, layer number and symmetry. The calculated vibrational pattern is shown beside the associated peaks [1]. The vibrations of the adjacent layers are in opposite directions, hence, the motion is odd parity when there is an inversion center. This results in an inactive Raman mode when MoTe$_2$ is in the centrosymmetric β phase [1]. These two regions can be used to distinguish between the two phases.

For the next part, we focus on the Raman data around the 13 cm^{-1} and 130 cm^{-1} region. For the top panel of Fig. 3.7(a), we first show Raman spectra for 50-nm- and 20-nm-thick flakes taken both at 294 K. For the lower traces, we compare Raman spectra for five thinner flakes of different thicknesses (4.5, 6, 7, 8.5, and 12.5 nm) taken at 294 K. Interestingly, they show similar features to bulk γ-MoTe$_2$ at low temperature and exhibit three peaks instead of one. In Fig. 3.7(b), we explicitly plot these peak positions as a

26
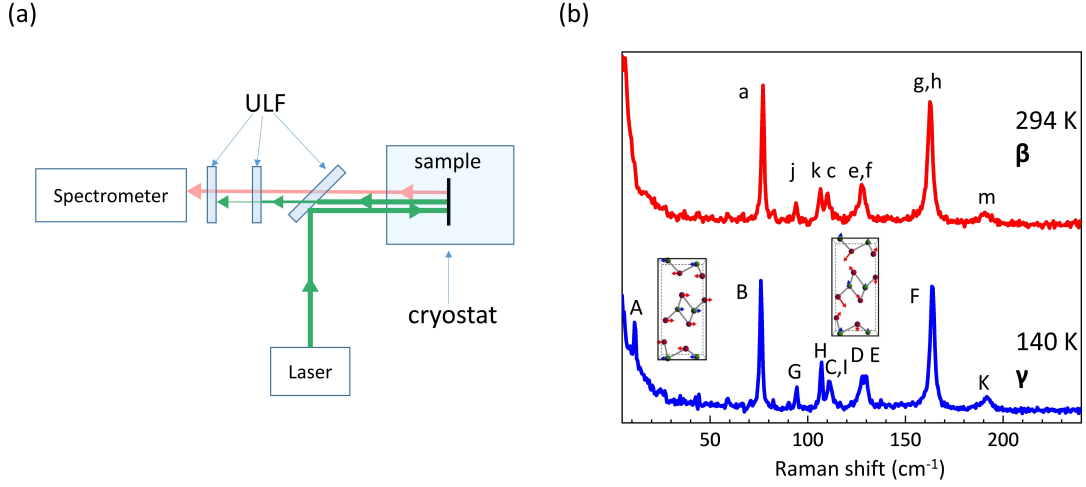
Figure 3.6: (a) Schematic of the Raman spectroscopy setup used for this thesis. (b) Raman spectroscopy of bulk MoTe$_2$ at room temperature (β phase) and low temperature (γ phase). Schematic of the two Raman modes that are activated due to the phase transition, A and D peak, is shown next to them. The schematics are adapted from [1], reused under Creative Commons license CC BY 4.0.

function of flake thickness. We have also marked with dashed lines the energies of modes A, D, and E observed in 50-nm MoTe$_2$ within the γ phase at 140 K. Overall, the thin flake modes redshift with decreasing sample thickness. Similar softening has been observed in other TMDC materials and could be due to a reduced interlayer force constant in few-layer systems [100–102]. The extrapolation of these mode positions to the bulk γ-phase peaks in the thick limit, however, indicates that thin MoTe$_2$ ($\simeq$12 nm) exhibits the inversion symmetry breaking orthorhombic structure at room temperature. We thus designate these three peaks as A, D, and E in direct connection with this phase.

In order to confirm that the γ phase is established across the entire measured temperature range for thin samples [scenario (2)], it is necessary to perform Raman measurements with changing temperature. In the main panel of Fig. 3.8(a), we plot the evolution of Raman spectra for another 4.5-nm-thick sample upon both cooling to 150 K and warming to 400 K. The A, D, and E modes characteristic of the γ phase can be seen at all temperatures. We have fitted these three peaks with Lorentzian line shapes and plotted their
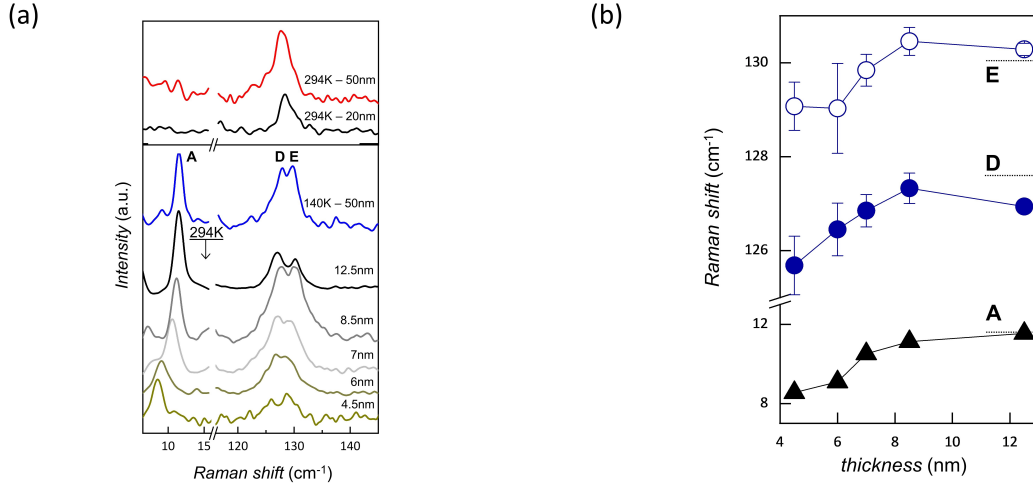
Figure 3.7: (a) Main panel, top two traces: Raman spectra of 50- and 20-nm MoTe$_2$ at room temperature resembling the β phase. Lower traces: Spectra of 50-nm MoTe$_2$ at 140 K (γ phase) and thinner flakes at 294 K. (b) Raman mode positions vs thickness for γ-MoTe$_2$ flakes at 294 K. Corresponding mode positions for the 50-nm sample at 140 K are marked by dashed lines.

temperature-dependent mode positions and areal intensities in Fig. 3.8(b). The modes redshift with increasing temperature, and increasingly so above room temperature. For cooling below 300 K, the intensity of peak E grows gradually with decreasing temperature, while the intensities of A and D slightly decrease. None of these modes, however, display large, abrupt changes characteristic of a first-order β-γ phase transition as in the bulk crystal at $\sim$250 K [1, 97]. For heating close to 400 K, the intensities of all three peaks decrease, which could indicate the beginning of a transition into another phase different from both the β and γ phases.

In order to rule out the effect of the hBN on the observed dimensional crossover, we have compared Raman spectra between bare hBN, *thick* MoTe$_2$ uncovered and covered with hBN, as well as *thin* MoTe$_2$ covered with hBN and graphite. The data is shown in Fig. 3.9(a). Due to the effect of surface oxidation, we are not able to study pristine thin MoTe$_2$ that is unprotected. hBN does not possess any Raman modes at the range of frequencies studied here. Furthermore, the precise structure of the capping layer does not seem to
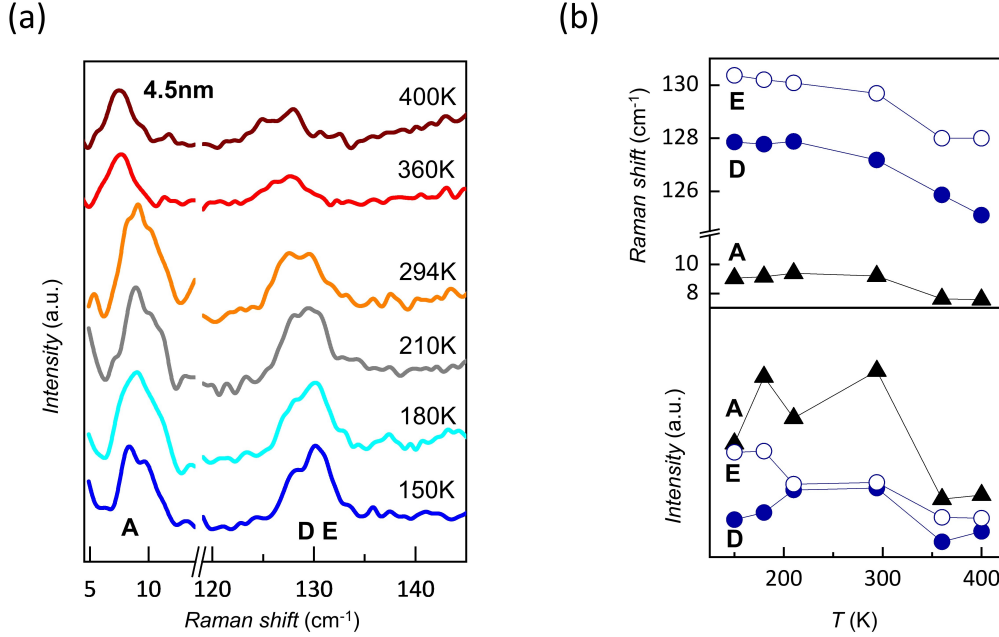
Figure 3.8: (a) Temperature evolution of Raman spectra for the 4.5-nm sample upon cooling and heating from room temperature. (b) Mode positions and areal intensities vs temperature after Lorentzian fits. Traces have been offset for clarity. No abrupt changes at ~250K corresponding to a first-order β-γ phase transition are observed.

affect the β-γ phase transition of the underlying MoTe$_2$. For Raman measurements at low temperatures, samples were loaded inside a cryostat whose optical window gives a rising background for ultra-low frequencies near the laser line. In Fig. 3.7(a) and Fig. 3.8(a), we have removed this background to compare better with the other spectra measured outside the cryostat. In Fig. 3.9(b), we show the original low-temperature data shown in Fig. 3.8(a) along with the room temperature spectra measured outside for comparison.

3.4   Discussion

The combined results of our Raman and transport study can be summarized by the temperature-thickness phase diagram shown in Fig. 3.10(a). For samples 12.5 nm and
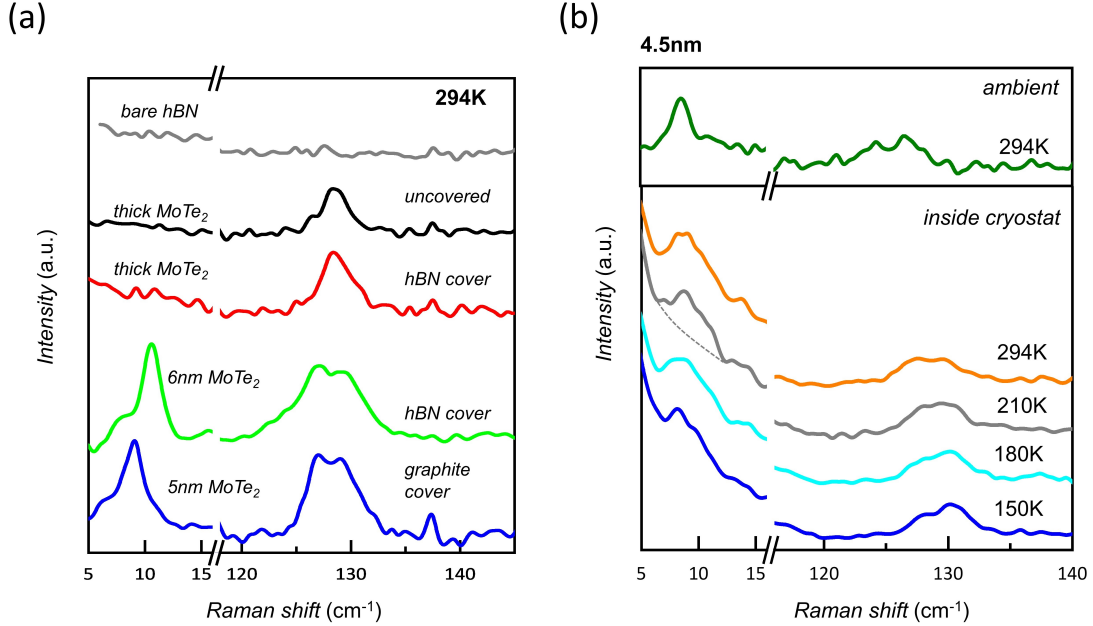
Figure 3.9: (a) Raman comparison between bare hBN and MoTe$_2$ with different capping conditions. (b) Comparison between ultralow-frequency spectra taken outside the cryostat (upper trace) with those taken in the cryostat. The cryostat window gives a rising background as well as a shoulder at $\sim$10 cm^{-1}. The gray dashed line shows a guide-to-eye example of the background signal.

thinner, the γ phase is stabilized at all temperatures up to 400 K. For thicker samples, a phase boundary separates the low-temperature γ phase from another high-temperature phase, which in the limit of a bulk crystal is the β phase. We have used the center temperature of the resistivity hysteresis to mark this phase boundary down to 50 nm [see Fig. 3.3]. The smallest thickness measured for which the γ phase is not observed in Raman at room temperature is 20 nm (see Fig. 3.7(a)). We have cooled this sample and determined that it transitions to the γ phase at $\sim$210 K. This indicates that the transition temperature does not change substantially with decreasing thickness, but rather terminates abruptly for a critical thickness (between 12.5 and 20 nm), below which only a single γ phase exists.

What is the nature of the high-temperature phase? If we take the resistivity dif-

ference in the hysteresis region as an indicator of the difference between the high- and low-temperature states, its decrease with decreasing thickness (see Fig. 3.3(b)) indicates that the β phase undergoes a slow crossover as thickness is reduced from the bulk limit. This indicates thickness driven β-γ phase transition is gradual until the γ phase is reached below the critical thickness. This is illustrated in Fig. 3.10(a) by the fading colors.

We now examine the possible mechanisms for the stabilization of γ-MoTe$_2$ in thin samples. First, since the hysteresis already weakened for the 180 nm sample, it is unlikely that the cause is surface or substrate effects impacting the top- or bottom-most layers [103, 104]. Second, since the Raman peak positions of thin γ-MoTe$_2$ are overall very similar to their bulk counterparts, especially for slightly thicker flakes close to 10 nm, we can also rule out the possibility of changing interlayer interactions driving the crossover [100–102]. Instead, we look to the 3D origins of the β-γ transition in bulk systems.

Recently, Kim *et al.* has calculated the electronic structure of bulk MoTe$_2$ across this phase transition [10]. Starting in the β phase, they find that there are two hole pockets that cross the Fermi energy in the out-of-plane, Γ-to-A direction. In addition to changes in the in-plane band structure, the upper c-axis hole band shifts to lower energy upon a transition into the γ phase. In comparison, for WTe$_2$, a structurally similar compound which always exists in the γ phase, the corresponding hole bands sit below the Fermi level. As a consequence, Kim et al. predict that γ-MoTe$_2$ can be stabilized by electron doping.

When samples are thin enough, quantum confinement will have a significant impact on the band structure. This can be understood in terms of the classic particle in a box example. When the box is very small, the ground state energy level shifts upward. Similarly, when samples approaches the monolayer limit, the electron (hole) band will shift upwards (downwards). Quantum confinement produced by thickness reduction may yield a similar stabilization of the orthorhombic γ phase by pushing the hole bands to lower energy. In the main panel of Fig. 3.10(b), we have used the results of Kim et al. and added a c-axis confinement energy, $\Delta E = \frac{\hbar^2 \pi^2}{2m_\perp L^2}$, to the β hole band for various thicknesses L (20, 10, 7, and 5 nm) by evaluating the effective mass through a numerical derivative ($m_\perp \sim 1.18 m_e$). Comparing to the corresponding band in the γ phase, we observe that thickness reduction results in a continuous shift of the β-phase band towards that of the γ phase. In particular, as shown in the inset, the confined β band energy at the point crosses the γ band for

31
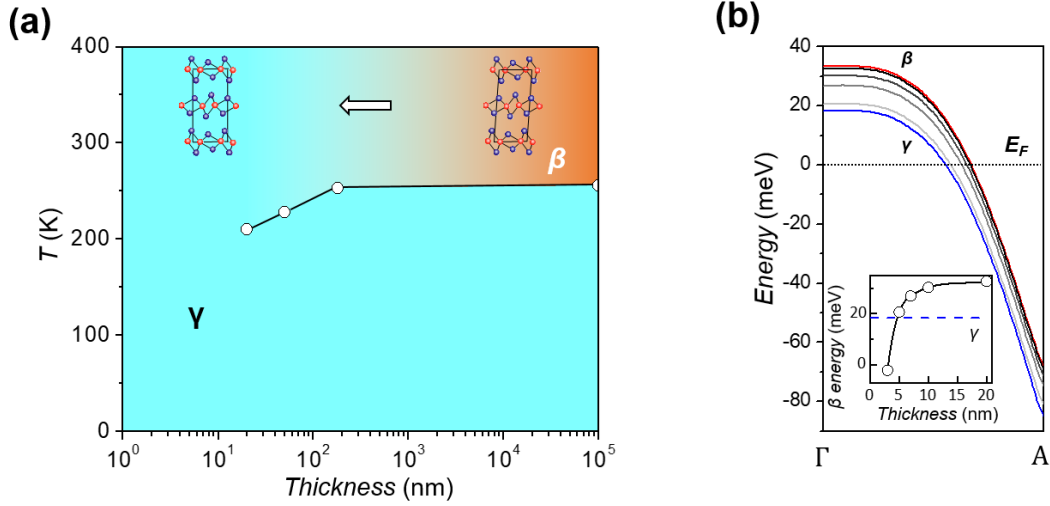
Figure 3.10: (a) Temperature-thickness phase diagram. Below a critical thickness, a single γ phase is stabilized at all temperatures up to 400 K. The high-temperature β phase undergoes a crossover with reducing thickness, likely due to a slowly changing structure. (b) Main panel: Proposed mechanism for crossover. An out-of-plane hole band is shifted to lower energy upon cooling in thick samples and confinement in thin samples. Red and blue traces are reproduced from Kim et al. [10] and correspond to bulk $MoTe_2$ in the β and γ phase, respectively. Gray traces correspond to the β band confined to thickness 20, 10, 7, and 5 nm. Inset: β band energy vs thickness at the Γ point, showing crossing below the γ-phase energy (dashed blue line) at $\sim$5 nm.

thicknesses under $\sim$5 nm. This critical thickness is less than but within the same order of the experimentally determined value, which could be due to an overestimate of the true effective mass and/or suggests that it may be necessary to consider the complete Fermi surface in order to fully substantiate this scenario. This simple analysis nevertheless provides for both a reasonable estimate of the critical thickness and accounts for the changes we observe in samples beyond the few-layer limit. An analogy may also be made to the semiconducting TMDCs, such as MoS_2 and WSe_2. For these materials, since the out-of-plane effective mass for both electrons and holes at the K point is much larger than those closer to the Γ point, decreasing thickness leads to a large confinement energy increase for

32

the indirect gap, while the direct gap is relatively unchanged [31].

3.5 Latest developments

Since the publication of our findings in 2018 [105], further investigations were done by other researchers. A photoemission electron microscopy study by Pawlik et al. have shown the Fermi level shifts upwards for thin $MoTe_2$ that was prepared by exfoliation [106]. Although this result does not serve as evidence for the establishment of γ phase in thin $MoTe_2$, it is consistent with our proposed mechanism. Rather than looking at pristine $MoTe_2$, Paul et al. took another route. They purposely introduced doping in $MoTe_2$ and examined the results. Depending on the doping level, thin $MoTe_2$ can be in either of the β or γ phases in temperatures between 80 and 300 K [107].

Cheon et al. also performed layer-dependent Raman spectroscopy for $MoTe_2$ down to monolayer [11]. They were able to reproduce what we have reported, however, they also found different results for flakes of the same thickness. By analyzing the Raman spectroscope of several 7-layers-thick $MoTe_2$ samples, three scenarios were observed: transition, intermediate and no transition from β to γ phase. Similar situations were also observed for other thickness and are summarized in Fig. 3.11(a). Based on their data, they believe there should be metastable intermediate phases between the β and γ phases.

Hart et al., on the other hand, have used a variety of experimental techniques including scanning transmission electron microscopy (STEM), *in situ* cryogenic TEM, electron diffraction measurements, electronic resistance measurements and Raman spectroscopy to examine the structure of semimetallic $MoTe_2$ [12]. In their measurements, bulk $MoTe_2$ shows well-defined β and γ phase structures, while thinner flakes are best described as "disordered". In other words, thin $MoTe_2$ does not have a strong preference for either the β or γ stacking. To rule out measurement artifacts due to the sample being in the thin limit, they confirmed thin WTe_2 shows a similar structure as the bulk form. They concluded by presenting a temperature-thickness phase diagram shown in Fig. 3.11(b).
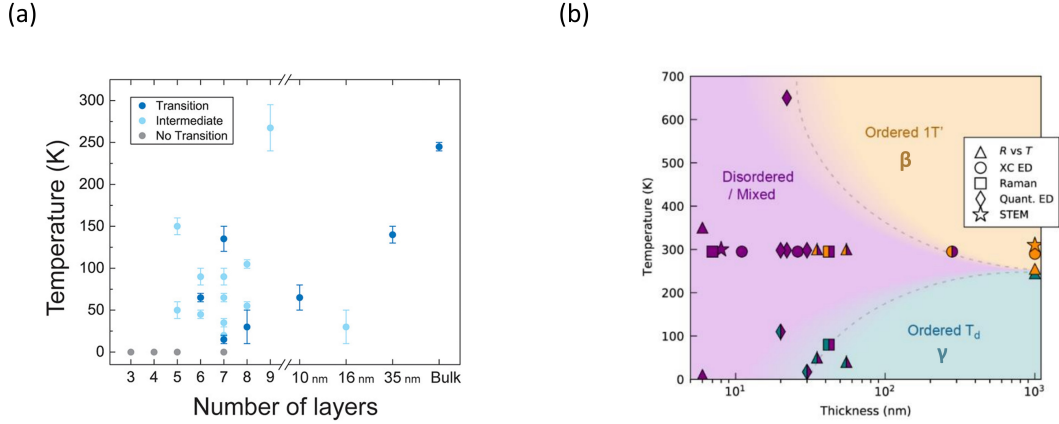
Figure 3.11: (a) Observed layer dependent phase transitions for MoTe$_2$. The critical temperature for transitioning into the γ phase and intermediate phase are represented by blue and cyan dots, respectively. Grey dots at 0 K represent no transition was observed. Figure adapted from [11], copyright (2021) American Chemical Society. (b) Phase diagram of thin MoTe$_2$ as a function of thickness and temperature based on different experimental methods. The color represents the phase and shape represent experimental type. R vs T indicates electrical resistance measurements, XC ED stands for cross-sectional electron diffraction, and Quant. ED stands for quantitative electron diffraction. Figure adapted from [12], reused under Creative Commons license CC BY 4.0.

3.6 Conclusion

In summary, our transport measurements show thin flakes exfoliated from β-MoTe$_2$ show semimetallic behavior. We observe no phase transition in semimetallic MoTe$_2$ flakes thinner than ~12 nm for temperatures below 400 K. This observation has been reproduced by various other groups. The actual crystal structure, however, is not consistent among different reports. Based on our Raman spectroscopy results, we believe it remains in a single orthorhombic phase. Among different possible causes, we considered the effect of perpendicular confinement on out-of-plane hole bands. We expect that this shift will have measurable effects on the transport properties of thin samples, especially at low temperatures where the electron and hole concentrations are balanced in the bulk crystal.

Chapter 4

Magnetotransport in thin MoTe$_2$

4.1 Introduction

4.1.1 Magnetoresistance

Magnetoresistance (MR) is the change in resistance with respect to an external magnetic field. Two well known types of MR are the giant MR (GMR) and colossal MR (CMR). GMR was realized in multilayer systems that consist of alternating magnetic and non-magnetic layers [108]. The observed percentage change in resistance at room temperature can be as large as 70%, which is much larger than that of the individual layers [109]. CMR, on the other hand, is observed in certain manganite perovskites where the change in resistance can be thousandfold at cryogenic temperatures [110]. MoTe$_2$, being a non-magnetic material, extremely large MR is also observed at low temperatures [13, 14, 58, 60]. As shown in Fig. 4.1(a), the resistance does not vary much with the external magnetic field at temperatures above 40 K. However, at 2 K, the MR increased by 3 orders of magnitudes at 9 T [13]. Plotting it in linear scale, shown in Fig. 4.1(b), the MR increases quadratically without saturation up to 60 T [14]. Note that the MR starts to show oscillatory behavior for magnetic fields beyond 20 T. This is known as Shubnikov-de Haas (SdH) oscillations and will be discussed in Sec. 4.1.2. The main reason for the large magnetoresistance is attributed to the compensation of electron and hole carriers. Since the calculated band
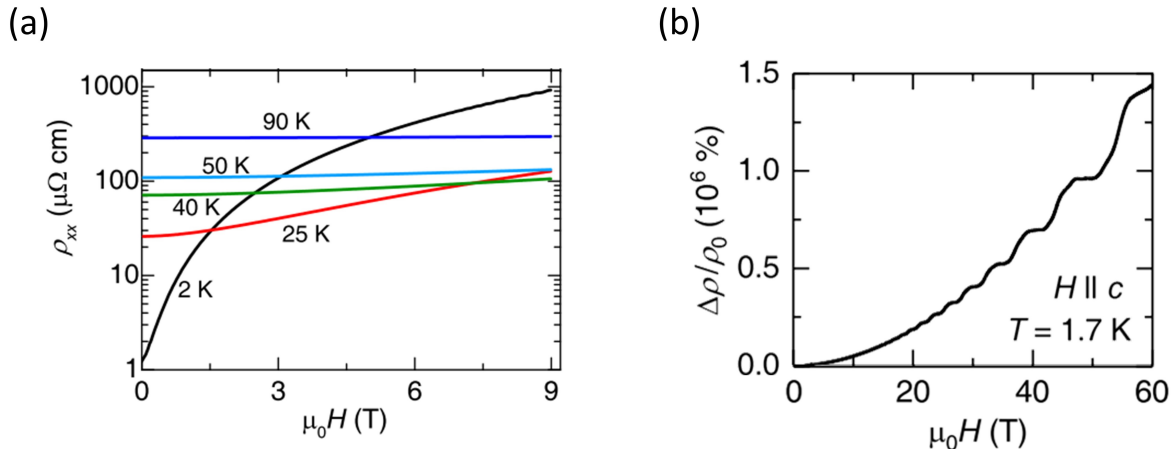
Figure 4.1: (a) Longitudinal resistivity ρ_{xx} of bulk γ-MoTe$_2$ as a function of external magnetic field μ_0H for several temperatures between 2 and 90 K. Figure adapted from [13], copyright (2016) by the American Physical Society. (b) MR(%) of bulk γ-MoTe$_2$ at 1.7 K for magnetic fields up to 60 T. Figure adapted from [14], copyright (2017) by the American Physical Society.

structure of γ-MoTe$_2$ shows the Fermi level crosses both the electron and hole bands. Hence, it is expected that both carrier species contribute to the electric conductance. When the two carrier densities are comparable, MR should increase quadratically with external magnetic field. Following the semiclassic approach by Pippard [111], the conductivity is given by

$$\sigma_0 = ne^2\tau/m^* = e\mu, \tag{4.1}$$

where n is the number of electron per unit volume, m^* is the effective mass, τ is the relaxation time and μ is the mobility. If an external magnetic field, $\mathbf{B}$, is applied, the electrons will experience a Lorentz force, $F = e\mathbf{v} \times \mathbf{B}$, where $\mathbf{v}$ is the velocity of the electron. This force bends the electron's trajectory into helices that are in the plane perpendicular to $\mathbf{B}$, with a cyclotron frequency of

$$\omega_c = eB/m^*. \tag{4.2}$$

Generally speaking, the magnetic field needs to be strong enough to have a significant impact on the MR. The conductivity can be expressed in tensor notation where it satisfies

$$J_i = \sigma_{ij} E_j, \tag{4.3}$$

where J_i is the current density and E_j is the applied electric field. If we set the external magnetic field in the z-direction, ie. $\mathbf{B} = B_z \hat{z}$, the conductivity tensor would be given by

$$\sigma_{ij} = \begin{pmatrix} \sigma_0/(1+\xi^2) & -\xi\sigma_0/(1+\xi^2) & 0 \\ \xi\sigma_0/(1+\xi^2) & \sigma_0/(1+\xi^2) & 0 \\ 0 & 0 & 1/\sigma_0 \end{pmatrix}, \tag{4.4}$$

where $\xi = \omega\tau$. It is more convenient to represent the $x - y$ plane as a complex plane where $\mathbf{E}$ and $\mathbf{J}$ are represented by complex numbers. They are linearly related by $\hat{\sigma} = \sigma_{xx} - i\sigma_{xy}$. From the above matrix, the in-plane conductivity can also be written as:

$$\hat{\sigma} = \sigma_0/(1 - i\xi) = \frac{en\mu}{1 - i\mu B}. \tag{4.5}$$

Now, let's consider the two-band model where both electron and hole contribute to the conduction independently. In such case, the two species differ only by a negative sign and the total conductivity tensor can be expressed as

$$\hat{\sigma}_T = e\left[\frac{n\mu_n}{1 - i\mu_n B} + \frac{p\mu_p}{1 + i\mu_p B}\right], \tag{4.6}$$

where n (p) and μ_n (μ_p) refer to the electron (hole) concentration and mobility, respectively. Isolating it into σ_{xx} and σ_{xy} would result in

$$\sigma_{xx} = e\left[\frac{n\mu_n}{1 + (\mu_e B)^2} + \frac{p\mu_p}{1 + (\mu_h B)^2}\right], \tag{4.7}$$

$$\sigma_{xy} = eB\left[\frac{n\mu_n^2}{1 + (\mu_e B)^2} - \frac{p\mu_p^2}{1 + (\mu_h B)^2}\right]. \tag{4.8}$$

The above two equations can be used to fit to experimental data. However, since resistivities are measured directly, it would be convenient to have an expression for ρ_{xx} and ρ_{yx}. Taking the reciprocal of $\hat{\sigma}_T$ gives

$$\hat{\rho} = \frac{1 + \mu_n\mu_p B^2 + i(\mu_n - \mu_p)B}{e(n\mu_n + p\mu_p + i(p - n)\mu_n\mu_p B)}. \tag{4.9}$$

The experimentally observed longitudinal (Hall) resistivity would be the real (imaginary) part of $\hat{\rho}$, namely

$$\rho_{xx}(B) = \frac{(n\mu_n + p\mu_p) + (n\mu_p + p\mu_n)\mu_n\mu_p B^2}{e[(n\mu_n + p\mu_p)^2 + (p-n)^2\mu_n^2\mu_p^2 B^2]}, \tag{4.10}$$

$$\rho_{yx}(B) = \frac{(p\mu_p^2 - n\mu_n^2)B + (p-n)\mu_p^2\mu_n^2 B^3}{e[(n\mu_n + p\mu_p)^2 + (p-n)^2\mu_n^2\mu_p^2 B^2]}. \tag{4.11}$$

If $n = p$, the first equation simplifies to MR=$\mu_n\mu_p B^2$, thus yielding unsaturating MR with a quadratic field dependence. Qualitatively, this result matches the MR observed in bulk γ-MoTe$_2$ as shown in Fig. 4.1(b) [14].

The two-band model can also be used to give more quantitative information. The $\sigma_{xx}(B)$ and $\sigma_{xy}(B)$ data can be fitted by Eq. 4.7 and Eq. 4.8 to give the carrier density and mobility of the two species. This analysis has been done by Zhou et al. as shown in Fig. 4.2(a) [13]. Note that resistivities, ρ_{xx} and ρ_{yx}, were measured directly and converted to conductivity using the relation $\sigma_{xy} = -\rho_{yx}/(\rho_{yx}^2 + \rho_{xx}^2)$. Based on the fit, the extracted electron and hole carrier density is shown in Fig. 4.2(b) with their ratio given in the inset. Electron carrier dominates at high temperatures, while hole carrier starts to grow rapidly below ∼40 K. The carrier density ratio reaches unity below ∼15 K, consistent with the observed extremely large magnetoresistance temperature range. Therefore, this gives quantitative evidence that bulk MoTe$_2$ has comparable electron and hole carriers at low temperatures.

4.1.2 Quantum oscillations

Under high enough magnetic fields, Landau levels may start to become quantized. This would manifest as oscillations in the resistance as the magnetic field increases. This effect was first observed by Shubnikov and de Haas in 1930 [112, 113]. This has become what is now known as the SdH oscillations. Later, a theory was proposed by Adams and Holstein involving detailed problem of electron scattering in a magnetic field [114]. However, as a qualitative analysis, SdH oscillations can be explained in simpler way [115]. For the quantum mechanical approach, the Hamiltonian of a free electron gas with an external

(a)

(b)
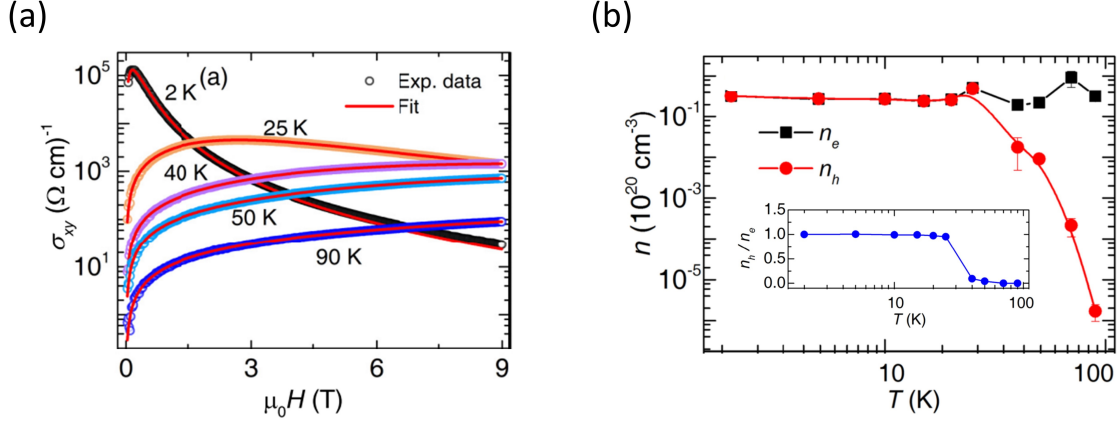
Figure 4.2: (a) γ-MoTe$_2$'s σ_{xy} as a function of magnetic field for several temperatures ranging from 2 to 90 K. Open circles represent the experimental data while solid lines are the fitting curves based on the two-band model. (b) The carrier density of the electron and hole carrier extracted from the fit in (a). Inset shows the density ratio of the two species as a function of temperature. Both figures adapted from [13], copyright (2016) by the American Physical Society.

magnetic field, $\mathbf{B} = (0, 0, B_z)$, is given by

$$\hat{H} = \frac{1}{2m^*}(\hat{\mathbf{p}} + e\mathbf{A})^2, \tag{4.12}$$

where $\hat{\mathbf{p}} = -i\hbar\nabla$ is the momentum operator and $\mathbf{A}$ is the vector potential that satisfies $\mathbf{B} = \nabla \times A$. It is convenient to choose the Landau gauge, $\mathbf{A} = (0, B\hat{x}, 0)$, and the Hamiltonian becomes

$$\hat{H} = \frac{1}{2m^*}(\hat{p}_x^2 + (\hat{p}_y - eB\hat{x})^2 + \hat{p}_z^2). \tag{4.13}$$

Substitute the cyclotron frequency $\omega_c = eB/m^*$ and we have

$$\hat{H} = \frac{\hat{p}_x^2}{2m^*} + \frac{1}{2}m^*\omega_c^2\left(\frac{\hat{p}_y}{m^*\omega_c} - \hat{x}\right)^2 + \frac{\hat{p}_z^2}{2m^*}. \tag{4.14}$$

Since $\hat{p}_y$ commutes with the Hamiltonian, it can be replaced with its eigenvalue. Let the wave function take the form of $\Psi(x, y, z) = e^{i(k_y y)}X(x)Z(z)$. The Hamiltonian can be

39

further reduced to

$$\hat{H} = \frac{\hat{p}_x^2}{2m^*} + \frac{1}{2}m^*\omega_c^2(\hat{x} - \frac{\hbar k_y}{m^*\omega_c})^2 + \frac{\hat{p}_z^2}{2m^*}. \tag{4.15}$$

The above Hamiltonian is a quantum harmonic oscillator with a shift in real space and free motion along the z-direction. Therefore, the energy eigenvalues are given as

$$E_n = \hbar\omega_c(n + \frac{1}{2}) + \frac{\hbar^2 k_z^2}{2m^*}. \tag{4.16}$$

This is known as Landau quantization. Each Landau level can be visualized as a Landau
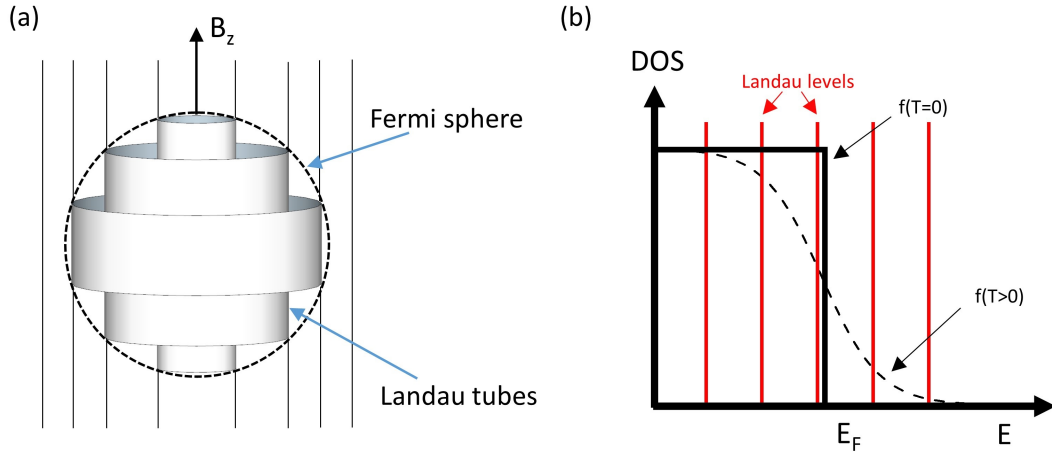
Figure 4.3: (a) Schematics of Landau tubes crossing the Fermi surface. (b) The density of states of 2DEG in a strong magnetic field where the Landau levels are delta peaks. The Fermi-Dirac distribution is a step function at T=0 K and widens for finite temperatures.

tube in momentum space as shown in Fig. 4.3(a). Assuming the Fermi surface is spherical and at T=0 K, only states within the Fermi sphere will be occupied. This is very similar to the 2D electron gas in strong magnetic fields. The density of states (DOS) are delta functions as shown in Fig. 4.3(b). As the magnetic field increases, the Landau levels move to higher energy. In the 3D case, that would be represented by increase of Landau tubes' radius. According to the Onsager's relation, the cross-section area of the Landau tubes is given by

$$a = (n + \frac{1}{2})2\pi eB/\hbar. \tag{4.17}$$

The occupied states will eventually vanish when a equals the extremal cross-section area, A_F, of the Fermi sphere. Successive crossing happens when Landau tubes of smaller energy level passes through the Fermi surface. The passings are periodic with respect to $1/B$. Experimentally, it's more convenient to measure the frequency of the passings, $1/\Delta(1/B)$, and is given by

$$F = \frac{1}{\Delta(1/B)} = (\Phi_0/2\pi^2)A, \tag{4.18}$$

where $\Phi_0 = h/2e$ is the magnetic flux quantum. Geometrically, the radius of A_F is just the Fermi wave vector, k_F, and they are related by $A = \pi k_F^2$. To calculate the carrier density, assume a box with volume, V. Then, the smallest unit in reciprocal space would be π^3/V. The volume of the Fermi sphere is given by $V_F = \frac{4}{3}\pi k_F^3$. The total number of states within the Fermi sphere is $N = \frac{1}{4}\frac{V_F}{\pi^3/V}$. Finally, the carrier density is $N/V = \frac{k_F^3}{3\pi^2}$. Although not all materials have Fermi surfaces in the form of a sphere, it provides an estimate of the carrier density.

The above analysis assumes T=0 K, where the Fermi distribution is like a step function. As the temperature increases, the extremal of the Fermi sphere is broadened, thus, affecting the Landau level's occupancy states when it passes through. Again, this is easier to visualize in the 2D case in Fig. 4.3(b). This results in a lower oscillation amplitude, R_T, and its dependence on temperature can be described by the Lifshitz-Kosevich (LK) relation [116]

$$R_T = \frac{X}{sinh(X)}, \tag{4.19}$$

where

$$X = \frac{2\pi^2 k_B T m^*}{\hbar e B}. \tag{4.20}$$

This is a very useful relation as the only unknown parameter is the effective mass. Therefore, it can be deduced by measuring the magnitude quantum oscillations at different temperatures.

Previous studies have shown bulk γ-MoTe$_2$ exhibits SdH oscillations at high fields (see Fig. 4.1(b)) [14]. The lower trace of Fig. 4.4(a) shows the result of a typical SdH with the quadratic background removed [14]. The top trace shows another type of quantum
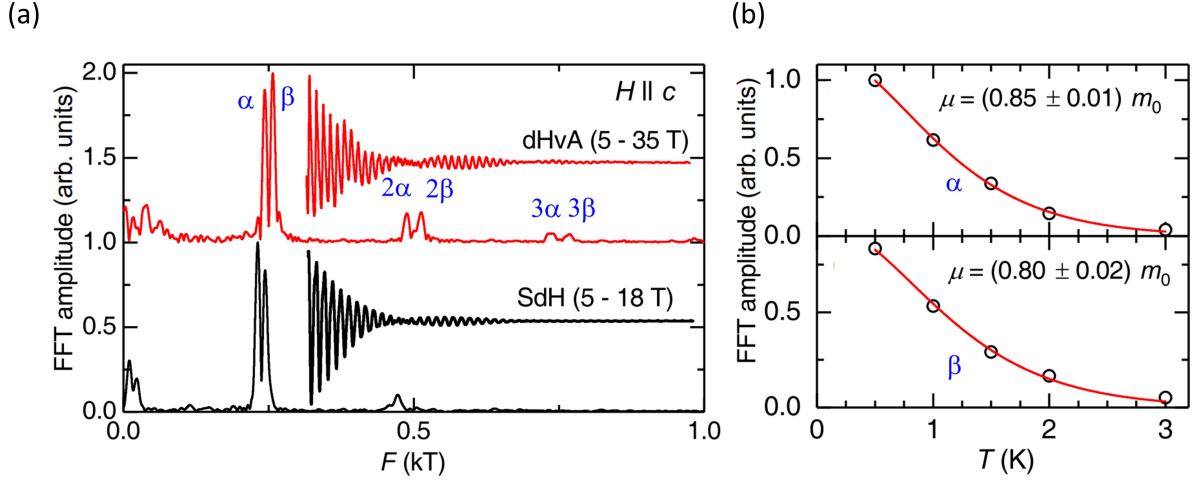
Figure 4.4: (a)Typical dHvA (red trace) and SdH (black trace) signals superimposed onto the magnetic torque and the magnetoresistivity, respectively, of bulk γ-MoTe$_2$. (b) Amplitude of the peaks observed in the FFT as a function of temperature. The red curve is the fitting using the LK formula. Both figures adapted from [14].

oscillation, the de Haas-van Alphen (dHvA) oscillation. This effect is an oscillation of a sample's magnetic susceptibility as the magnetic field increases [117]. Both SdH and dHvA oscillations are closely related, but the latter will not be discussed in this thesis. Taking the fast Fourier transform (FFT) of the SdH can reveal the oscillation frequency, which is also shown in Fig. 4.4(a). Two main peaks are observed in bulk γ-MoTe$_2$. The oscillating amplitude decreases due to thermal effects. Therefore, the FFT amplitudes of the peaks would also decrease accordingly. Fig. 4.4(b) shows the amplitude of the peaks observed in the FFT as a function of temperature. The LK (Eq. 4.19) formula was used for the fitting to extract the effective masses.

As mentioned in the previous chapter, Chapter 3, the γ phase is realized in thin MoTe$_2$ samples (below ~12 nm) at all temperatures up to 400 K, potentially allowing for the observation of Weyl nodes and their surface states under ambient conditions. The cause has been attributed to the c-axis confinement of the hole bands. For the bulk crystal, it has been calculated that both electron and hole pockets shrink when cooling from the β to γ phase [10], and so it is possible that reducing thickness similarly stabilizes the latter

at higher temperatures by confining the hole bands to lower energy.

In principle, these differences for thin samples should have a marked effect on the magnetoresistance (MR) at low temperatures, provided that charge compensation is responsible for the extremely large magnetoresistance (XMR) [58]. Namely, we expect that a changing electronic structure would alter the delicate carrier balance achieved in the bulk crystal. We have performed both longitudinal and transverse magnetotransport measurements on MoTe$_2$ flakes at 300 mK as a function of thickness. Not only do we observe lower MR in thin samples, fittings to a two-band model surprisingly show a decrease in both the absolute and relative carrier concentrations as well as their mobilities. This is qualitatively consistent with the measurement of SdH oscillations, which provides an independent measure of the Fermi surface. By modeling the different effects separately, we conclude that the MR is more sensitive to changes in carrier mobility, and that, in principle, relatively large MR values can be achieved with a moderate degree of charge imbalance.

4.2   Experimental Results

A schematic of the device setup is shown in Fig.4.5(a). The longitudinal(V_{xx}) and Hall (V_{yx}) voltages are measured using the standard 4-probe method. Fig. 4.5(b) shows an optical image of a representative device. In the main panel of Fig. 4.5(c), we show temperature-dependent resistivity for three representative MoTe$_2$ samples of different thicknesses (7, 50, and 180 nm) prepared in this manner. The traces are normalized to the resistivity at 280 K and are offset for clarity. All show metallic characteristics in contrast with an earlier report on unprotected thin flakes, which observes insulating behavior for thicknesses below ∼10 nm [58].

As discussed in Chapter 3, the hysteresis loop associated with the β-γ transition at ∼250 K gradually disappears for decreasing thickness as a single γ phase is stabilized in thin flakes for the entire temperature range [105]. Below ∼10 K, the resistivity saturates to a temperature-insensitive, residual value. In the inset, we have explicitly plotted the residual resistivity for all of the samples measured in this work (eight in total) at 300 mK. There is variation between samples, up to two orders of magnitudes. During the sample
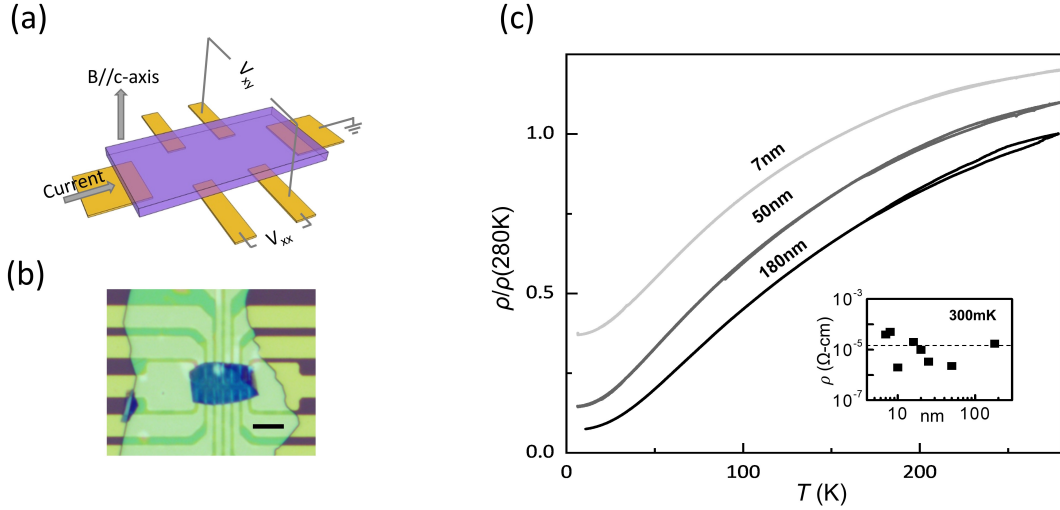
Figure 4.5: (a) Schematic of the device geometry used in this experiment. (b) An optical image of the MoTe$_2$ on pre-patterned electrodes covered with hBN. (c) Normalized resistivity as a function of temperature for three MoTe$_2$ flakes of different thicknesses. An offset was applied to the upper traces for clarity. Inset: Residual resistivity of all samples measured at 300 mK. The dashed line marks the average resistivity.

preparation, we did not deliberately choose a specific crystal axis to source the current. In bulk MoTe$_2$, the resistivity ratio between the a- and b-axis is about a factor of 2 [9, 118]. This ratio probably does not change much in thin materials [61]. Hence, the anisotropy among the different axis alone does not explain the orders of magnitude difference across all samples. The average residual resistivity 1.8×10^{-5} Ωcm (marked by dashed line) is comparable to that of the bulk crystal ($\sim 10^{-5}$ Ωcm) [60], indicating that our flakes have not degraded during the preparation process.

4.2.1 Magnetoresistance in thin MoTe$_2$

The longitudinal resistivity, ρ_{xx} and thus MR, should be symmetric with respect to magnetic field direction, while the transverse resistivity ρ_{yx} should be antisymmetric. In practice, however, there is some deviation due to mixing between the two signals. We

44
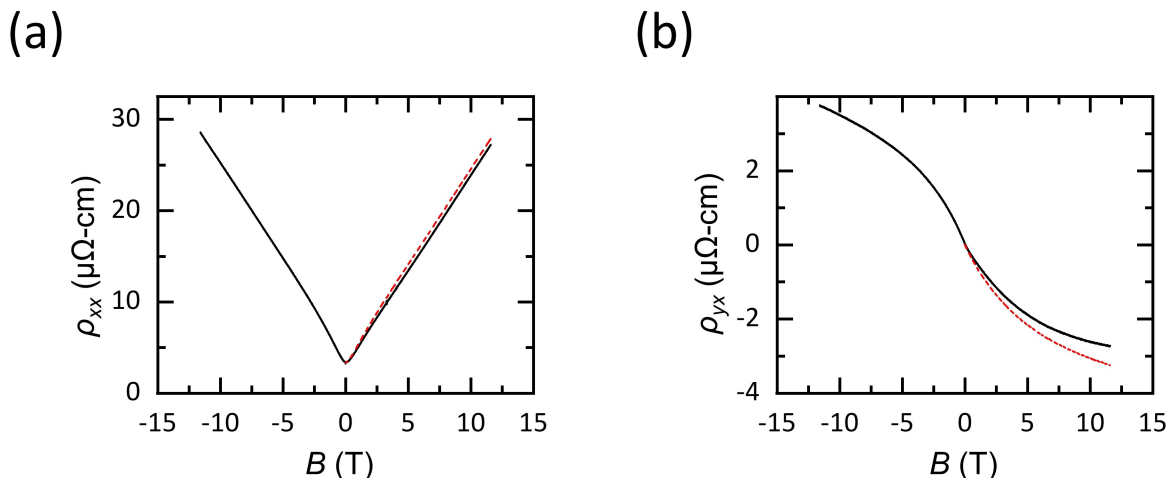
Figure 4.6: The measured longitudinal and transverse resistivity for a representative (25 nm) sample shown in (a) and (b), respectively. The (anti-)symmetrized data is plotted in red dashed lines.

thus symmetrized ρ_{xx} and anti-symmetrized ρ_{yx} by: $\rho_{xx}(B > 0) = \frac{\rho_{xx}(B)+\rho_{xx}(-B)}{2}$ and $\rho_{yx}(B > 0) = \frac{\rho_{yx}(B)-\rho_{yx}(-B)}{2}$. Fig. 4.6(a) and (b) show the original data for the 25 nm sample, while the (anti-)symmetrized data are plotted as red dashed lines. The MR displays strong thickness-dependent behavior. In Fig. 4.7(a), we plot MR(%)=$\frac{\rho(B)-\rho(0)}{\rho(0)} \times 100\%$ for the eight samples at 300 mK and field applied along the c-axis. While the MR is always positive and unsaturating, we observe a clear and systematic suppression with reduced thickness. In the top panel of Fig. 4.7(b), we explicitly plot the thickness-dependent MR measured at 10 T. The value is ∼3000% in the 180-nm flake, which is comparable to that measured in the bulk crystal [60], and decreases by two orders of magnitude in the thinnest samples. Although the full Fermi surface of γ-MoTe$_2$ is complex and made up of multiple electron and hole pockets, the magnetotransport behavior may be understood from a simplified two-band model, where we assume that conduction takes place via one electron and one hole band only.

The suppression of MR we observe in thin samples then suggests either (1) an imbalance of electrons and holes or (2) a decrease in their carrier mobilities. In order to distinguish between these two scenarios, we have investigate the field-dependent exponent from our

45
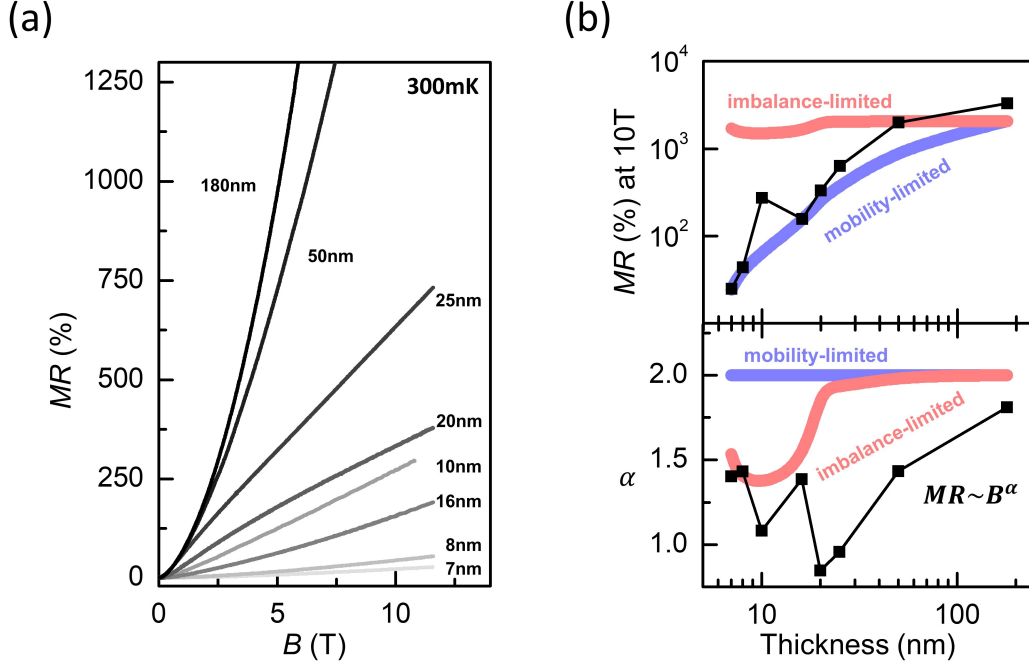
Figure 4.7: (a) Percent magnetoresistance as a function of perpendicular magnetic field. MR decreases with decreasing thickness. (b) The MR(%) measured at 10 T for the different samples shown in the top plot with the exponent α of power-law fit to the field dependence shown in the bottom.

data. We fitted a power-law formula, MR$\sim B^{\alpha}$, to the magnetoresistance data. The result is plotted in the bottom panel of Fig. 4.7(b). α is closer to 2 for thicker samples, but decreases with decreasing thickness, suggesting that the field-dependent term in the denominator of ρ_{xx} becomes more dominant, and thus $n = p$ for thinner flakes [scenario (1)]. The red and blue curves show the result of modeling the two scenarios separately, which will be discussed below. We would like to determine quantitatively the carrier concentrations and mobilities for the different thickness flakes. Unlike ρ_{yx}, however, ρ_{xx} is insensitive to the carrier type. We have therefore measured both longitudinal and transverse resistivities in order to determine the full resistivity tensor of our samples. The (anti-)symmetrized data are used to fit to the two-band model. In Fig. 4.8(a) and (b), the solid lines show the experimental data and the dashed lines show the result of simultaneous fitting to Eq. 4.10
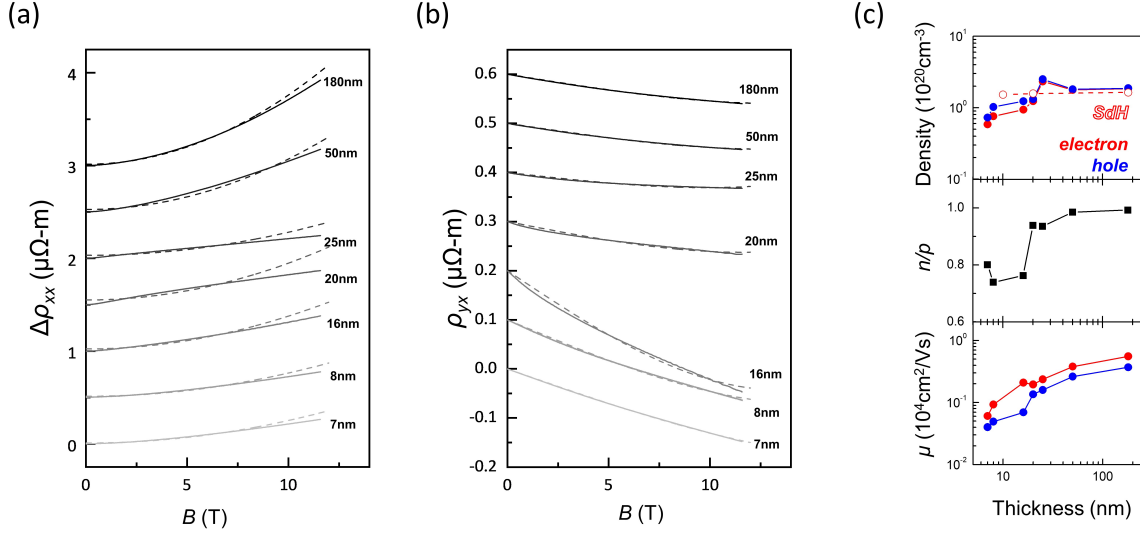
Figure 4.8: Simultaneous fit of (a) ρ_{xx} and (b) ρ_{yx} using the two-band model. (c) The carrier densities and mobilities for different thickness samples extracted from the fit are shown in the top and bottom plot, respectively. The electron-to-hole ratios for the different samples are shown in the center plot. The open circles in the top panel are carrier densities calculated from SdH measurements.

and Eq. 4.11. The extracted carrier densities, relative concentration ratio, and mobilities as a function of thickness are shown in Fig. 4.8(c). Within the two-band model, we find that the density and mobility for both electrons and holes decrease slightly with reduced thickness. The ratio between electrons and holes n/p also decreases, indicating greater carrier imbalance. For comparison, we have also plotted the electron densities determined by SdH oscillation measurements (open red circles), which will be discussed below.

In connection with the previous chapter, Chapter 3, we suggested hole band may have shifted to a lower energy level in thin samples due to the quantum confinement effect. We can further quantify how much it shifted based on our measured hole carrier density. According to the free electron model, the Fermi energy level, E_F, is related to the Fermi wavevector, k_F, by [119]

$$E_F = \frac{\hbar^2 k_F^2}{2m},\tag{4.21}$$

47

where $\hbar$ is the reduced Planck constant and m is rest mass of the electron. We assume the Fermi surface is spherical. Thus, the Fermi wavevector relates to the carrier density, n, by [119]

$$n = \frac{k_F^3}{3\pi^2}. \qquad (4.22)$$

Therefore, the Fermi energy level for certain carrier density is

$$E_F = \frac{\hbar^2}{2m}(3n\pi^2)^{2/3}. \qquad (4.23)$$

Based on our two-band model fit, the hole carrier concentration for the 180-nm sample and the 7-nm sample is 1.87×10^{20} and 0.73×10^{20} cm^{-3}, respectively. Using these two carrier concentrations, the edge of the hole band with respect to the Fermi energy level has shifted 56 meV. Based on the calculations by Kim et al., the hole band shifted about 20 meV when transitioning from the β phase to the γ phase [10]. So, based on this simple calculation, the hole band shifted enough in thin MoTe$_2$ to crystallize in the γ phase. Note that the calculation is a rough estimate as we are simplifying the Fermi surface as spherical. The decreased electron carrier density in thin samples is not consistent with the c-axis quantum confinement picture as the electron pockets are mostly cylindrical [14, 120]. It is consistent, however, with the transition energetics calculated by Kim et al. [10], which reports an overall shrinking of both surfaces accompanying the β-to-γ transition. The mechanism behind the thickness-driven effect, therefore, remains an open question.

Since both carrier imbalance and reduced mobility can suppress the MR, the two behaviors should be considered separately. In order to model this explicitly, we have taken the extracted carrier densities for the different thickness flakes and kept their mobilities constant and are fixed to the values for the 180-nm flake. We then calculated the MR within the two-band model using these new parameters, and plotted the MR percentage at 10 T as well as the field-dependent exponent on top of the original data in Fig. 4.7(b) in red ("imbalance-limited" curve). We similarly modeled the effect of reducing mobility only by fixing carrier densities fixed to the 180-nm values. This is plotted in blue ("mobility-limited" curve). We observe that while subquadratic field dependence can be attributed to the lack of charge compensation, the overall MR suppression is due to a reduction of carrier mobility. In principle, MR above 1000% may still be achieved in the thinnest samples, despite an imbalance ratio of $n/p \sim 0.8$, as long as the mobility can be made large.

We noticed that using the two-band model, the fit for ρ_{xx} is consistently larger than the measured values at higher fields beyond 8 T. The reason for this is that the degree of carrier imbalance, p-n, allowed for by ρ_{yx} is not sufficient to deviate ρ_{xx} strongly away from a B^2 dependence. Thus, we have additionally used a three-band model to fit the data. where we allow the charge of the third carrier to be a free parameter. Here, it is more straightforward to consider the conductivities:

$$\sigma_{xx}(B) = \frac{ne\mu_n}{1 + (\mu_n B)^2} + \frac{pe\mu_p}{1 + (\mu_p B)^2} + \frac{n_3 e\mu_3}{1 + (\mu_3 B)^2}, \tag{4.24}$$

$$\sigma_{xy}(B) = [-\frac{ne\mu_n}{1 + (\mu_n B)^2} + \frac{pe\mu_p}{1 + (\mu_p B)^2} \pm \frac{n_3 e\mu_3}{1 + (\mu_3 B)^2}]eB, \tag{4.25}$$

The charge for third species n_3 is left as a free parameter. The above formulas can be inverted to obtain the resistivities:

$$\rho_{xx} = \frac{\sigma_{xx}}{\sigma_{xx}^2 + \sigma_{xy}^2}, \tag{4.26}$$

$$\rho_{yx} = \frac{\sigma_{xy}}{\sigma_{xx}^2 + \sigma_{xy}^2}. \tag{4.27}$$

The results after simultaneous fitting of the experimental data to equations Eq. 4.26 and 4.27 are shown in Fig. 4.9.

While this indeed achieves a better fit, the third band has significantly lower mobility and fluctuates between electron and hole species. It is possible that it represents an effective average of the remaining bands, which acts to suppress further the MR at high fields. Nonetheless, we find that the behavior of the first two bands is qualitatively similar to that obtained in the two-band model, which suggests that this simplified picture may be sufficient to capture the physics.

4.2.2 SdH in thin MoTe$_2$

At high fields, SdH oscillations have been observed in high-quality MoTe$_2$ crystals, which allow for an independent measurement of the Fermi surface [14, 58, 80]. We observe quantum oscillations in $\rho_{xx}(B)$ or $\rho_{yx}(B)$ for the 10-, 20-, and 180-nm flakes at 300 mK. The
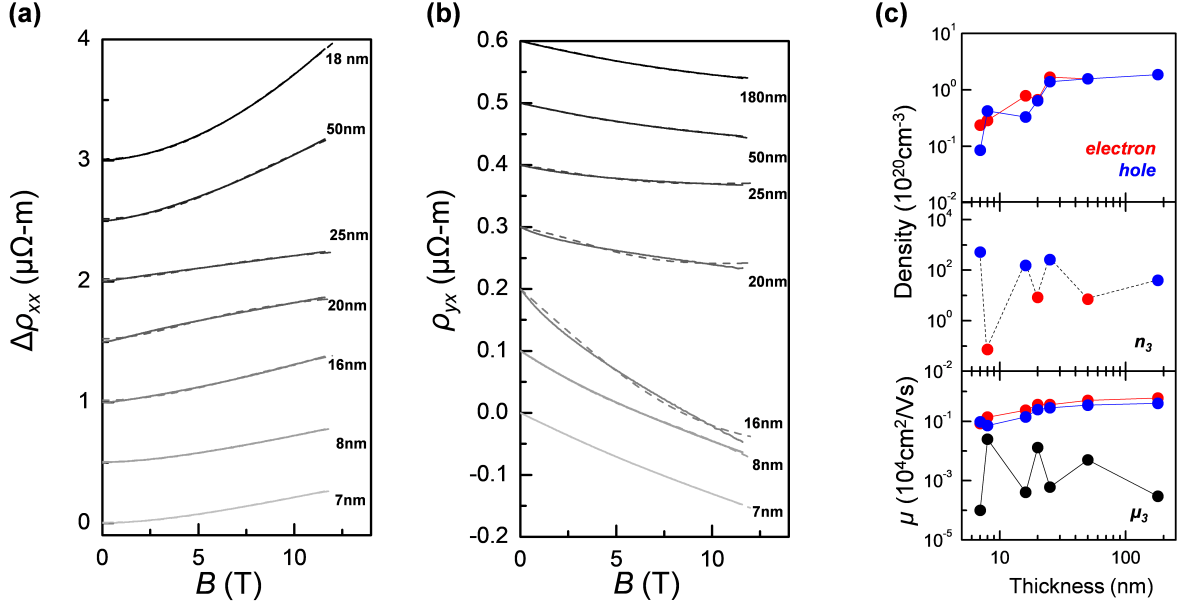
Figure 4.9: Symmetrized $\Delta\rho_{xx} = \rho_{xx}(B) - \rho_{xx}(0)$ in (a) and anti-symmetrized ρ_{yx} in (b) as a function of magnetic field for different sample thickness. Experimental data are shown as solid lines and three-band model fit are shown as dashed lines. Offset is applied to the traces for clarity. (c) Extracted carrier concentrations and mobility as a function of thickness.

upper panel of Fig. 4.10(a) shows representative data for the 20 nm sample, while the lower shows the result after subtracting a polynomial fit (dashed red line). Their background removed results are plotted as a function of $1/B$ in the insets of Fig. 4.10(b). The samples show a beating pattern, thus indicating the presence of more than one frequency. We have taken the FFT of the SdH oscillations and the result is shown in the main panel of Fig. 4.10(b). We observe two clear peaks for all samples and possibly three for the 20-nm flake, which show oscillations starting at lower fields. For the 180-nm flake, the peak positions (202 and 266 T) are similar to what has been observed in the bulk crystal [14], and correspond to carrier densities of 0.70×10^{20} and 0.93×10^{20} cm^{-3}, respectively, via the Onsager relation. Density functional calculations indicate these oscillation frequencies are associated with electron pockets [14], while the hole pocket frequencies either exceed
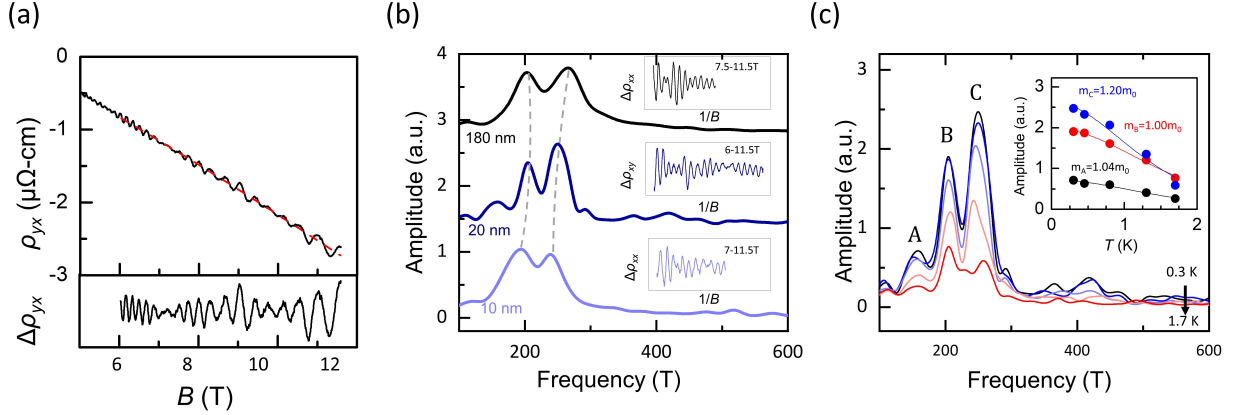
Figure 4.10: (a)(Top panel) Original $\rho_{yx}(B)$ data measured for the 20 nm sample. (Bottom) result after subtracting a polynomial fit (red dashed line). (b) Inset: SdH oscillations observed after subtracting the polynomial background for each sample. Their corresponding FFT is shown in the main panel. The dashed lines are guides to the eye showing decreasing frequencies with decreasing sample thickness. (c) Main panel: The FFT of the SdH oscillations for the 20-nm sample measured at 0.3, 0.45, 0.8, 1.3, and 1.7 K. Inset: The amplitude of the FFT peaks as a function of temperature fit to the LK formula to extract the effective masses.

1000 T or fall below 100 T. For the thinner flakes, these two peaks are systematically shifted to lower fields, and thus densities. In Fig. 4.8(c), we have plotted the sum of the densities extracted from the positions of the two prominent peaks (open red circles) in order to compare with the concentrations obtained from the two-band model. The thickness dependence is qualitatively consistent, although the electron density estimated from classical magnetotransport is lower in thinner samples. We have further performed the same measurement on the 20-nm flake, which shows the most prominent oscillations, as a function of temperature [see Fig. 4.10(c)]. By fitting the peak amplitudes to the LK formula (Eq. 4.19), we obtained an estimate of the effective masses ($\sim$1.0-1.2 m_0), which are slightly larger than those measured for the bulk crystal ($\sim$0.8 m_0) [14].

4.3 Conclusion

In summary, we used magnetotransport measurements to study the thickness evolution of the electronic structure in γ-MoTe$_2$ at low temperatures. We observe a decrease in both electron and hole densities as well as mobilities in thin flakes. The former possibly stabilizes the γ phase at room temperature, while the latter greatly suppresses the XMR effect. At the same time, this has potentially interesting consequences for the tailoring of XMR in future materials. Namely, it may be possible to still achieve very large MR values without near-perfect charge compensation.

Chapter 5

Non-linear electronic transport in WTe$_2$

5.1 Introduction

When a material is placed under a magnetic field, an electric field can be generated in the transverse direction with respect to the current direction. This is the well-known Hall effect, which was discovered in 1879 by Edwin Hall [121]. The effect can be easily explained using Lorentz force where the moving electrons are pushed to the transverse direction under a magnetic field. However, this simple model cannot explain the Hall effect in ferromagnetic material. Experimentally, the Hall effect is much strong in iron as compared to nonmagnetic conductors [122], hence given the name anomalous Hall effect (AHE). It took almost a century of theoretical and experimental investigations to properly explain the AHE [123]. The non-linear anomalous Hall effect (NLAHE) explored in this work relates closely to the AHE. Firstly, the driving mechanism are very similar, both have terms that are attributed to the Berry curvature. In contrast, however, the current and electric field in AHE are collinear in time-reversal invariant systems. This constraint does not apply to higher-order responses and Sodemann et al. have shown a second-order Hall voltage can arise in certain inversion-breaking materials while under timer-reversal condition [124]. Shortly after, NLAHE was observed in thin WTe$_2$ [15, 16], and subsequently in other

systems [17, 61, 125–129].

In this chapter, we present the exploration of NLAHE in thin WTe$_2$ with the focus on extending the frequency range. Firstly, we review recent works on NLAHE. We then examine the crystal symmetry of WTe$_2$ and the relation to the NLAHE. Following that, we show the experimental setup used and how it is designed to support high frequencies. Finally, we present our experimental data including successful rectification in the radio frequency (RF) range.

5.2   Non-linear anomalous Hall effect

NLAHE was first realized in thin WTe$_2$ [15, 16]. Soon after the realization of NLAHE in WTe$_2$, it has been realized in other systems [130]. For thin materials, this includes superconducting NbSe$_2$ [17], monolayer WSe$_2$ [131] and twisted WSe$_2$ [132], corrugated bilayer graphene [126] and the surface of topological insulator Bi$_2$Se$_3$ [129]. NLAHE was also observed in systems that are far from the monolayer limit. This includes Weyl semimetal TaIrTe$_4$ [127], nonmagnetic Weyl-Kondo semimetal Ce$_3$Bi$_4$Pd$_3$ [128], Dirac semimetal Cd$_3$As$_2$ [125] and semimetallic γ-MoTe$_2$ [61].

The driving mechanism of NLAHE can be categorized into intrinsic or extrinsic contribution. The intrinsic contribution depends only on the perfect crystal Hamiltonian. Sodemann et al. have shown a nonlinear Hall voltage can be driven by a finite Berry curvature in materials with time-reversal symmetry [124]. For a n-dimension system, the nonlinear Hall susceptibility tensor can be expressed as:

$$\chi_{abc} = -\epsilon_{adc}\frac{e^3\tau}{2\hbar^2(1+i\omega\tau)}\mathbf{D}_{bd}, \tag{5.1}$$

$$\mathbf{D}_{bd} = \int \frac{d^nk}{(2\pi)^n} f_0 \frac{\partial\Omega_d}{\partial k_b}, \tag{5.2}$$

where $\mathbf{D}_{db}$ is the Berry curvature dipole, Ω_d is the Berry curvature, f_0 is the equilibrium Fermi-Dirac distribution, τ is the relaxation time approximation in the Boltzmann equation, ϵ_{adc} is the third-rank Levi-Civita symbol and $\hbar$ is the reduced Planck constant. The

Berry curvature of a material can be tuned by applying a displacement field. Ma et al. have shown the NLAHE in bilayer WTe$_2$ varies with displacement field [15]. Hence, they attributed the major contribution is due to the Berry curvature.

The extrinsic contributions to the NLAHE are due to impurity scattering. Just like AHE, the two major mechanisms include skew scattering and side-jump [130]. Skew scattering is when electrons are scattered asymmetrically due to the effective spin-orbit coupling of the electron or the impurity [123]. The side-jump contribution is when electrons deflect in opposite directions by the opposite electric fields when approaching and leaving an impurity [123]. The different types of extrinsic contribution scale differently with the relaxation time, τ, in which the conductivity also depends on. It has been shown that the extrinsic contributions can be distinguished by analyzing the scaling of Hall conductivity with respect to the longitudinal conductivity (ie. $\sigma_H \sim \sigma_{xx}^\alpha$) [130]. For instance, it has been used to identify that the extrinsic contributions in MoTe$_2$ [61] and few-layered WTe$_2$ [16] are significant.

The NLAHE has direction dependency with respect to the crystallographic axis. Ma et al. did their measurements on bilayer WTe$_2$ with the sourcing current parallel to the crystal's a-axis. According to their data shown in Fig. 5.1(a), the observed second harmonic voltage in the transverse direction, $V_\perp^{2\omega}$, is significantly stronger compared to the longitudinal direction. Also, the quadratic growth of the Hall signal and the 2ω frequency establishes its second-order nature. Kang et al. did a more systematic investigation of the NLAHE's direction dependency. They probed thin WTe$_2$ with circularly placed electrodes as shown in the inset of Fig. 5.1(b). The WTe$_2$ flakes are chosen between four to eight layers. The result is shown in the main panel with 0° defined parallel to the crystallographic b-axis. Qualitatively, NLAHE is very small when the sourcing current is parallel to the b-axis. The direction dependency of NLAHE can be found in non-linear optics theory. For a linear medium, the electric dipole polarization, $\mathbf{P}$, is linearly related to the incident electric field, $\tilde{\mathbf{E}}$. In non-linear mediums, additional terms are added [133]:

$$\mathbf{P}_{nonlinear} = \epsilon_0[\chi^{(2)} \cdot \tilde{\mathbf{E}}^2 + \chi^{(3)} \cdot \tilde{\mathbf{E}}^3 + ... + \chi^{(n)} \cdot \tilde{\mathbf{E}}^n], \tag{5.3}$$

where ϵ_0 is the permittivity of free space and $\chi^{(n)}$ is the nth order susceptibility tensor. The higher order terms are usually very small, if not non-existence. Therefore, we will
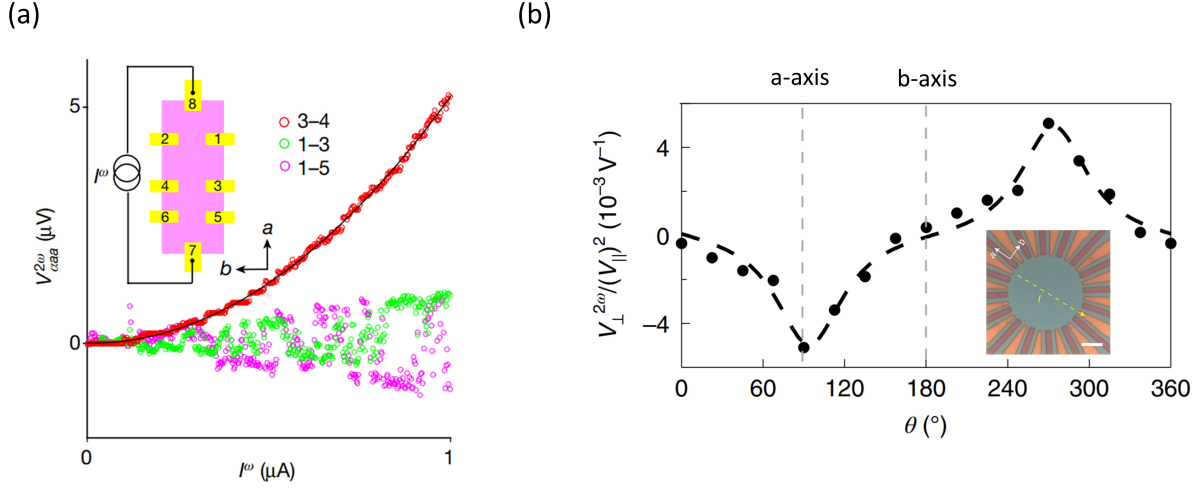
Figure 5.1: (a) Non-linear measurements of bilayer WTe$_2$ at T=50 K. The data shows both the longitudinal and transverse second harmonic signals with AC current sourcing in the crystal's a-axis direction. Figure adapted from [15] with permission from Springer Nature. (b) Non-linear Hall signal as a function of current sourcing angle, θ. Measurement taken on few layer WTe$_2$ at T=1.8 K. Inset shows the optical image of a representative device. Figure adapted from [16] with permission from Springer Nature.

focus only on the second order term, $\mathbf{P}^{(2)} = \epsilon_0 \chi^{(2)} \cdot \tilde{\mathbf{E}}^2$. Assume the incident electric field takes the form

$$\tilde{\mathbf{E}}(t) = \tilde{\mathbf{E}}_0 e^{i\omega t} + \tilde{\mathbf{E}}_0^* e^{-i\omega t}. \tag{5.4}$$

Then, it follows that the second order term is

$$\tilde{\mathbf{E}}^2(t) = \tilde{\mathbf{E}}_0^{\,2} e^{i2\omega t} + \tilde{\mathbf{E}}_0^{*\,2} e^{-i2\omega t} + 2\tilde{\mathbf{E}}_0 \cdot \tilde{\mathbf{E}}_0^*. \tag{5.5}$$

The second-order polarization depends on the incident electric field by

$$\mathbf{P}^{(2)} = \epsilon_0 \chi^{(2)} \cdot \tilde{\mathbf{E}}^2(t) = \epsilon_0 \chi^{(2)} \cdot [\tilde{\mathbf{E}}_0^{\,2} e^{i2\omega t} + \tilde{\mathbf{E}}_0^{*\,2} e^{-i2\omega t} + 2\tilde{\mathbf{E}}_0 \cdot \tilde{\mathbf{E}}_0^*]. \tag{5.6}$$

Notice the first two terms have double the frequency of the incident electric field, whereas the third term is DC.

$$\mathbf{P}^{(2)} = \mathbf{P}^{2\omega} + \mathbf{P}^{DC} = [\epsilon_0 \chi^{(2)} \cdot (\tilde{\mathbf{E}}_0^{\,2} e^{i2\omega t} + \tilde{\mathbf{E}}_0^{*\,2} e^{-i2\omega t})] + [2\epsilon_0 \chi^{(2)} \cdot \tilde{\mathbf{E}}_0 \cdot \tilde{\mathbf{E}}_0^*]. \tag{5.7}$$

Finally, we want to relate the polarization to current as that is what we will be measuring. The displacement field, $\mathbf{D}$, is defined as

$$\mathbf{D} = \epsilon_0 \tilde{\mathbf{E}} + \mathbf{P}. \tag{5.8}$$

The displacement current is the time derivative of the displacement field and is given by

$$\mathbf{j} = \epsilon_0 \frac{\partial \tilde{\mathbf{E}}}{\partial t} + \frac{\partial \mathbf{P}}{\partial t}. \tag{5.9}$$

If we measure in the DC current and the second harmonic current, the contribution only comes from $\mathbf{P}^{(2)}$ and are given by

$$\begin{cases} \mathbf{j}^{2\omega} \propto \chi^{(2)} \cdot (\tilde{\mathbf{E}}_0^{\,2} e^{i2\omega t} + \tilde{\mathbf{E}}_0^{*\,2} e^{-i2\omega t}) \\ \mathbf{j}^{DC} \propto \chi^{(2)} \cdot \tilde{\mathbf{E}}_0 \cdot \tilde{\mathbf{E}}_0^* \end{cases}, \tag{5.10}$$

where $\mathbf{j}^{2\omega}$ and $\mathbf{j}^{DC}$ are the currents double the incident electric field frequency and zero frequency, respectively. The magnitude of both currents depends quadratically on the amplitude of the incident electric field. The direction of the NLAHE signal with respect to a given incident electric field depends on non zeros terms in $\chi^{(2)}$.

The second-order non-linear susceptibility, $\chi^{(2)}$, in the above analysis depends on the crystal structure, specifically on certain symmetries [133]. Hence, it is necessary to examine the crystal structure of WTe$_2$ to determine the relation between sourcing electric field $\tilde{\mathbf{E}}$ and the signals $\mathbf{j}^{DC}$ and $\mathbf{j}^{2\omega}$. Raman spectroscopy has revealed that the crystal's space group of WTe$_2$ is thickness dependent. They are summarized in Table 5.1. Bulk WTe$_2$ belongs to the $Pmn2_1$ space group with a mirror plane normal to the a-axis (M_a) and a glide plane normal to the b-axis ($\bar{M}_b$). In few-layered WTe$_2$, only M_a symmetry exists. This puts few-layered WTe$_2$ in the Pm space group [134, 135]. The symmetries of few-layered WTe$_2$ are explained using representative bilayer schematics in Fig. 5.2(a). The resulting crystal structure after M_a, M_b and M_c transformations are shown in the second row. The third row is the overlap between the original and the transformed structures. For the M_a transformation, the crystal structures overlap perfectly, which means few-layered WTe$_2$ is symmetric about the mirror plane normal to the a-axis. For the other two transformations, the structures do not recover the original ones. The M_a symmetry is also apparent from

57

WTe$_2$ Thickness	group number	Hermann–Mauguin	Schoenflies	references
monolayer	11	$P2_1/m$	C_{2h}^2	[134, 135]
few layers	6	Pm	C_s^1	[134, 135]
bulk	31	$Pmn2_1$	C_{2v}^7	[72, 134, 135]

Table 5.1: Space group of WTe$_2$ in different thickness range.

the top view of a single layer as shown in Fig. 5.2(b). Monolayer WTe$_2$ is centrosymmetric and belongs to the $P2_1/m$ space group.

In this work, we focus on few layers WTe$_2$. The $\chi^{(2)}$ of the Pm space group is given by [133]:

$$\chi_{Pm}^{(2)} = 2 \begin{pmatrix} d_{11} & d_{12} & d_{13} & 0 & d_{15} & 0 \\ 0 & 0 & 0 & d_{24} & 0 & d_{26} \\ d_{31} & d_{32} & d_{33} & 0 & d_{35} & 0 \end{pmatrix}, \tag{5.11}$$

where the x-direction is set to be parallel to crystallographic b-axis (the mirror axis in few layer WTe$_2$). For a thin flake geometry, it is more convenient to source the electric field in the ab-plane, ie. $\mathbf{E} = \{E_b, E_a, 0\}$. Therefore, the expected in-plane second harmonic current would be

$$j_a^{2\omega} \propto 2d_{26}E_b E_a \tag{5.12}$$

$$j_b^{2\omega} \propto d_{11}E_b^2 + d_{12}E_a^2. \tag{5.13}$$

Qualitatively, this shows there should be a finite second harmonic hall current in the b-axis direction when sourcing electric field along the a-axis. This is the setup used in this experiment, as indicated by the arrow in Fig. 5.2(b). A more quantitative description was given by Kang et al. where the second harmonic Hall voltage ($V_\perp^{2\omega}$) is related to the sourcing voltage angle (θ) by [16]

$$\frac{V_\perp^{2\omega}}{V_\parallel^2} \propto sin\theta \frac{d_{12}r^2 sin^2\theta + (d_{11} - 2d_{26}r^2)cos^2\theta}{(cos^2\theta + rsin^2\theta)^2}, \tag{5.14}$$

where $r = \frac{\rho_a}{\rho_b}$ is the ratio of resistivity of the a-axis to b-axis, θ is the incident electric field angle with $0°$ defined parallel to the b-axis and $V_\parallel$ is the first harmonic voltage parallel
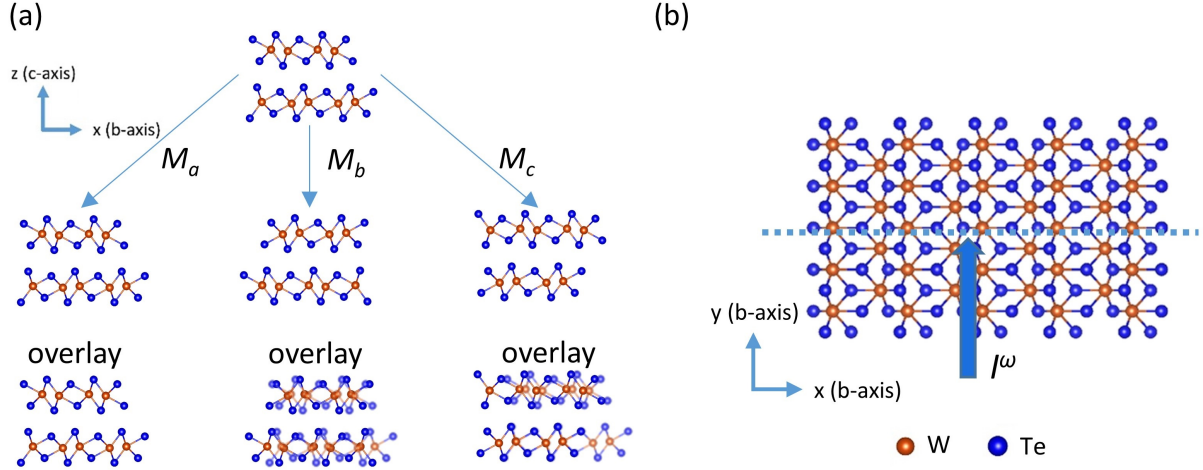
Figure 5.2: Crystal symmetry of few-layered WTe$_2$. The x-direction in the non-linear susceptibility tensor is taken to be parallel to the mirror plane. (a) Side view of WTe$_2$ in the first row. The second row shows the structure after each transformations. The third row is the overlap of the before (transparent) and after (solid) transformations. (b) Top view showing the mirror plane (dashed line) normal to the a-axis. Only one layer is shown for clarity. The arrow indicates the direction of the sourcing electric field that gives the strongest NLAHE signal.

to the sourcing direction. This is also the formula used for the fitting curve shown in Fig. 5.1(b). Since the crystal structure of low temperature MoTe$_2$ is the same as WTe$_2$, in-plane NLAHE in also be observed in the former [61, 136]. We picked WTe$_2$ because it is relatively easier to exfoliate and have much better chance of finding flakes that are thin enough.

5.2.1 High frequency rectification

As discussed earlier, the NLAHE has both the second harmonic term and the DC term. Due to the latter term, systems that display NLAHE are able to convert an oscillating electromagnetic field into DC voltage. Theoretically, NLAHE is predicted to persist to the terahertz range [137, 138]. Therefore, this process can be used as a high-frequency rectifier,

which plays a key role in wireless communication, energy harvesting and infrared detection [137, 139, 140].

Most of the previous experiments on NLAHE are performed by measuring the second harmonic signal in the low-frequency range. For WTe_2, the highest frequency tested was ~1 kHz [15]. Frequencies higher than that have been demonstrated in other materials. In particular, using the setup shown in Fig. 5.3(a), Zhang et al. showed the DC component of the NLAHE in $NbSe_2$ can be detected with sourcing frequencies up to 900 MHz [17]. Similarly, Kumar et al. were able to detect rectification in $TaIrTe_4$. The excitation field comes from a 2.4 GHz patch antenna. This particular frequency is chosen because it is widely used in WiFi technology. By placing the $TaIrTe_4$ flake in close proximity to the antenna, a DC voltage that is attributed to the NLAHE was detected [127]. Quantitatively,
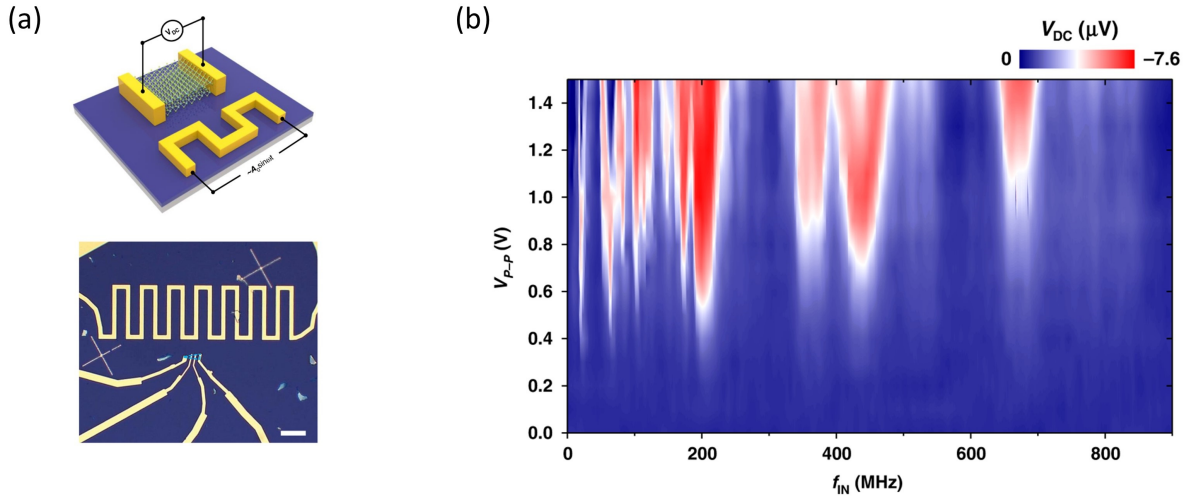
Figure 5.3: (a) Schematics and Optical image of antenna setup for rectification in $NbSe_2$. (b) The 2D plot of V_{DC} detected in $NbSe_2$ as a function of antenna's driving voltage and frequency shown in the bottom. Figure adapted from [17], reused under Creative Commons license CC BY 4.0.

the observed DC voltage of $NbSe_2$ as a function of the antenna's driving voltage and frequency is shown in Fig. 5.3(b). According to the 2D plot, the rectification is not uniform in the frequency range tested. This suggests the NLAHE in $NbSe_2$ is frequency dependent.

However, considering that the RF electric field was sourced by using an antenna, the electric field it emits may be frequency dependent. Therefore, the electric field received by the sample may be non-uniform. In order to investigate the frequency dependency of NLAHE, the source itself should be uniform across all frequencies. Therefore, rather than using an antenna, we used a planar waveguide geometry to deliver the high-frequency electric field. In the next section, we present in detail the design of our setup.

5.3   Experimental setup

In this experiment, we attempt to increase the frequency of the sourcing frequency. For the electrodes, we employed a signal-ground-signal geometry to deliver the excitation current. This setup is commonly used in spin-torque ferromagnetic resonance measurements. Previous reports have shown this geometry is able to deliver current with frequencies up to ~10 GHz [141–145]. We have, however, made some modifications to it. Since we want to measure voltage in the transverse direction, we added additional Hall electrodes. An optical image of the design is shown in Fig. 5.4(a). For the substrate, we chose sapphire because it is good for high frequency operations [141].
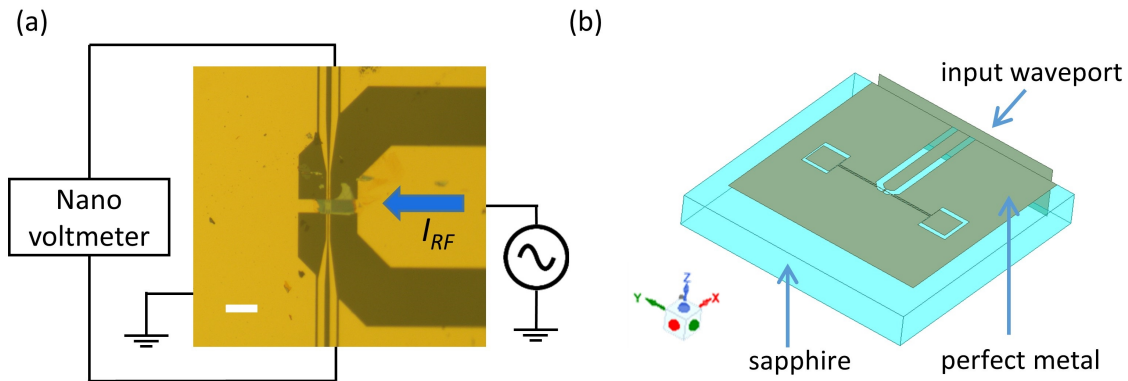
Figure 5.4: (a) Optical image of the setup used for RF compatible measurements. Scale bar is 50 μm. (b) Model used for the HFSS simulation.

The added additional Hall bars to the signal-ground-signal geometry create distortion

at high frequencies. We first used computer simulation to characterize the disturbance caused by these extra electrodes. The program used is a high-frequency structure simulator (HFSS) by Ansys, Inc. The 3D model was constructed with real dimensions of the electrode used as shown in Fig. 5.4(b). The most relevant properties of the model are their conductivity and permittivity. For vacuum and sapphire (the substrate material), they are set to the values in the database. For WTe_2, many of its high-frequency properties are not known. Since WTe_2 is a semimetal, it should have optical properties similar to other semimetals. Thus, as an approximation, the WTe_2 was set to have the properties of graphite. The gold electrodes are not modeled as 3D objects. Rather, they are set as 2D surfaces with "perfect E" boundary conditions. The excitation of the system is done by setting a 2D surface called the waveport. The plane defines where the energy enters the system. The resulting electric field lines distribution for different frequencies are shown in Fig. 5.5. The 500 Hz simulation provides a reference DC limit case. As expected, the electric field lines are mostly uniform in the region between the source and drain. Up to 1 GHz, the simulation does not show much difference. For the 5 GHz and 8 GHz simulations, the electric fields are not as uniform. Therefore, based on the simulation, it is likely that the system will experience loss for frequencies beyond 1 GHz.
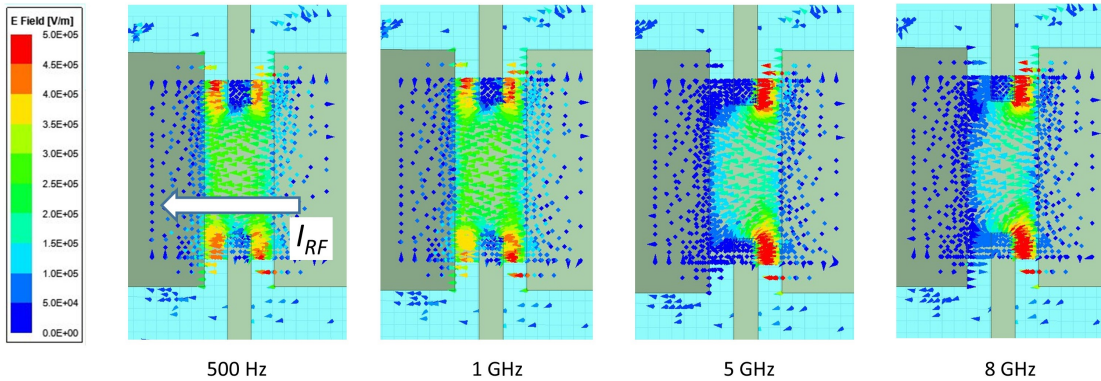
Figure 5.5: Simulation result showing the electric field distributions of different sourcing frequencies.

To deliver the current to the chip, we designed a coplanar waveguide (CPW) that supports high frequencies. The CPW is made from a double-sided 1/2 oz copper FR-
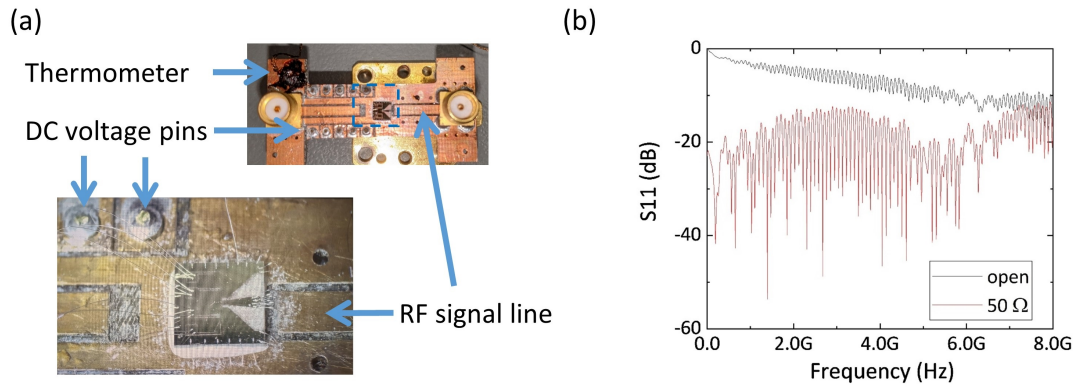
Figure 5.6: (a) Picture of the actual setup of RF measurements. Top: The PCB made CPW used to carry the RF signal on to the sapphire chip. Bottom: Up close image showing the sapphire chip that is mounted on the PCB board. (b) The S_{11} of the setup used with 50 Ω impedance matched case and the open circuit case.

4 substrate. The RF line in the center has a width of 1.8 mm with the gap between the signal and ground being 0.35 mm. These dimensions are chosen so that it is 50 Ω impedance matched, the characteristic impedance of our equipment. The sapphire chip is glued onto the PCB board using silver paste. Electric connections from the PCB to the electrodes on the substrate were made with wire bonds. Pictures of the actual setup are shown in Fig. 5.6(a).

After making both the CPW and the sapphire chip, we tested the total loss in the combined system. This is done by using a vector network analyzer (VNA) made by Advantest model r3767cg. The system is connected to the VNA for the reflection signal test. The VNA sources an oscillating voltage and measures how much of it is reflected back to the source port. The ratio of the reflection to forward voltage ratio is known as S_{11} measurement. By placing either a dummy 50 Ω resistor or no resistor at the sample location, it represents the impedance-matched case and the infinite impedance case, respectively. In the impedance-matched scenario, there should be no reflection as all the power would be absorbed by the load resistor. In contrast, all power should be reflected in the infinite impedance case, just like how a wave would reflect back when hitting a wall. The measured S_{11} for both cases are shown in Fig. 5.6(b). In the 50 Ω case, there is minimum reflection

63

across all frequencies as expected. In the infinite impedance case, however, the reflection is close to unity at low frequencies and starts to decrease as the frequency increases. Approximately, the voltage reflection is less than -3 dB (50% power) beyond 1 GHz. Therefore, this shows the setup is not ideal at frequencies higher than that.
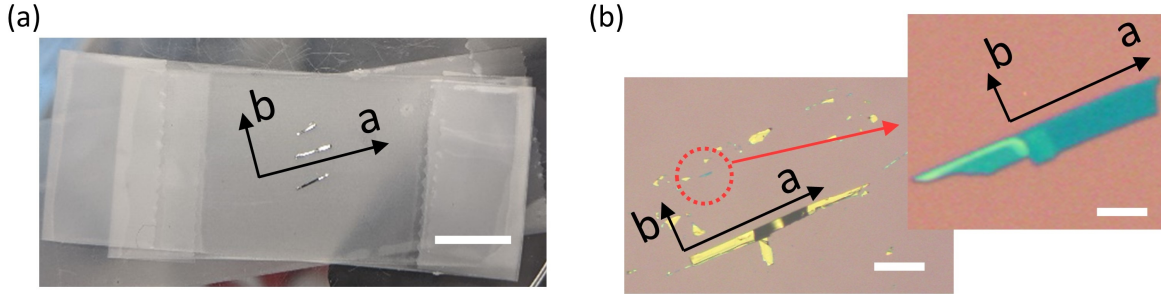
Figure 5.7: Optical images of WTe$_2$ during the exfoliation process. (a) The WTe$_2$ crystals are placed parallel to each other on the Scotch tape. The longer crystal direction is the a-axis. The scale bar is 5 mm. (b) The resulting WTe$_2$ flakes that are exfoliated on Si/SiO$_2$ chip. The overview image (scale bar 200 μm) shows a large flake that has a well defined axis direction. The targeted flake in the zoomed in image (scale bar 10 μm) with its axis direction labeled.

As mentioned, the sourcing electric field should align with the crystallographic a-axis in order to observe a strong NLAHE signal in the transverse direction. WTe$_2$ crystallizes in a needle shape where the longer direction is parallel to the a-axis [59]. This property serves as a convenience in determining the crystal axis of thin flakes of WTe$_2$. During the exfoliation process, the bulk crystals are first placed parallel to each other on the Scotch tape as shown in Fig. 5.7(a). The longer direction is the a-axis as labeled in the figure. The resulting flakes that are exfoliated on the Si/SiO$_2$ substrate are shown in Fig. 5.7(b). Thin flakes tend to cleave along the crystal axes, especially the bigger ones. Thus, it can be used as a compass for the smaller, targeting flakes. If necessary, the crystallographic directions can be verified later using techniques such as second harmonic generation [61].

The oscillating currents with frequencies below 500 kHz were sourced by a lock-in amplifier (Stanford Research Systems model SR860). For higher frequencies, we used the VNA, which ranges from 300 kHz to 8 GHz. For an alternating current, $I(\omega)$, its second

harmonic current would be [15, 17, 146]

$$I^2(\omega) = [I_0 sin(\omega t)]^2 = I_0^2[1 + sin(2\omega t - \pi/2)]/2. \tag{5.15}$$

Measuring the second harmonic voltage is done by standard lock-in technique using the two input ports provided by the lock-in amplifier. The above equation shows there should be a $\pi/2$ phase shift between the source and generated voltage. Therefore, it is expected that the lock-in measurement for the second harmonic signal would show a $90°$ phase shift with respect to the source. The DC voltage is measured by a nanovoltmeter (Keithley model 2182A). Note that the lock-in amplifier sources and measures in root mean square (rms) whereas the nanovoltmeter measures peak voltage. The two voltages are related by $V_{peak} = \sqrt{2}V_{rms}$.

5.4   Experimental results
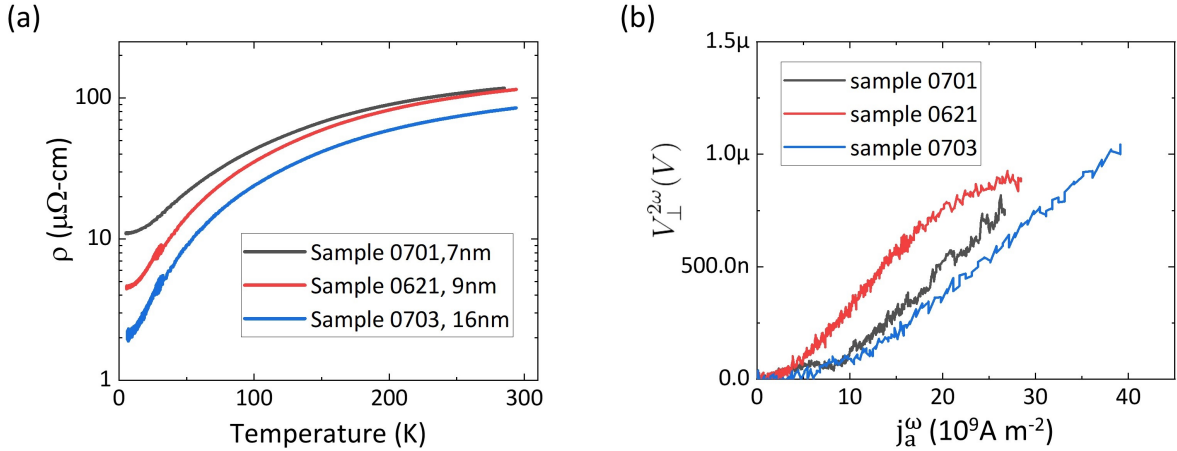
Figure 5.8: (a) Resistivity dependence as a function of temperature for the three WTe_2 devices. (b) The second harmonic Hall voltage measured with current injecting in the a-axis direction with frequency ω=17.77 Hz.

Three devices with thicknesses between 7 to 16 nm were made. The temperature-dependent resistivities of the three samples are shown in Fig. 5.8(a). All three devices

show metallic behavior with residual resistivities between 2 to 10 $\mu\Omega$-cm. These values are between the previously reported values of bulk (2 $\mu\Omega$-cm [59]) and thin WTe$_2$ (50 to 150 $\mu\Omega$-cm [16, 55]). Fig. 5.8(b) shows the NLAHE signal taken at T=6 K. The frequency of the sourcing current was set to $\omega = 17.77$ Hz. All three devices show non-linear behavior at low bias current as expected. At high biasing current, however, it plateaus. This is likely caused by Joule heating and the temperature of the samples increased. As previous reports of NLAHE's temperature dependence have shown, the $V_\perp^{2\omega}$ decreases with raising temperature [15, 16]. We have also tested for a few temperatures. This will be discussed later with further details. Therefore, the sub-quadratic behavior at high currents is presumably due to this heating effect.

Next, we attempt to increase the frequency. Fig. 5.9(a) shows the frequency dependence of $V_\perp^{2\omega}$ for Sample 0703 measured at 6 K. The bias current is held constant at I_{rms}=2.4 mA. Up to 2ω=500 kHz, the maximum frequency of our SRS 860 lock-in amplifier, no apparent cutoff frequency is detected. We also made a few current sweeps at different frequencies, ω=45, 150 and 250 kHz, as shown in Fig. 5.9(b). Similar to the frequency sweep, $V_\perp^{2\omega}$ also shows no dependency on the frequency.

(a) (b)
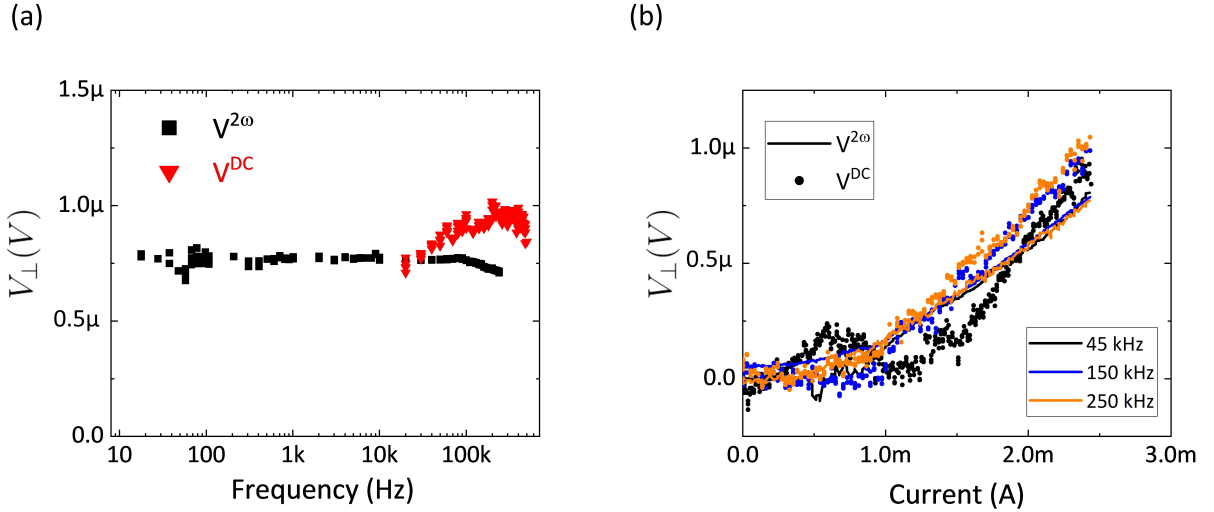
Figure 5.9: (a) Frequency dependent Hall measurement. (b) $V_\perp^{DC}$ and $V_\perp^{2\omega}$ Hall measurements at different frequencies.

The lock-in amplifier produces low-frequency noise while sourcing the I^ω. That noise interferes with the $V_\perp^{DC}$ signal. Therefore, a high-pass filter with a cutoff frequency of 10 kHz was added to the current source to block out that low-frequency noise. Unfortunately, this resulted in losing the ability to measure $V_\perp^{DC}$ for $\omega <$ 10 kHz. By holding a constant current (I_{rms}=2.4 mA), the $V_\perp^{DC}$ for frequencies 10 kHz$< \omega <$500 kHz are plotted against $V_\perp^{2\omega}$ in Fig. 5.9(a). A few current sweeps by holding the frequency constant, comparison of $V_\perp^{2\omega}$ and $V_\perp^{DC}$ is shown in Fig. 5.9(b). They show great agreement over the frequency range that is available by the lock-in amplifier. This is consistent with the theory, that the DC and second harmonic terms of NLAHE have the same magnitude. We also measured the temperature dependence of both $V_\perp^{2\omega}$ and $V_\perp^{DC}$. This is shown in Fig. 5.10. The frequency of the current was set to ω=45 kHz. Again, both voltages show comparable magnitude and decreases with increasing temperature.
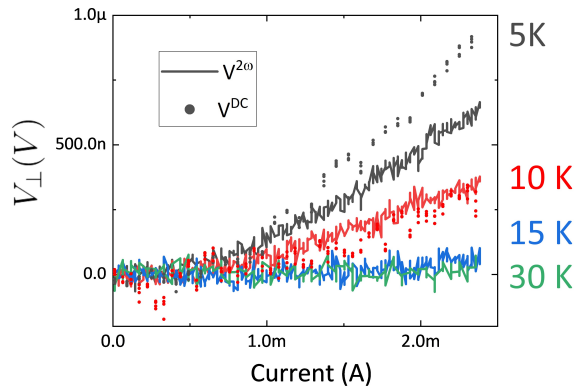
Figure 5.10: Temperature dependency of the NLAHE.

5.4.1 RF rectification

The VNA is used to source currents with higher frequencies. Since the VNA and lock-in amplifier are both capable of sourcing frequencies between 300 kHz and 500kHz, we are able to compare the $V_\perp^{DC}$ signal generated by the two different sources. Fig. 5.11(a) shows the comparison with ω=500 kHz at 5 K. The current delivered by the VNA was calibrated

based on the following calculation [143]. To begin with, for an oscillatory sine wave, the total current at any point is the sum of the forward traveling wave and the reflection wave. That is

$$I(z) = \frac{1}{Z_c}(Ae^{-ikz} - Be^{ikz}), \tag{5.16}$$

where $A = V_0$ is the amplitude of the forward traveling voltage supplied by the source, B is the amplitude of the reflection voltage and Z_C is the characteristic impedance and is 50 Ω in our setup. The reflection coefficient is defined as $\Gamma = B/A$. This is the measurable quantity S_{11}. and substituting in the above relation gives

$$I_{RF}(z) = \frac{V_0}{Z_c}(e^{-ikz} - \Gamma e^{ikz}). \tag{5.17}$$

For convenience, we can set the location of the test device at $z = 0$, and the current through the device is give by

$$I_{RF}(0) = \frac{V_0}{Z_c}(1 - \Gamma). \tag{5.18}$$

Since VNA source levels are set in power, not voltage. So converting to power via $P_0 = V_0^2/Z_C$, we have

$$I_{RF} = \sqrt{P_0(1 - \Gamma)^2/Z_C}. \tag{5.19}$$

The P_0 is the power sourced by the VNA. Between the VNA and the sample, there will be loss through the transmission line. Thus, we characterized this loss by measuring the transmission ratio, S_{21}. Adding this correction term, the final RMS current going through the sample is

$$I_{RF} = \sqrt{P_0 S_{21}^2(1 - \Gamma)^2/Z_C}. \tag{5.20}$$

Using the above conversion, we can estimate the current delivered to the sample by the VNA.

Fig. 5.11(b) shows the measured $V_\perp^{DC}$ as a function of both VNA power and frequency. The $V_\perp^{DC}$ grows as the power is increased. However, the signal is not uniform throughout the whole frequency range. Few peaks are observed around frequencies of 4 MHz, 400 MHz and 1 GHz. This is most apparent in the highest power curve, -5 dBm. Also, beyond 500 MHz, the signal $V_\perp^{DC}$ sees a downward trend. We know the setup is not perfect and the source RF signal will experience loss, especially at high frequencies. Therefore, we quantify
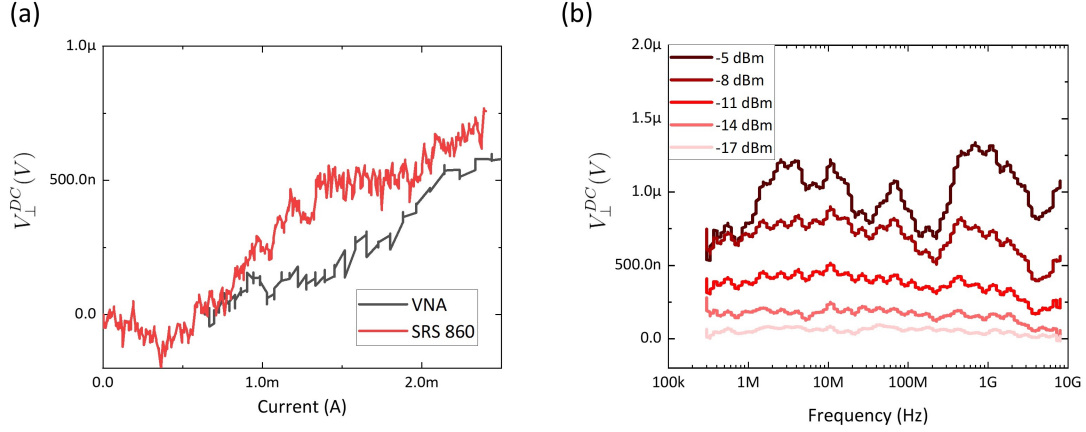
Figure 5.11: (a) Comparison of $V_\perp^{DC}$ measured by two different current source. (b) The $V_\perp^{DC}$ as a function of VNA output frequency for different powers.

the current delivered to the device by measuring how much the sample heated up due to Joules heating. Since the resistivity of WTe$_2$ depends on temperature, the effective Joule heating can be quantified by monitoring the resistance of WTe$_2$ as a function of VNA power and frequency. A schematic of the setup is shown in Fig. 5.12(a). A bias tee was used to combine the high-frequency current and low-frequency currents, ω=17.77 Hz sourced by the lock-in amplifier. Fig. 5.12(b) is the resistance of Sample 0703 as a function of temperature, which serves as the reference. Fig. 5.12(c) shows the WTe$_2$'s resistance dependence on VNA power and frequency. when the power increase, the resistance also goes up. This is consistent with increasing temperature in WTe$_2$. As the frequency increases, less heating is observed. This is likely due to the dielectric loss in the system, which is expected to be higher with increasing frequencies. This will result in less power delivered to the device. Comparing the heating 2D plot to the peaks observed in the $V_\perp^{DC}$ measurements in Fig. 5.11(b), there are no heating hot spots at the frequencies where the peaks are observed. Therefore, we rule out the effect due to inconsistent sourcing current. More investigation is needed to explain the stronger signals around those frequencies.
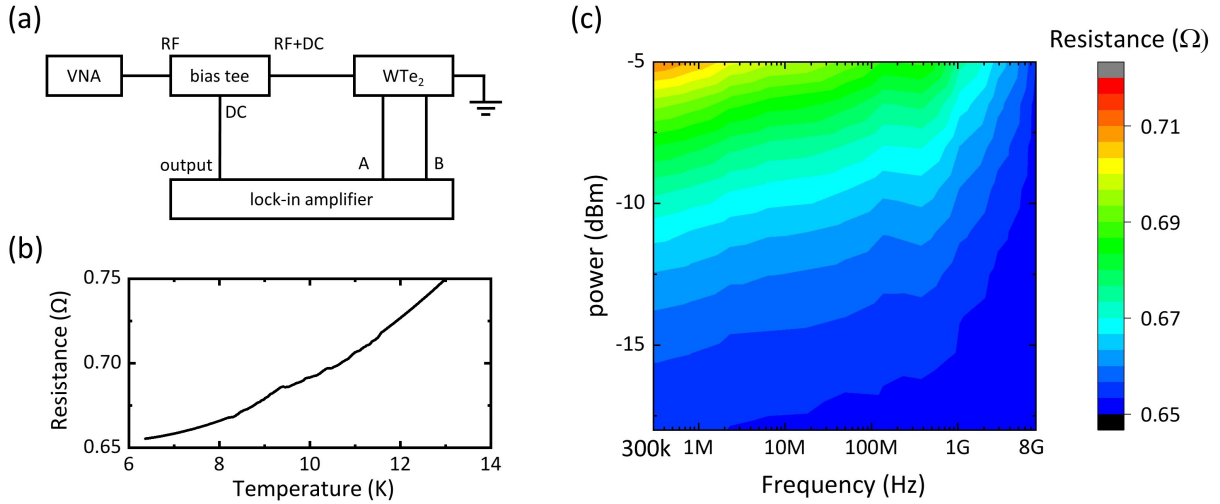
Figure 5.12: Characterizing Joule heating due to RF current. (a) The setup of the measurement. (b) The measured temperature dependent resistance of Sample 0703. (c) 2D plot of the resistance of WTe$_2$ as a function of VNA power and frequency. The measurement was performed on Sample 0703 at 6 K.

5.5 Conclusion

In summary, this experiment extended the range for the previously reported NLAHE in few-layered WTe$_2$. RF electric fields up to 8 GHz, which covers radio telecommunication and WiFi frequency range, were rectified into DC signals. As this is a proof-of-concept experiment, there is room for improvement. Specifically, the measured DC response is not uniform across all frequencies. More tests on different samples would help in determining the cause for the stronger signal at some frequencies. Also, since theories predict that the NLAHE should persist to higher frequencies, we can improve the setup to investigate the intrinsic frequency limit of the NLAHE in WTe$_2$.

Chapter 6

Conclusion

This thesis presents the study of MoTe$_2$ and WTe$_2$, both are members of the TMDC family. Semimetallic MoTe$_2$ naturally crystallizes in two structures, β and γ phase. It is able to transition between the two according to temperature. In our work, we demonstrated that thickness can also drive the phase transition. In thinner samples, the hysteresis in the resistivity-temperature plot that is associated with the first-order phase transition vanishes. We then characterized the crystal structure of thin MoTe$_2$ using Raman spectroscopy. In the tested temperature range, 150-400 K, only the symmetry-breaking phase exists for thickness below $\sim$12 nm. Theoretical calculations of bulk MoTe$_2$ have shown the hole band is lowered as it transitions from β to γ phase. In thin samples, we believe a similar lowering of the hole band due to the quantum confinement effect is the cause for establishing the γ phase in thin MoTe$_2$.

We then characterized the transport properties of MoTe$_2$ as thickness is reduced. Using the two-band model, we find that the carrier densities of both electron and hole carriers decreased for thinner samples. This is consistent with theoretical calculations where the electron and hole bands are smaller in the γ phase as compared to the β phase. However, since the electron bands are mostly cylindrical, quantum confinement effect should have little impact on its carrier density. Hence quantum confinement should not be the main reason for establishing the γ phase in thin MoTe$_2$. The hole band, however, in thin MoTe$_2$ is comparable to the energy level in γ-MoTe$_2$. This is a plausible explanation for thin

MoTe$_2$ crystallizing only in the γ phase. The MR, which is extremely large in bulk MoTe$_2$, decreased by two orders of magnitude in the 7 nm sample when compared to the 180 nm sample. For all samples tested, the ratio between the two carrier densities is still close to unity. Therefore, the decrease in MR is not the loss of compensation between the carrier species. Instead, the two-band model analysis shows the mobility of the two carriers decreased significantly, which is the reason for reduced MR in thin MoTe$_2$.

In the third experiment, we explored the frequency dependency of the NLAHE in thin WTe$_2$. By using an RF-compatible design, we showed the second harmonic Hall voltage is independent of frequency up to 250 kHz. The DC component of the NLAHE is also measured for frequencies from 10 kHz to 8 GHz. DC voltage is detected at all frequencies, however, the signal shows some frequency dependency. The findings are still preliminary, thus, further investigations are needed to address this observation.

References

[1] K. Zhang, C. Bao, Q. Gu, X. Ren, H. Zhang, K. Deng, Y. Wu, Y. Li, J. Feng, and S. Zhou, Nature Communications **7**, 13552 (2016).

[2] Y. Zhang, Y.-W. Tan, H. L. Stormer, and P. Kim, Nature **438**, 201 (2005).

[3] K. S. Novoselov, Z. Jiang, Y. Zhang, S. V. Morozov, H. L. Stormer, U. Zeitler, J. C. Maan, G. S. Boebinger, P. Kim, and A. K. Geim, Science **315**, 1379 (2007).

[4] D. A. Rhodes, A. Jindal, N. F. Q. Yuan, Y. Jung, A. Antony, H. Wang, B. Kim, Y.-c. Chiu, T. Taniguchi, K. Watanabe, K. Barmak, L. Balicas, C. R. Dean, X. Qian, L. Fu, A. N. Pasupathy, and J. Hone, Nano Letters **21**, 2505 (2021), pMID: 33689385, https://doi.org/10.1021/acs.nanolett.0c04935 .

[5] A. Chaves, J. G. Azadani, H. Alsalman, D. R. da Costa, R. Frisenda, A. J. Chaves, S. H. Song, Y. D. Kim, D. He, J. Zhou, A. Castellanos-Gomez, F. M. Peeters, Z. Liu, C. L. Hinkle, S.-H. Oh, P. D. Ye, S. J. Koester, Y. H. Lee, P. Avouris, X. Wang, and T. Low, npj 2D Materials and Applications **4**, 29 (2020).

[6] Y. Cao, V. Fatemi, S. Fang, K. Watanabe, T. Taniguchi, E. Kaxiras, and P. Jarillo-Herrero, Nature **556**, 43 (2018).

[7] S. Manzeli, D. Ovchinnikov, D. Pasquier, O. V. Yazyev, and A. Kis, Nature Reviews Materials **2**, 17033 (2017).

[8] M. Vellinga, R. de Jonge, and C. Haas, Journal of Solid State Chemistry **2**, 299 (1970).

[9] H. P. Hughes and R. H. Friend, Journal of Physics C: Solid State Physics **11**, L103 (1978).

[10] H.-J. Kim, S.-H. Kang, I. Hamada, and Y.-W. Son, Phys. Rev. B **95**, 180101 (2017).

[11] Y. Cheon, S. Y. Lim, K. Kim, and H. Cheong, ACS Nano **15**, 2962 (2021), pMID: 33480685, https://doi.org/10.1021/acsnano.0c09162 .

[12] J. L. Hart, L. Bhatt, Y. Zhu, M.-G. Han, E. Bianco, S. Li, D. J. Hynek, J. A. Schneeloch, Y. Tao, D. Louca, P. Guo, Y. Zhu, F. Jornada, E. J. Reed, L. F. Kourkoutis, and J. J. Cha, Emergence of layer stacking disorder in c-axis confined MoTe$_2$ (2022), arXiv:2210.16390.

[13] Q. Zhou, D. Rhodes, Q. R. Zhang, S. Tang, R. Schönemann, and L. Balicas, Phys. Rev. B **94**, 121101 (2016).

[14] D. Rhodes, R. Schönemann, N. Aryal, Q. Zhou, Q. R. Zhang, E. Kampert, Y.-C. Chiu, Y. Lai, Y. Shimura, G. T. McCandless, J. Y. Chan, D. W. Paley, J. Lee, A. D. Finke, J. P. C. Ruff, S. Das, E. Manousakis, and L. Balicas, Phys. Rev. B **96**, 165134 (2017).

[15] Q. Ma, S.-Y. Xu, H. Shen, D. MacNeill, V. Fatemi, T.-R. Chang, A. M. Mier Valdivia, S. Wu, Z. Du, C.-H. Hsu, S. Fang, Q. D. Gibson, K. Watanabe, T. Taniguchi, R. J. Cava, E. Kaxiras, H.-Z. Lu, H. Lin, L. Fu, N. Gedik, and P. Jarillo-Herrero, Nature **565**, 337 (2019).

[16] K. Kang, T. Li, E. Sohn, J. Shan, and K. F. Mak, Nature Materials **18**, 324 (2019).

[17] E. Zhang, X. Xu, Y.-C. Zou, L. Ai, X. Dong, C. Huang, P. Leng, S. Liu, Y. Zhang, Z. Jia, X. Peng, M. Zhao, Y. Yang, Z. Li, H. Guo, S. J. Haigh, N. Nagaosa, J. Shen, and F. Xiu, Nature Communications **11**, 5634 (2020).

[18] N. D. Mermin, Phys. Rev. **176**, 250 (1968).

[19] K. v. Klitzing, G. Dorda, and M. Pepper, Phys. Rev. Lett. **45**, 494 (1980).

[20] K. S. Novoselov, A. K. Geim, S. V. Morozov, D. Jiang, Y. Zhang, S. V. Dubonos, I. V. Grigorieva, and A. A. Firsov, Science **306**, 666 (2004), https://www.science.org/doi/pdf/10.1126/science.1102896 .

[21] A. K. Geim and K. S. Novoselov, Nature Materials **6**, 183 (2007).

[22] J. Baringhaus, M. Ruan, F. Edler, A. Tejeda, M. Sicot, A. Taleb-Ibrahimi, A.-P. Li, Z. Jiang, E. H. Conrad, C. Berger, C. Tegenkamp, and W. A. de Heer, Nature **506**, 349 (2014).

[23] C. Lee, X. Wei, J. W. Kysar, and J. Hone, Science **321**, 385 (2008), https://www.science.org/doi/pdf/10.1126/science.1157996 .

[24] J. Simonin, Phys. Rev. B **33**, 7830 (1986).

[25] J. P. Carbotte, Rev. Mod. Phys. **62**, 1027 (1990).

[26] X. Xi, Z. Wang, W. Zhao, J.-H. Park, K. T. Law, H. Berger, L. Forró, J. Shan, and K. F. Mak, Nature Physics **12**, 139 (2016).

[27] M. Gibertini, M. Koperski, A. F. Morpurgo, and K. S. Novoselov, Nature Nanotechnology **14**, 408 (2019).

[28] B. Huang, G. Clark, E. Navarro-Moratalla, D. R. Klein, R. Cheng, K. L. Seyler, D. Zhong, E. Schmidgall, M. A. McGuire, D. H. Cobden, W. Yao, D. Xiao, P. Jarillo-Herrero, and X. Xu, Nature **546**, 270 (2017).

[29] C. Gong, L. Li, Z. Li, H. Ji, A. Stern, Y. Xia, T. Cao, W. Bao, C. Wang, Y. Wang, Z. Q. Qiu, R. J. Cava, S. G. Louie, J. Xia, and X. Zhang, Nature **546**, 265 (2017).

[30] A. Splendiani, L. Sun, Y. Zhang, T. Li, J. Kim, C.-Y. Chim, G. Galli, and F. Wang, Nano Letters **10**, 1271 (2010), pMID: 20229981, https://doi.org/10.1021/nl903868w .

[31] K. F. Mak, C. Lee, J. Hone, J. Shan, and T. F. Heinz, Phys. Rev. Lett. **105**, 136805 (2010).

[32] Q. H. Wang, K. Kalantar-Zadeh, A. Kis, J. N. Coleman, and M. S. Strano, Nature Nanotechnology **7**, 699 (2012).

[33] Z. Wang, C. Tang, R. Sachs, Y. Barlas, and J. Shi, Phys. Rev. Lett. **114**, 016603 (2015).

[34] C. R. Dean, L. Wang, P. Maher, C. Forsythe, F. Ghahari, Y. Gao, J. Katoch, M. Ishigami, P. Moon, M. Koshino, T. Taniguchi, K. Watanabe, K. L. Shepard, J. Hone, and P. Kim, Nature **497**, 598 (2013).

[35] V. Shanmugam, R. A. Mensah, K. Babu, S. Gawusu, A. Chanda, Y. Tu, R. E. Neisiany, M. Försth, G. Sas, and O. Das, Particle & Particle Systems Characterization **39**, 2200031 (2022), https://onlinelibrary.wiley.com/doi/pdf/10.1002/ppsc.202200031 .

[36] A. J. Mannix, B. Kiraly, M. C. Hersam, and N. P. Guisinger, Nature Reviews Chemistry **1**, 0014 (2017).

[37] C.-Z. Chang, J. Zhang, X. Feng, J. Shen, Z. Zhang, M. Guo, K. Li, Y. Ou, P. Wei, L.-L. Wang, Z.-Q. Ji, Y. Feng, S. Ji, X. Chen, J. Jia, X. Dai, Z. Fang, S.-C. Zhang, K. He, Y. Wang, L. Lu, X.-C. Ma, and Q.-K. Xue, Science **340**, 167 (2013), https://www.science.org/doi/pdf/10.1126/science.1234414 .

[38] R. F. Frindt, Journal of Applied Physics **37**, 1928 (1966), https://doi.org/10.1063/1.1708627 .

[39] R. F. Frindt, Phys. Rev. Lett. **28**, 299 (1972).

[40] A. K. Geim and I. V. Grigorieva, Nature **499**, 419 (2013).

[41] Y. Zhang, J. P. Small, W. V. Pontius, and P. Kim, Applied Physics Letters **86**, 073104 (2005), https://aip.scitation.org/doi/pdf/10.1063/1.1862334 .

[42] L. Yuan, J. Ge, X. Peng, Q. Zhang, Z. Wu, Y. Jian, X. Xiong, H. Yin, and J. Han, AIP Advances **6**, 125201 (2016), https://doi.org/10.1063/1.4967967 .

[43] Y. Huang, E. Sutter, N. N. Shi, J. Zheng, T. Yang, D. Englund, H.-J. Gao, and P. Sutter, ACS Nano **9**, 10612 (2015), pMID: 26336975, https://doi.org/10.1021/acsnano.5b04258 .

[44] M. Velický, G. E. Donnelly, W. R. Hendren, S. McFarland, D. Scullion, W. J. I. DeBenedetti, G. C. Correa, Y. Han, A. J. Wain, M. A. Hines, D. A. Muller, K. S. Novoselov, H. D. Abruña, R. M. Bowman, E. J. G. Santos, and F. Huang, ACS Nano **12**, 10463 (2018), pMID: 30265515, https://doi.org/10.1021/acsnano.8b06101 .

[45] J.-S. You, S. Fang, S.-Y. Xu, E. Kaxiras, and T. Low, Phys. Rev. B **98**, 121109 (2018).

[46] M. Kan, J. Y. Wang, X. W. Li, S. H. Zhang, Y. W. Li, Y. Kawazoe, Q. Sun, and P. Jena, The Journal of Physical Chemistry C **118**, 1515 (2014), https://doi.org/10.1021/jp4076355 .

[47] A. J. Grant, T. M. Griffiths, G. D. Pitt, and A. D. Yoffe, Journal of Physics C: Solid State Physics **8**, L17 (1975).

[48] C. Ruppert, B. Aslan, and T. F. Heinz, Nano Letters **14**, 6231 (2014), pMID: 25302768, https://doi.org/10.1021/nl502557g .

[49] A. A. Soluyanov, D. Gresch, Z. Wang, Q. Wu, M. Troyer, X. Dai, and B. A. Bernevig, Nature **527**, 495 (2015).

[50] Y. Sun, S.-C. Wu, M. N. Ali, C. Felser, and B. Yan, Phys. Rev. B **92**, 161107 (2015).

[51] L. Huang, T. M. McCormick, M. Ochi, Z. Zhao, M.-T. Suzuki, R. Arita, Y. Wu, D. Mou, H. Cao, J. Yan, N. Trivedi, and A. Kaminski, Nature Materials **15**, 1155 (2016).

[52] K. Deng, G. Wan, P. Deng, K. Zhang, S. Ding, E. Wang, M. Yan, H. Huang, H. Zhang, Z. Xu, J. Denlinger, A. Fedorov, H. Yang, W. Duan, H. Yao, Y. Wu, S. Fan, H. Zhang, X. Chen, and S. Zhou, Nature Physics **12**, 1105 (2016).

[53] F. Y. Bruno, A. Tamai, Q. S. Wu, I. Cucchi, C. Barreteau, A. de la Torre, S. McKeown Walker, S. Riccò, Z. Wang, T. K. Kim, M. Hoesch, M. Shi, N. C. Plumb, E. Giannini, A. A. Soluyanov, and F. Baumberger, Phys. Rev. B **94**, 121112 (2016).

[54] Y. Wu, D. Mou, N. H. Jo, K. Sun, L. Huang, S. L. Bud'ko, P. C. Canfield, and A. Kaminski, Phys. Rev. B **94**, 121113 (2016).

[55] P. Li, Y. Wen, X. He, Q. Zhang, C. Xia, Z.-M. Yu, S. A. Yang, Z. Zhu, H. N. Alshareef, and X.-X. Zhang, Nature Communications **8**, 2150 (2017).

[56] P. K. Das, D. D. Sante, F. Cilento, C. Bigi, D. Kopic, D. Soranzio, A. Sterzi, J. A. Krieger, I. Vobornik, J. Fujii, T. Okuda, V. N. Strocov, M. B. H. Breese, F. Parmigiani, G. Rossi, S. Picozzi, R. Thomale, G. Sangiovanni, R. J. Cava, and G. Panaccione, Electronic Structure **1**, 014003 (2019).

[57] Z. Fei, T. Palomaki, S. Wu, W. Zhao, X. Cai, B. Sun, P. Nguyen, J. Finney, X. Xu, and D. H. Cobden, Nature Physics **13**, 677 (2017).

[58] D. H. Keum, S. Cho, J. H. Kim, D.-H. Choe, H.-J. Sung, M. Kan, H. Kang, J.-Y. Hwang, S. W. Kim, H. Yang, K. J. Chang, and Y. H. Lee, Nature Physics **11**, 482 (2015).

[59] M. N. Ali, J. Xiong, S. Flynn, J. Tao, Q. D. Gibson, L. M. Schoop, T. Liang, N. Haldolaarachchige, M. Hirschberger, N. P. Ong, and R. J. Cava, Nature **514**, 205 (2014).

[60] F. C. Chen, H. Y. Lv, X. Luo, W. J. Lu, Q. L. Pei, G. T. Lin, Y. Y. Han, X. B. Zhu, W. H. Song, and Y. P. Sun, Phys. Rev. B **94**, 235154 (2016).

[61] A. Tiwari, F. Chen, S. Zhong, E. Drueke, J. Koo, A. Kaczmarek, C. Xiao, J. Gao, X. Luo, Q. Niu, Y. Sun, B. Yan, L. Zhao, and A. W. Tsen, Nature Communications **12**, 2049 (2021).

[62] P. Blake, E. W. Hill, A. H. Castro Neto, K. S. Novoselov, D. Jiang, R. Yang, T. J. Booth, and A. K. Geim, Applied Physics Letters **91**, 063124 (2007), https://doi.org/10.1063/1.2768624 .

[63] Z. H. Ni, H. M. Wang, J. Kasim, H. M. Fan, T. Yu, Y. H. Wu, Y. P. Feng, and Z. X. Shen, Nano Letters **7**, 2758 (2007), pMID: 17655269, https://doi.org/10.1021/nl071254m .

[64] A. W. Tsen, R. Hovden, D. Wang, Y. D. Kim, J. Okamoto, K. A. Spoth, Y. Liu, W. Lu, Y. Sun, J. C. Hone, L. F. Kourkoutis, P. Kim, and A. N. Pasupathy, Proceedings of the National Academy of Sciences **112**, 15054 (2015), https://www.pnas.org/doi/pdf/10.1073/pnas.1512092112 .

[65] A. Castellanos-Gomez, M. Buscema, R. Molenaar, V. Singh, L. Janssen, H. S. J. van der Zant, and G. A. Steele, 2D Materials **1**, 011002 (2014).

[66] F. Pizzocchero, L. Gammelgaard, B. S. Jessen, J. M. Caridad, L. Wang, J. Hone, P. Bøggild, and T. J. Booth, Nature Communications **7**, 11894 (2016).

[67] D. G. Purdie, N. M. Pugno, T. Taniguchi, K. Watanabe, A. C. Ferrari, and A. Lombardo, Nature Communications **9**, 5387 (2018).

[68] T. Gilani and D. Rabchuk, Canadian Journal of Physics **96**, 272 (2018), https://doi.org/10.1139/cjp-2017-0484 .

[69] F. Pobell, *Matter and methods at low temperatures*, 3rd ed. (Springer, 2007).

[70] C. Manolikas, J. van Landuyt, and S. Amelinckx, physica status solidi (a) **53**, 327 (1979), https://onlinelibrary.wiley.com/doi/pdf/10.1002/pssa.2210530138 .

[71] I. G. Lezama, A. Ubaldini, M. Longobardi, E. Giannini, C. Renner, A. B. Kuzmenko, and A. F. Morpurgo, 2D Materials **1**, 021002 (2014).

[72] B. E. Brown, Acta Crystallographica **20**, 268 (1966).

[73] K. Ueno and K. Fukushima, Applied Physics Express **8**, 095201 (2015).

[74] R. Clarke, E. Marseglia, and H. P. Hughes, Philosophical Magazine B **38**, 121 (1978), https://doi.org/10.1080/13642817808245670 .

[75] S. Cho, S. Kim, J. H. Kim, J. Zhao, J. Seok, D. H. Keum, J. Baik, D.-H. Choe, K. J. Chang, K. Suenaga, S. W. Kim, Y. H. Lee, and H. Yang, Science **349**, 625 (2015), https://www.science.org/doi/pdf/10.1126/science.aab3175 .

[76] Y. Wang, J. Xiao, H. Zhu, Y. Li, Y. Alsaid, K. Y. Fong, Y. Zhou, S. Wang, W. Shi, Y. Wang, A. Zettl, E. J. Reed, and X. Zhang, Nature **550**, 487 (2017).

[77] J. Yang, J. Colen, J. Liu, M. C. Nguyen, G. wei Chern, and D. Louca, Science Advances **3**, eaao4949 (2017), https://www.science.org/doi/pdf/10.1126/sciadv.aao4949 .

[78] S. Lee, J. Jang, S.-I. Kim, S.-G. Jung, J. Kim, S. Cho, S. W. Kim, J. Y. Rhee, K.-S. Park, and T. Park, Scientific Reports **8**, 13937 (2018).

[79] Y. Qi, P. G. Naumov, M. N. Ali, C. R. Rajamathi, W. Schnelle, O. Barkalov, M. Hanfland, S.-C. Wu, C. Shekhar, Y. Sun, V. Süß, M. Schmidt, U. Schwarz, E. Pippel, P. Werner, R. Hillebrand, T. Förster, E. Kampert, S. Parkin, R. J. Cava, C. Felser, B. Yan, and S. A. Medvedev, Nature Communications **7**, 11038 (2016).

[80] X. Luo, F. C. Chen, J. L. Zhang, Q. L. Pei, G. T. Lin, W. J. Lu, Y. Y. Han, C. Y. Xi, W. H. Song, and Y. P. Sun, Applied Physics Letters **109**, 102601 (2016), https://doi.org/10.1063/1.4962466 .

[81] Z. Guguchia, F. von Rohr, Z. Shermadini, A. T. Lee, S. Banerjee, A. R. Wieteska, C. A. Marianetti, B. A. Frandsen, H. Luetkens, Z. Gong, S. C. Cheung, C. Baines, A. Shengelaya, G. Taniashvili, A. N. Pasupathy, E. Morenzoni, S. J. L. Billinge, A. Amato, R. J. Cava, R. Khasanov, and Y. J. Uemura, Nature Communications **8**, 1082 (2017).

[82] Y. Li, Q. Gu, C. Chen, J. Zhang, Q. Liu, X. Hu, J. Liu, Y. Liu, L. Ling, M. Tian, Y. Wang, N. Samarth, S. Li, T. Zhang, J. Feng, and J. Wang, Proceedings of the National Academy of Sciences **115**, 9503 (2018), https://www.pnas.org/doi/pdf/10.1073/pnas.1801650115 .

[83] W. Wang, S. Kim, M. Liu, F. A. Cevallos, R. J. Cava, and N. P. Ong, Science **368**, 534 (2020), https://www.science.org/doi/pdf/10.1126/science.aaw9270 .

[84] Z. Wang, D. Gresch, A. A. Soluyanov, W. Xie, S. Kushwaha, X. Dai, M. Troyer, R. J. Cava, and B. A. Bernevig, Phys. Rev. Lett. **117**, 056805 (2016).

[85] A. Tamai, Q. S. Wu, I. Cucchi, F. Y. Bruno, S. Riccò, T. K. Kim, M. Hoesch, C. Barreteau, E. Giannini, C. Besnard, A. A. Soluyanov, and F. Baumberger, Phys. Rev. X **6**, 031021 (2016).

[86] J. Jiang, Z. K. Liu, Y. Sun, H. F. Yang, C. R. Rajamathi, Y. P. Qi, L. X. Yang, C. Chen, H. Peng, C.-C. Hwang, S. Z. Sun, S.-K. Mo, I. Vobornik, J. Fujii, S. S. P. Parkin, C. Felser, B. H. Yan, and Y. L. Chen, Nature Communications **8**, 13973 (2017).

[87] J. C. Park, E. Jung, S. Lee, J. Hwang, and Y. H. Lee, Phys. Rev. B **101**, 235434 (2020).

[88] S. Tang, C. Zhang, D. Wong, Z. Pedramrazi, H.-Z. Tsai, C. Jia, B. Moritz, M. Claassen, H. Ryu, S. Kahn, J. Jiang, H. Yan, M. Hashimoto, D. Lu, R. G. Moore, C.-C. Hwang, C. Hwang, Z. Hussain, Y. Chen, M. M. Ugeda, Z. Liu, X. Xie, T. P. Devereaux, M. F. Crommie, S.-K. Mo, and Z.-X. Shen, Nature Physics **13**, 683 (2017).

[89] S. Tang, C. Zhang, C. Jia, H. Ryu, C. Hwang, M. Hashimoto, D. Lu, Z. Liu, T. P. Devereaux, Z.-X. Shen, and S.-K. Mo, APL Materials **6**, 026601 (2018), https://doi.org/10.1063/1.5004700 .

[90] P. Song, C. Hsu, M. Zhao, X. Zhao, T.-R. Chang, J. Teng, H. Lin, and K. P. Loh, 2D Materials **5**, 031010 (2018).

[91] J. Guo and K. Liu, Nanomaterials **12**, 10.3390/nano12010110 (2022).

[92] L. Wang, I. Gutiérrez-Lezama, C. Barreteau, N. Ubrig, E. Giannini, and A. F. Morpurgo, Nature Communications **6**, 8892 (2015).

[93] C.-H. Lee, E. C. Silva, L. Calderin, M. A. T. Nguyen, M. J. Hollander, B. Bersch, T. E. Mallouk, and J. A. Robinson, Scientific Reports **5**, 10013 (2015).

81

[94] F. Ye, J. Lee, J. Hu, Z. Mao, J. Wei, and P. X.-L. Feng, Small **12**, 5802 (2016), https://onlinelibrary.wiley.com/doi/pdf/10.1002/smll.201601207 .

[95] V. Fatemi, Q. D. Gibson, K. Watanabe, T. Taniguchi, R. J. Cava, and P. Jarillo-Herrero, Phys. Rev. B **95**, 041410 (2017).

[96] J. Joshi, I. R. Stone, R. Beams, S. Krylyuk, I. Kalish, A. V. Davydov, and P. M. Vora, Applied Physics Letters **109**, 031903 (2016), https://doi.org/10.1063/1.4959099 .

[97] S.-Y. Chen, T. Goldstein, D. Venkataraman, A. Ramasubramaniam, and J. Yan, Nano Letters **16**, 5852 (2016), pMID: 27517466, https://doi.org/10.1021/acs.nanolett.6b02666 .

[98] J. J. Laserna, ed., *Modern Techniques in Raman Spectroscopy* (Wiley, 1996).

[99] F. Baldini, A. Chester, J. Homola, and S. Martellucci, eds., *Optical Chemical Sensors* (Springer, 2006).

[100] C. Lee, H. Yan, L. E. Brus, T. F. Heinz, J. Hone, and S. Ryu, ACS Nano **4**, 2695 (2010), pMID: 20392077, https://doi.org/10.1021/nn1003937 .

[101] M. Grzeszczyk, K. Gołasa, M. Zinkiewicz, K. Nogajewski, M. R. Molas, M. Potemski, A. Wysmołek, and A. Babiński, 2D Materials **3**, 025010 (2016).

[102] R. He, J. van Baren, J.-A. Yan, X. Xi, Z. Ye, G. Ye, I.-H. Lu, S. M. Leong, and C. H. Lui, 2D Materials **3**, 031008 (2016).

[103] R. He, J. Okamoto, Z. Ye, G. Ye, H. Anderson, X. Dai, X. Wu, J. Hu, Y. Liu, W. Lu, Y. Sun, A. N. Pasupathy, and A. W. Tsen, Phys. Rev. B **94**, 201108 (2016).

[104] R. Zhao, Y. Wang, D. Deng, X. Luo, W. J. Lu, Y.-P. Sun, Z.-K. Liu, L.-Q. Chen, and J. Robinson, Nano Letters **17**, 3471 (2017), pMID: 28463560, https://doi.org/10.1021/acs.nanolett.7b00418 .

[105] R. He, S. Zhong, H. H. Kim, G. Ye, Z. Ye, L. Winford, D. McHaffie, I. Rilak, F. Chen, X. Luo, Y. Sun, and A. W. Tsen, Phys. Rev. B **97**, 041410 (2018).

[106] A.-S. Pawlik, S. Aswartham, I. Morozov, M. Knupfer, B. Büchner, D. V. Efremov, and A. Koitzsch, Phys. Rev. Materials **2**, 104004 (2018).

[107] S. Paul, S. Karak, M. Mandal, A. Ram, S. Marik, R. P. Singh, and S. Saha, Phys. Rev. B **102**, 054103 (2020).

[108] M. N. Baibich, J. M. Broto, A. Fert, F. N. Van Dau, F. Petroff, P. Etienne, G. Creuzet, A. Friederich, and J. Chazelas, Phys. Rev. Lett. **61**, 2472 (1988).

[109] E. Dagotto, Brief introduction to giant magnetoresistance (gmr), in *Nanoscale Phase Separation and Colossal Magnetoresistance: The Physics of Manganites and Related Compounds* (Springer Berlin Heidelberg, 2003) pp. 395–405.

[110] S. Jin, T. H. Tiefel, M. McCormack, R. A. Fastnacht, R. Ramesh, and L. H. Chen, Science **264**, 413 (1994), https://www.science.org/doi/pdf/10.1126/science.264.5157.413 .

[111] A. B. Pippard, *Magnetoresistance in Metals* (Cambridge University Press, 1989).

[112] L. Schubnikow and W. J. de Haas, Proc. Netherlands Roy. Acad. Sci. **33**, 130 (1930).

[113] L. Schubnikow and W. J. de Haas, Nature **126**, 500 (1930).

[114] E. Adams and T. Holstein, Journal of Physics and Chemistry of Solids **10**, 254 (1959).

[115] D. Shoenberg, *Magnetic Oscillations in Metals*, Cambridge Monographs on Physics (Cambridge University Press, 1984).

[116] I. M. Lifshitz and A. M. Kosevich, Sov. Phys. JETP **2**, 636 (1956).

[117] W. J. de Haas and P. M. van Alphen, in *Proc. Netherlands Roy. Acad. Sci*, Vol. 33 (1930) p. 170.

[118] Y.-Y. Lv, X. Li, B. Pang, L. Cao, D. Lin, B.-B. Zhang, S.-H. Yao, Y. B. Chen, J. Zhou, S.-T. Dong, S.-T. Zhang, M.-H. Lu, and Y.-F. Chen, Journal of Applied Physics **122**, 045102 (2017), https://doi.org/10.1063/1.4995951 .

[119] N. W. Ashcroft and N. D. Mermin, *Solid State Physics* (Holt-Saunders, 1976).

[120] S. Thirupathaiah, R. Jha, B. Pal, J. S. Matias, P. K. Das, P. K. Sivakumar, I. Vobornik, N. C. Plumb, M. Shi, R. A. Ribeiro, and D. D. Sarma, Phys. Rev. B **95**, 241105 (2017).

[121] E. H. Hall, American Journal of Mathematics **2**, 287 (1879).

[122] E. Hall, The London, Edinburgh, and Dublin Philosophical Magazine and Journal of Science **12**, 157 (1881), https://doi.org/10.1080/14786448108627086 .

[123] N. Nagaosa, J. Sinova, S. Onoda, A. H. MacDonald, and N. P. Ong, Rev. Mod. Phys. **82**, 1539 (2010).

[124] I. Sodemann and L. Fu, Phys. Rev. Lett. **115**, 216806 (2015).

[125] O. O. Shvetsov, V. D. Esin, A. V. Timonina, N. N. Kolesnikov, and E. V. Deviatov, JETP Letters **109**, 715 (2019).

[126] S.-C. Ho, C.-H. Chang, Y.-C. Hsieh, S.-T. Lo, B. Huang, T.-H.-Y. Vu, C. Ortix, and T.-M. Chen, Nature Electronics **4**, 116 (2021).

[127] D. Kumar, C.-H. Hsu, R. Sharma, T.-R. Chang, P. Yu, J. Wang, G. Eda, G. Liang, and H. Yang, Nature Nanotechnology **16**, 421 (2021).

[128] S. Dzsaber, X. Yan, M. Taupin, G. Eguchi, A. Prokofiev, T. Shiroka, P. Blaha, O. Rubel, S. E. Grefe, H.-H. Lai, Q. Si, and S. Paschen, Proceedings of the National Academy of Sciences **118**, e2013386118 (2021), https://www.pnas.org/doi/pdf/10.1073/pnas.2013386118 .

[129] P. He, H. Isobe, D. Zhu, C.-H. Hsu, L. Fu, and H. Yang, Nature Communications **12**, 698 (2021).

[130] Z. Z. Du, H.-Z. Lu, and X. C. Xie, Nature Reviews Physics **3**, 744 (2021).

[131] M.-S. Qin, P.-F. Zhu, X.-G. Ye, W.-Z. Xu, Z.-H. Song, J. Liang, K. Liu, and Z.-M. Liao, Chin. Phys. Lett. **38**, 017301 (2021).

[132] M. Huang, Z. Wu, J. Hu, X. Cai, E. Li, L. An, X. Feng, Z. Ye, N. Lin, K. T. Law, and N. Wang, National Science Review , nwac232 (2022).

[133] Y. R. Shen, *The Principles of Nonlinear Optics* (Wiley, Hoboken, 2002).

[134] Q. Song, X. Pan, H. Wang, K. Zhang, Q. Tan, P. Li, Y. Wan, Y. Wang, X. Xu, M. Lin, X. Wan, F. Song, and L. Dai, Scientific Reports **6**, 29254 (2016).

[135] Y. C. Jiang, J. Gao, and L. Wang, Scientific Reports **6**, 19624 (2016).

[136] T. Ma, H. Chen, K. Yananose, X. Zhou, L. Wang, R. Li, Z. Zhu, Z. Wu, Q.-H. Xu, J. Yu, C. W. Qiu, A. Stroppa, and K. P. Loh, Nature Communications **13**, 5465 (2022).

[137] H. Isobe, S.-Y. Xu, and L. Fu, Science Advances **6**, eaay2497 (2020), https://www.science.org/doi/pdf/10.1126/sciadv.aay2497 .

[138] Y. Zhang and L. Fu, Proceedings of the National Academy of Sciences **118**, e2100736118 (2021), https://www.pnas.org/doi/pdf/10.1073/pnas.2100736118 .

[139] J. Garnica, R. A. Chinga, and J. Lin, Proceedings of the IEEE **101**, 1321 (2013).

[140] S. Hemour and K. Wu, Proceedings of the IEEE **102**, 1667 (2014).

[141] A. R. Mellnik, J. S. Lee, A. Richardella, J. L. Grab, P. J. Mintun, M. H. Fischer, A. Vaezi, A. Manchon, E.-A. Kim, N. Samarth, and D. C. Ralph, Nature **511**, 449 (2014).

[142] D. MacNeill, G. M. Stiehl, M. H. D. Guimarães, N. D. Reynolds, R. A. Buhrman, and D. C. Ralph, Phys. Rev. B **96**, 054450 (2017).

[143] D. MacNeill, G. M. Stiehl, M. H. D. Guimaraes, R. A. Buhrman, J. Park, and D. C. Ralph, Nature Physics **13**, 300 (2017).

[144] M. H. D. Guimarães, G. M. Stiehl, D. MacNeill, N. D. Reynolds, and D. C. Ralph, Nano Letters **18**, 1311 (2018), pMID: 29328662, https://doi.org/10.1021/acs.nanolett.7b04993 .

[145] T. Horaguchi, M. Matsuo, and Y. Nozaki, Journal of Magnetism and Magnetic Materials **505**, 166727 (2020).

[146] F. Qin, W. Shi, T. Ideue, M. Yoshida, A. Zak, R. Tenne, T. Kikitsu, D. Inoue, D. Hashizume, and Y. Iwasa, Nature Communications **8**, 14465 (2017).